Thermal Emission of Strontium Products for Scalar Diagnostics in Internal Combustion Engines

by

Ivan Andres Tibavinsky

A dissertation submitted in partial fulfillment
of the requirements for the degree of
Doctor of Philosophy
(Mechanical Engineering)
in the University of Michigan
2019

Doctoral Committee:

Professor Volker Sick, Chair
Professor Andre Boehman
Associate Professor Mirko Gamba
Professor Pramod Sangi Reddy

Ivan A. Tibavinsky

ivantib@umich.edu

ORCID iD : 0000-0002-1012-1602

Dedication

To my parents, William and Constanza

Acknowledgements

I consider myself fortunate to realize the immensity of the community to which I must whole-heartedly express my gratitude for being part of the process that culminates with this document. I would like to thank my advisor, Prof. Volker Sick, for his energetic support, encouragement, and guidance, which have been profoundly nourishing for my growth as an engineer. I must also thank the members of my dissertation committee for their inspirational input to the different aspects of this project.

Further, I am indebted to the technicians and staff in the Autolab for maintaining the facilities and always providing assistance when needed. In particular I would like to mention James Elkins, whose opportune and kind help was crucial to the rebuilding of the optical engine used in the experiments for this work and to whom I owe much of my confidence in being a “hands-on” engineer.

I also want to thank current and past undergraduates, graduates, post-doctoral fellows and research scientists at the Quantitative Laser Diagnostics Laboratory. Besides being a never-ending source of knowledge, motivation, and support, they created an environment in which I was always pleased to learn and work.

I was also very fortunate to have support from different organizations across campus. In particular I must recognize the encouragement offered by individuals in the former Office of Graduate education at the College of Engineering, Rackham Graduate School, and of course, by current and past graduate members of the Society of Hispanic Professional Engineers.

Lastly, I want to thank my family and friends who were with me during different stages of this process and helped me maintain confidence and grit during the innumerable challenges that surfaced along the way.

Table of Contents

List of Tables

List of Figures

List of Abbreviations

BDC	Bottom Dead Center
CAD	Crank Angle Degree
CI	Confidence Interval
DI	Direct Injection
FWHM	Full Width at Half Maximum
HCCI	Homogeneous Charge Compression Ignition
IC	Internal Combustion
IMEP	Integrated Mean Effective Pressure
MFB	Mass Fraction Burned
PFI	Port Fuel Injection
PLIF	Planar Laser Induced Fluorescence
SC	Stratified Combustion
SI	Spark Ignition
SIDI	Spark Ignition – Direct Injection
TCC	Transparent Combustion Chamber
TDCc	Top Dead Center - compression

Abstract

Developments in optical diagnostics for combustion systems have been essential to the recent improvements in efficiency and abatement of emissions that internal combustion engines have undergone recently. Great emphasis has been placed in the measurement of quantities with high temporal and spatial resolution, which has enabled the understanding of key physical and chemical processes, but there remains a need for obtaining spatially integrated measurements to understand how local events affect the overall behavior of the gases in a turbulent combustion chamber. Strontium offers a potential avenue to provide these measurements. When present in combustion it produces strontium monohydroxide, which spontaneously emits radiation in several bands of the visible spectrum, and thus enables the determination of temperature independently of species concentration through the Boltzmann distribution. Further, chemical equilibrium calculations can relate equivalence ratio to the relative concentration strontium and strontium monohydroxide, which could also be measured optically.

The potential of this technique was explored in this work. An optical engine was operated under different conditions with a strontium-containing fuel and spectral measurements of the radiation emitted from the chamber were performed. The temperature in the cylinder was predicted by a one-dimensional thermodynamic model that used a two-zone model for flame propagation. The relative spectrally resolved emission intensity of atomic strontium and strontium monohydroxide was measured using a spectrometer coupled with camera, and the collected signals were related to the conditions in the chamber. From the results the mathematical formulation for the relationship of spectral intensity with temperature was found to be adequate, and important insights for the application of the diagnostic in imaging experiments were obtained. A universally applicable calibration was not attained due to experimental limitations, however, but the key barriers to overcome were identified.

Chapter 1

Motivation and Context

The automotive Internal Combustion (IC) engine has several key characteristics that have made it an essential tool for societies around the world since its widespread introduction in the early 20th century. Its high energy density and historically low-cost energy source made it possible for individuals to own their main transportation medium, which has allowed them to quickly and conveniently travel on their own schedule. In addition, the ease and the speed with which vehicles that utilize IC engines are refueled also facilitates the rapid and efficient transportation of goods around the world. As an established technology, the IC engine also enables the production of transportation vehicles at a relatively low cost and requires few to no infrastructure changes, which makes it adequate to satisfy the growing demand for transportation. Today this device powers the vast majority of land vehicles. Although alternative technologies are quickly growing, it is unlikely that any of them will match all of the key features that the IC engine offers simultaneously in the foreseeable future. For this reason, the engine will likely keep an important role in society for many years to come.

However, the IC engine is also well known to present a number of significant challenges. Emissions of particulate matter, nitrogen oxides, carbon monoxide, and unburnt hydrocarbons are of great concern for public health and the environment, especially in densely populated areas. Carbon dioxide emissions represent, perhaps, an even greater threat as they contribute substantially to human-induced climate change. Additionally, the long-term world-wide availability of oil-derived fuels as a reliable source of energy is under threat by political and economic instabilities. Although the IC engine has seen tremendous improvements in recent years, further development is critical in order to meet present and future demands.

Significant contributions to this overarching objective may be made by improving light-duty vehicle technologies in particular. In the U. S. this transportation sector alone produces about 17% of all greenhouse gas emissions [1]. Advancements in this area will rely heavily on overcoming the inherent limitations imposed by homogeneous charge spark ignition engines, since this is the dominant technology on which vehicles on the road rely today. In order to realize the needed improvements, a better understanding of the fundamental processes that take place during combustion at engine conditions is essential. This work presents an optical diagnostics tool that has the potential to accelerate the understanding of those processes.

In the next Section a general description of IC engines is provided in order to understand how their much needed improvements might come about. In addition, the fundamentals behind some of the analyses performed in the study of the diagnostics technique presented are given.

1.1 Fundamentals of IC Engines

In an engine, the conversion of chemical energy of fuel into mechanical energy occurs in a piston-cylinder arrangement which usually operates on a 4-stroke cycle, as illustrated in Figure 1.1. During the first stroke of the cycle (intake), the intake valves open and air enters the chamber. Fuel is typically introduced at this stage as well in gasoline engines. Next, during the second stroke (compression), the valves close and the gases in the cylinder are compressed as the volume of the chamber is reduced by the movement of the piston. At this point in the cycle, when the chamber reaches its smallest volume the piston is said to be at Top Dead Center compression (TDCc), and in the ideal representation of the gasoline engine, it is at this time that combustion takes place and the third stroke (power) begins. As the gases expand, they push on the piston and thus produce mechanical energy as the piston travels towards the Bottom Dead Center (BDC) position, the point at which the chamber has its largest volume. Finally, during the fourth stroke (exhaust), the exhaust valves open, the movement of the piston reduces the volume of the chamber again, and the waste gases exit the cylinder.

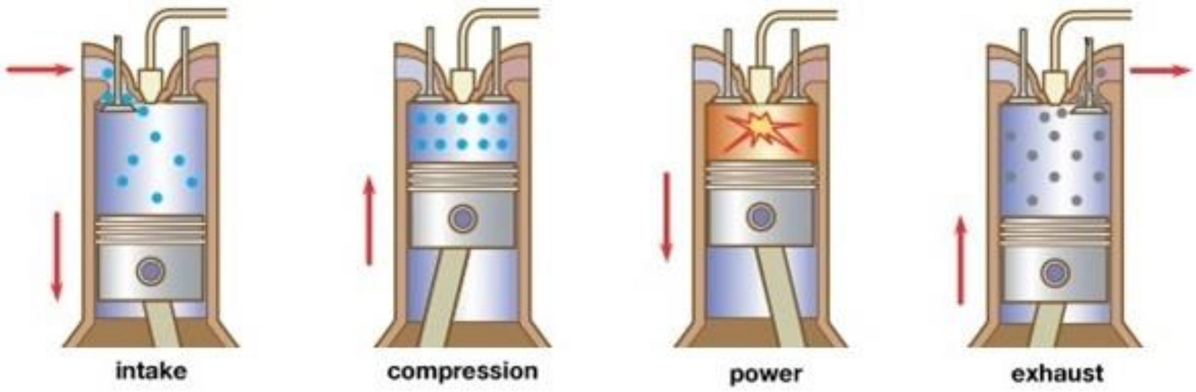

Figure 1.1 The four strokes of a typical automotive interal combustion engine. Adapted from [2].

Equation (1. 1) is an overall first-law thermodynamic analysis over the four strokes. Through combustion, the chemical energy of the fresh charge in the cylinder, Q_{ch}, is transformed into internal energy in the fluid, U, net work done pushing the piston, W, and heat transferred to the walls of the cylinder, q. Some unreleased chemical energy, Q_{cr}, results from the fact that a small portion of the unburnt charge occupies small spaces in the chamber between the liner, piston, rings and other components that cannot be reached by the propagating flame.

$$Q_{ch} = U + W + q + Q_{cr} \tag{1. 1}$$

1.1.1 Efficiency

The thermal efficiency of the engine is defined as the ratio of the net work to the chemical energy provided to the cylinder, as given in Equation (1. 2). A more detailed analysis of each of the strokes demonstrates that efficiency may also be expressed as a function of the ratio of the maximum and the minimum volume of the combustion chamber, r_c, also called the compression ratio, and the ratio of specific heat of the working fluid, γ [3].

$$\eta_{\text{th}} = \frac{W}{Q_{ch}} = 1 - \frac{1}{{r_c}^{\gamma-1}} \tag{1. 2}$$

1.1.2 Apparent Heat Release

Another useful metric of engine performance is the apparent heat release, Q_{app}. In a properly instrumented engine it can be readily calculated, and it provides information about the deviation of the operation of the engine from the ideal hypothetical scenario in which combustion occurs instantaneously at TDCc, which is helpful for setting operation parameters and comparing their effect in engine performance. It is defined to be the linear combination of the work performed on the piston, and the increase in internal energy of the gases. Equation (1. 3) defines this quantity in differential form and expresses it in an equivalent way using thermodynamic definitions.

$$\delta Q_{app} = dU + \delta W = mc_v \, dT + P \, dV \tag{1. 3}$$

Here, m is the mass of the gas, c_v is its constant volume heat capacity, T is the temperature, P is the pressure, and V is the volume.

An equivalent expression for dT results from application of the ideal gas law while neglecting the change of specific gas constant, R. This gives:

$$dT = d\left(\frac{PV}{mR}\right) = \frac{1}{mR}(P \, dV + V \, dP) \tag{1. 4}$$

Substitution of dT into Equation (1. 3) and applying Mayer's relation ($R = c_p - c_v$), the apparent heat release rate becomes:

$$\frac{dQ_{app}}{d\theta} = \frac{c_v}{R} V \frac{dP}{d\theta} + \left(\frac{c_v}{R} + 1\right) P \frac{dV}{d\theta} = \frac{1}{\gamma - 1} V \frac{dP}{d\theta} + \frac{\gamma}{\gamma - 1} P \frac{dV}{d\theta} \tag{1. 5}$$

where θ is the angular position of the engine's crank shaft. γ can be determined from thermodynamic relations and cylinder pressure and volume data. The compression and expansion strokes, represented in Figure 1. 2 by the diagonal straight lines, can be approximated as an adiabatic polytropic processes given by Equation (1. 6).

$$PV^{\gamma} = \text{constant} \tag{1. 6}$$

Therefore, by calculating the slope of each one of these linear portions of the plot, the ratio of specific heats during each one of the compression and expansion strokes can be estimated.

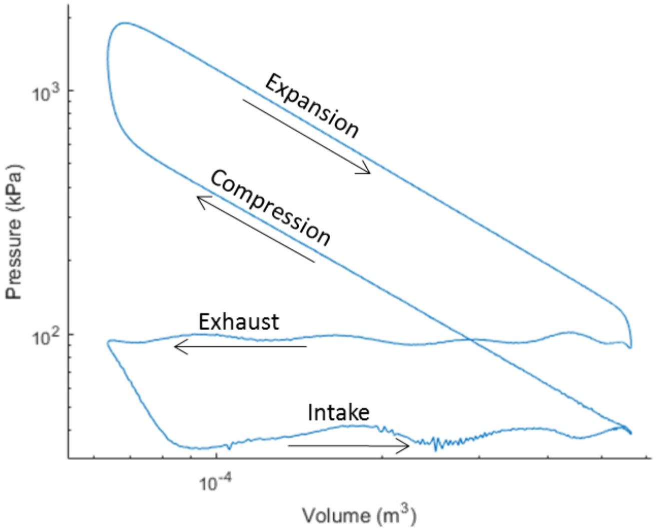

Figure 1. 2 Logarithmic plot of measured pressure vs volume in the combustion chamber of an engine during one cycle of homogeneous stoichiometric spark-ignited operation.

Thus, the rate at which heat is released from the combustion reaction may be estimated by integrating Equation (1. 5). This calculation neglects heat transfer between the gas in the cylinder and the walls, and although this is adequate for many purposes, a strict analysis must take this process into account as well.

1.1.3 Heat Transfer

The characterization of heat transfer between the gases in a combustion chamber and its walls is a complex problem that motivates much active research at present. The chaotic nature of the gas flow in a cylinder and the rapidly fluctuating local surface temperatures make an accurate quantification of this quantity extremely difficult. However, some tools have been devised to obtain reasonable approximations for some conditions.

Engine heat transfer quantification is typically reduced to defining the relationship between an effective convective heat transfer coefficient and the flow conditions, which is usually done in an empirical fashion. One of the most widely used correlations for gasoline engine applications, and the most relevant of the ones available in the software used for calculations in this work, is the one devised by Woschni [3, 4]. In it the fluid velocity is assumed to be proportional to the mean piston speed during intake, compression, and exhaust. During the power stroke, the change in fluid density is accounted for as well. The expression for convective heat transfer coefficient, h_c,is based on dimensionless transport quantities and reported to be

$$h_c(\mathrm{W/m^2 \cdot K}) = 3.26B(\mathrm{m})^{-0.2}P(\mathrm{kPa})^{0.8}T(\mathrm{K})^{-0.55}w(\mathrm{m/s})^{0.8} \tag{1. 7}$$

where B is the cylinder bore in meters, and w, the average cylinder gas velocity is defined as

$$w = C_1\bar{S}_p + C_2\frac{V_dT_r}{P_rV_r}(P - P_m) \tag{1. 8}$$

Here $\bar{S}_p$ is the mean piston speed, V_d is the displaced volume, P_m is the motored pressure at the given crank angle degree, and the subscript r denotes an arbitrary reference value for the corresponding quantity. For different strokes C_1 and C_2 are defined as follows:

$C_1 = 6.18, C_2 = 0$	for intake and exhaust
$C_1 = 2.28, C_2 = 0$	for compression
$C_1 = 2.28, C_2 = 3.24 \times 10^{-3}$	for expansion

Although the calculation of heat transfer requires uncertain quantities to be known, with empirical correlations such as this one, reasonable estimates may be obtained.

1.2 IC Engines Limitations and Avenues for Improvement

Although quantitative analyses provide an understanding of the different processes that affect engine performance, the most pressing current limitations can only be understood from a practical point of view. In most modern production gasoline engines, for instance, the stoichiometry of the mixture is tightly constrained to an equivalence ratio of 1, which introduces several disadvantages. This is done so that the efficient treatment of carbon monoxide, unburnt hydrocarbon, and nitrous oxide emissions is possible by use of a 3-way catalytic converter at the tailpipe. However, if a non-stoichiometric mixture is burnt in these engines, the reactions that enable the treatment of these pollutants would not take place. To avoid this situation, when the engine operates at low loads, power output is regulated by restricting the inflow of air into the chamber and injecting a proportional amount of fuel. Throttling air flow in this way causes the pressure in the cylinder to be lower than the atmospheric pressure, and therefore work is lost to filling the chamber. This lost energy is known as a pumping loss and accounts for much of the inefficiency of modern light-vehicle IC engines. Additional improvements in efficiency could also be accomplished if combustion took place under lean conditions instead [5]. This is because, as expressed in Equation (1. 2), thermal efficiency increases with increasing ratio of specific heats, and at the same time, the ratio of specific heats of a mixture of fuel and air generally increases with decreasing equivalence ratio [6].

It is also readily evident from Equation (1. 2) that another way to improve efficiency is to increase the cylinder compression ratio. However, it is not possible to do this arbitrarily in practice due to gasoline’s tendency to ignite spontaneously under high pressures, leading to high compression temperatures. This occurs most often after the main ignition event has taken place but before the charge is fully burnt. The expanding burnt gases compress the unburnt gas and causes it to initiate a secondary flame. This occurrence is known as knock, and it causes excessively high pressures and temperatures that may be harmful for the engine.

Alternative combustion strategies have a great potential to provide thermodynamic advantages that address these challenges. For example, pumping losses can be addressed by injecting fuel late during the compression stroke such that fuel and air do not have enough time to mix well, and a higher concentration of fuel results closer to the spark plug than elsewhere in the chamber. This is the concept of Stratified Combustion (SC). Ideally, the necessary conditions for ignition and subsequent complete burn of the charge would be obtained in this way even though, if the same relative amount of fuel and air were homogeneously mixed, the charge would be too lean to be within flammability limits. This form of operation permits power output at low loads to be regulated by the amount of fuel injected into the chamber only and, thus, it does not require air flow to be constrained.

Significant advantages could also be attained with Homogeneous Charge Compression Ignition (HCCI). In this mode the charge is well mixed before being ignited by compression.

This strategy typically operates with a globally and locally lean mixture, which results in a higher ratio of specific heats and allows the use of higher compression ratios.

However, these alternative combustion strategies face significant challenges that have impeded them from attaining wide commercial success. One of these is the management of emissions. Since these combustion modes utilize an overall non-stoichiometric charge, and therefore a catalytic converter cannot be used, tailpipe emissions must be controlled in the combustion process. One of the requirements to accomplish this is reaching a balance between local equivalence ratio and combustion temperature in the chamber. Figure 1. 3 depicts an equivalence ratio and temperature map that shows the combustion parameters under which soot and nitric oxide tend to form. A combustion strategy that does not require exhaust gas after-treatment must avoid the emission-prone areas during operation as well as any operation conditions that may result in increased unburnt hydrocarbon emissions.

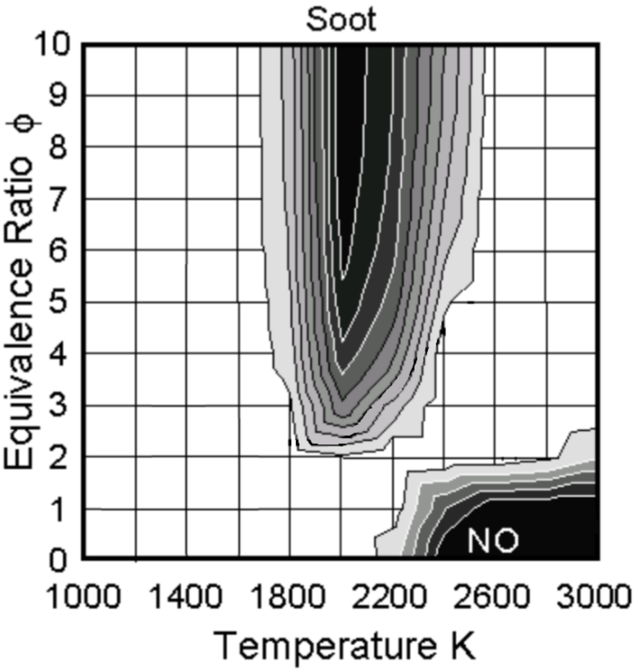

Figure 1. 3 Equivalence ratio – temperature map showing the local combustion conditions under which nitric oxide and soot tend to form. Adapted from [7].

Local conditions must also be controlled in engines that utilize novel combustion strategies to permit combustion stability. Significant variability in temperature and equivalence ratio from cycle-to-cycle results from the chaotic nature of the turbulent flow inside an engine cylinder. In consequence, ensuring that the precise conditions in the chamber are met consistently in order to ensure complete and in-phase combustion becomes very difficult.

Thus, for engines that operate on emerging combustion strategies such as the ones described above, control of local conditions in the cylinder during operation is imperative. The successful design of new engines that will be able to accomplish this relies on a deeper understanding of the interplay between flow and the parameters that determine emissions and combustion stability. For this reason, having accessible techniques to obtain in-cylinder measurements of quantities such as temperature and equivalence ratio with high temporal and spatial resolution is important.

1.3 Optical Diagnostics in IC Engines

Substantial achievements in the detailed understanding of combustion processes in the IC engine have been made possible by the use of advanced laser and high speed imaging technology with specially designed transparent engines. The methods that these instruments permit enable high temporal and spatial resolution measurements of quantities such as temperature and concentration of different species inside of an engine in operation, and thus elucidate aspects of key physical and chemical processes that would otherwise remain unknown. In addition, optical diagnostics have a pivotal benefit in that they are non-intrusive; they do not require probes that would disturb the flow and affect the measured quantities.

Optical diagnostics have also played a central role in the development of computational tools that are crucial for the development of IC engines. Conventionally, engine design has been centered on iterative experimental testing, which can be expensive and time consuming, but the design of combustion systems for transportation applications is significantly more efficient when guided by advanced computational models [8]. Simulating the performance of design iterations computationally is more time-and-resource-efficient, which ultimately accelerates progress. However, models that are accurate enough to be fully dependable for these purposes are not yet available. As these models are developed, optical diagnostics will provide a way to compare this models' predictions with experimental evidence.

Many techniques have been successfully used to measure temperature and equivalence ratio in IC engines. Most notably Raman scattering [9, 10] and PLIF [10-15] have been widely applied to measure these scalar quantities to explain in-cylinder events such as partial burns and misfires in SC engines and to explore the behavior of turbulent flames. The capabilities that these techniques offer have enabled much of the progress that the automotive engine has undergone in recent years.

1.3.1 Shortcomings Addressed in this Work

Although existing optical diagnostics have led to an increasing understanding of combustion processes by enabling measurements with an unprecedented level of detail, they have critical limitations. Two of these are addressed by the diagnostics technique presented in this work.

The first one is that many existing optical quantitative measurements provide detailed information about a portion of the chamber only, as in spark emission spectroscopy [11, 16], but in order to understand many of the processes that drive combustion in an engine an understanding of the state in the entire chamber is needed.

The second major shortcoming of state-of-the-art optical diagnostics addressed in this work is their complexity. This is a critical limiting factor in their use on industrial research and development. Many diagnostic methods utilize expensive and complicated lasers and intensifiers, which makes the techniques costly, time consuming, and difficult for personnel without extensive training to operate. For these reasons, these tools are useable only by highly specialized research teams. Reducing hardware requirements would make optical diagnostics more accessible to a wider community, and faster development of novel combustion strategies would be enabled.

1.3.2 Metal Thermal Emission Diagnostics in Engines

The limitations outlined above may be addressed with techniques that use the fluorescence of metals added to the combustion chamber of an engine. These methods have a demonstrated potential to provide measurements with three-dimensional information while minimizing hardware requirements. In particular, the capabilities offered by the introduction of alkali metals in the combustion chamber of IC engines have been progressively expanded since their first use in the 1930’s.

In early experiments, adding a sodium salt dust to the intake air of an engine made it possible to measure temperature in one dimension with the line reversal method [17-21]. This capability provided access to multiple insights into in-cylinder processes for the first time, but it only provided temperature along a line averaged over all the cycles in a given engine run. More recently, it was possible to quantify temperature close to the spark plug by measuring the relative intensities of potassium and sodium emissions in engines with limited optical access [22, 23]. However, these studies did not account for the equilibrium concentrations of the emitting species or considered the optical thickness of the gas, and therefore the accuracy of the reported measurements was limited. Metal thermal emission was also used later as a tool to enhance flame luminosity and acquire high-speed images in a SIDI optical engine [24].

Further progress was demonstrated by performing line-of-sight average measurements of temperature and equivalence ratio with high temporal and spatial resolution in a SIDI engine by imaging the spontaneous emission of three different alkali metals while estimating their equilibrium concentrations under different engine conditions [25, 26]. The three metals were sodium, lithium, and potassium. A combination of ratios and products of the three different atomic emissions, which was found to be independent of equivalence ratio through computational calculations, was used to determine temperature. With this knowledge, it was then possible to determine equivalence ratio by measuring the relative intensity of the radiative emission of two of the metals used. Thus, this work accounted for the equilibrium concentration of the emitting species, but inaccuracies were still a challenge if the assumed gas equilibrium conditions were not met, which is the case in some areas such as close to liquid fuel film fires, or if the precursor salts were not homogeneously distributed in the chamber.

The drawbacks that the use of alkali metals for scalar optical diagnostics present, which emerge from the need to know the concentration of emitting species, may be overcome by introducing alkali-earth metals in the combustion process instead. In the study presented in this document, the use of strontium as a dopant for measuring temperature and equivalence ratio in IC engines is explored. As will be explained in more detail in Chapter 2, the main benefit that this method offers stems from the fact that an alkali-earth-metal-doped flame emits multiple features in the visible region of the electromagnetic spectrum that originate from the same species, which eliminates the need to know equilibrium concentrations for temperature measurements and thus has the potential of making the diagnostic significantly more robust. The technique involves measuring atomic features and unresolved bands from a largely uncharacterized molecule, however, and therefore the capability to calculate scalar quantities from the thermal emission of strontium products at the conditions typically found in an engine cylinder must be confirmed experimentally. The main objective of this work is to obtain such confirmation.

Chapter 3 presents the experimental methodology followed in order to accomplish this goal. An optical engine was operated under different conditions, and emission in the visible range of the electromagnetic spectrum was measured at different Crank Angle Degrees (CAD). In parallel, a computational thermal model of the engine was used to calculate the temperature in the chamber at the moments in time in which the spectral measurements were made. This strategy was similar to that used successfully in previous studies [27], and was therefore considered to be adequate for the current objective. Insights were complemented with measurements of the emission spectrum of a flat flame burner doped with strontium compounds. The processing and analysis of the collected data is described in Chapter 4 along with a discussion of the results.

Finally, Chapter 5 states the main conclusion from this work and makes recommendations for future studies. Suggestions to address some of the uncertainties associated with the assumptions made are presented along with considerations for further development of the technique.

Chapter 2

Theoretical Background

The moderate addition of strontium into a combustion process of interest offers a potential for improved capabilities in optical diagnostics that facilitate the development of advanced combustion strategies in IC engines. The multiple bands in the visible spectrum that are emitted from the burnt gases enable the determination of temperature independently of species concentration through the Boltzmann distribution. This method could eventually produce spatially integrated measurements of temperature and equivalence ratio over an extended volume thus taking a step towards volumetric measurements of scalar quantities that would unravel 3-D in-cylinder engine processes. In addition, since this technique eliminates the need of lasers and reduces the required optical access, the method would result in simpler and less resource intensive experimental arrangements than currently available. A fundamental understanding of how this diagnostics method would be possible requires familiarity with the chemistry and spectroscopy of strontium in combustion environments.

2.1 Chemistry of Strontium in a Flame

Elemental strontium is a highly reactive metal, and as such it would be extremely difficult to handle and vaporize in an IC engine cylinder. It is far more convenient to introduce the metal in a molecular complex, as done in pyrotechnics. For the experiments performed in the present study, strontium acetylacetonate was dissolved in the fuel used in the engine experiments, as will be described in detail in Chapter 3.

Once doped fuel starts burning in the engine chamber, metal-containing molecules dissociate and readily release their metal atoms, which may react with other species. Atomic strontium tends to react with carbon dioxide and water molecules to form strontium oxide, SrO, strontium hydroxide, $Sr(OH)_2$, and strontium monohydroxide, SrOH [28, 29]. It is the formation of the last compound along with the unreacted atomic species that makes strontium a stronger alternative for non-laser-based combustion diagnostics than substances previously used for the same purposes. This is because strontium and its monohydroxide present in hot burnt gases emit strong radiation with spectral features in the visible range, as shown in Figure 2. 1. Strontium oxide, on the other hand, is present in the solid phase at these conditions since its melting point is 2800 K, and strontium hydroxide remains in the gas phase but condenses and precipitates when the burnt gases cool down. A solid residue might therefore be expected to remain in the chamber after the combustion process is completed. Indeed, such a deposit was found in the cylinder and on the walls of the exhaust system after the engine experiments described in Chapter 3.

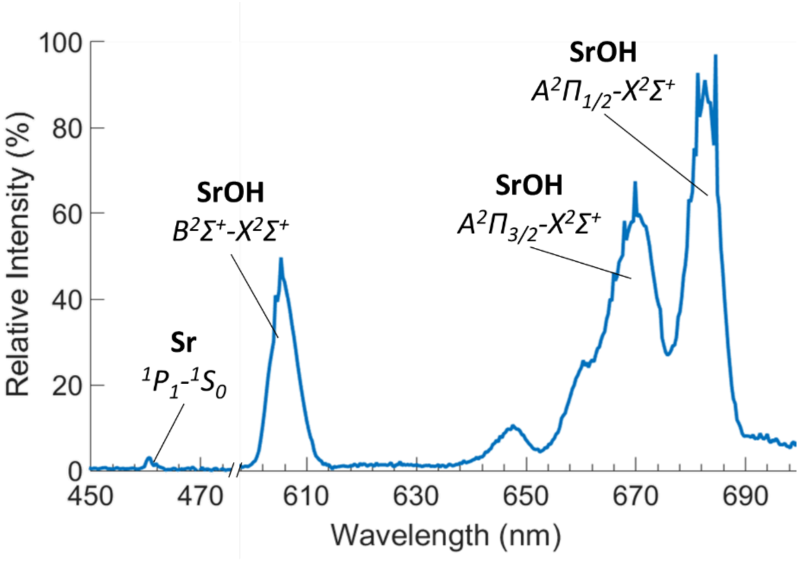

Figure 2. 1 Spectral distribution of radiation emitted from a strontium-containing methane-air stoichiometric flame at atmospheric pressure. The flame and spectral measurement were obtained with the setup described in Section 3.3. Spectroscopic terms were determined from [30, 31].

It is worth noting that other alkali-earth metals such as calcium and barium also have a great potential to support the improvement of combustion diagnostics, but strontium was the element of choice in this study because of practical advantages. Compounds that contain this metal are commercially available and safe to handle, and they were most easily dissolved in automotive fuels. In addition, strontium combustion products do not have any known effects that are harmful for either human health, the environment, or engine components. This made possible their introduction in an optical IC engine in operation.

A quantitative assessment of the equilibrium concentrations of the different strontium species at the conditions expected in the optical engine provides insight into practical aspects of the diagnostics technique. In order to perform such assessment, computational calculations using the NASA Combustion Equilibrium Application [32-34] were performed. The equilibrium of fuel, air, and strontium at prescribed constant temperatures was evaluated. The proportions of the initial substances were specified to represent an equivalence ratio range from 0.6 to 2 at 0.2 intervals and a relative mass fraction of strontium to fuel of 400 ppm and 1000 ppm[1]. The evaluated temperatures and pressures ranged from 800 K to 2800 K at 200 K intervals and 100 kPa to 2000 kPa at 500 kPa intervals, respectively, which is inclusive of the conditions at which radiative emission from inside the engine cylinder was expected to be observed and captured.

A result of particular interest for this study is that for any given combination of temperature and pressure values, the ratio of the equilibrium concentrations of strontium and strontium monohydroxide increases monotonically with equivalence ratio, as shown in Figure 2. 2. This relationship is what makes it possible to calculate the equivalence ratio in a flame from measurements of relative intensity of radiation emitted by atomic strontium and strontium monohydroxide. These results are not affected by the magnitude of the initial concentration of strontium in the mixture.

---

[1] These strontium content quantities are significantly higher than the ones used in the experiments in these work, but they were close to the minimum values that were possible to input in the program before results that signaled computational errors were obtained. Given that the results with both of these low values were identical, it is assumed that the results of relevance would be the same for lower quantities.

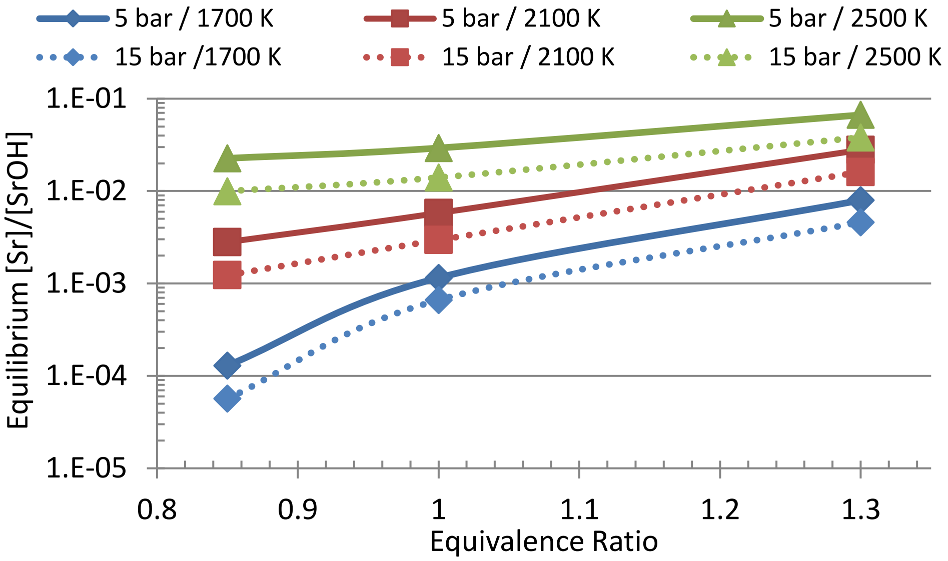

Figure 2. 2 The relative concentration of atomic strontium and strontium monohydroxide vs equivalence ratio is monotonic for all combinations of temperature and pressure considered.

While atomic strontium forms molecules that are useful for combustion diagnostics development, other by-products of the initial metal-containing molecule could cause significant difficulties. In particular, if strontium is introduced in a flame with a halogen salt, such as strontium chloride or strontium iodide, radiative emission that obscures the spectral features of strontium monohydroxide may result. Halogen salts are perhaps the most common compounds that contain alkali-earth metals, and it is therefore useful to study their use for the purpose of this work in detail. Figure 2. 3 on the left shows the spectrum of the radiation emitted by a flame to which a droplet of a saturated solution of water and strontium chloride was added. The flame was created with the flat-flame setup described in Chapter 3, as was the flame used to produce the spectrum shown in Figure 2. 1, but the spectrum in this case shows different features. This is because the flame that produced Figure 2. 1 was doped with strontium acetylacetonate, while the one that produced on the left-hand side of Figure 2. 3 was doped with strontium chloride. Strontium monochloride, a by-product of the combustion of strontium chloride, emits radiation with the spectral distribution shown on the right side of Figure 2. 3, which overlaps significantly in wavelength with strontium monohydroxide emission; a result of the similarities in molecular structure of strontium monohydroxide and the strontium halides. Although this signal interference only seems to be a practical problem when the substance is introduced in large amounts (otherwise, strontium monochloride radiative emission is generally too faint compared to that of strontium monohydroxide), halogen salts were altogether avoided in the experimental studies described in this document in order to prevent any potential ambiguities in the results due to this effect.

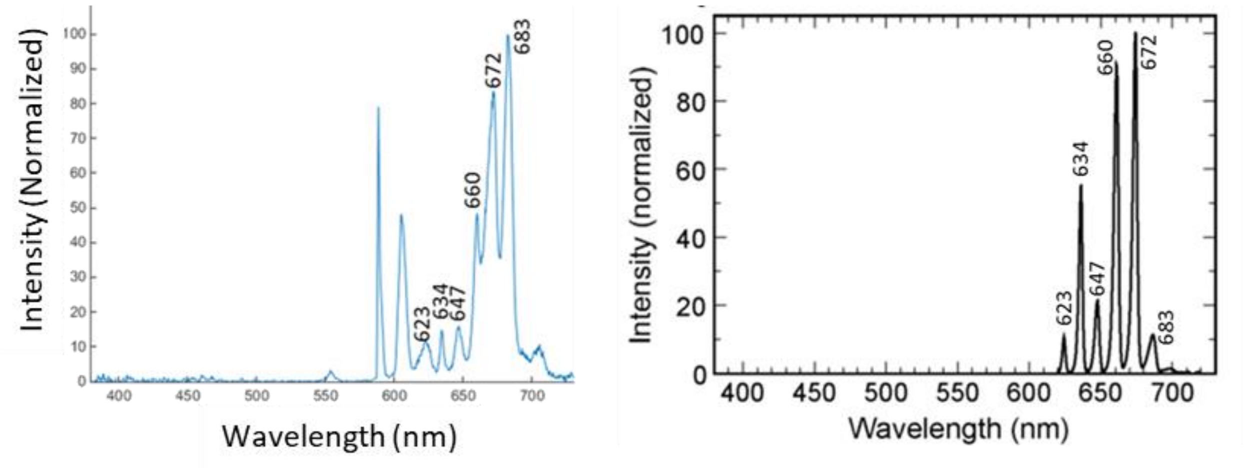

Figure 2. 3 Left: Spectral distribution of radiation emitted from flame heavily doped with strontium chloride. Right: Isolated emission spectrum of strontium monochloride [35].

2.2 Spectroscopy of Strontium Products

The science of spectroscopy provides the tools needed to describe the processes that result in radiative emission and explains how the produced radiation can be used for scalar gas diagnostics. An understanding of the discrete exchanges of energy between photons and particles such as strontium atoms and strontium monohydroxide molecules is instrumental in recognizing the quantitative relationships between electromagnetic emission, temperature and equivalence ratio.

2.2.1 Atomic Spectrum

The internal energy state of an isolated atom or molecule is at the center of the relevant processes for gas diagnostics. For an atom, this is determined exclusively by its electronic configuration, which can be described by the Schrödinger equation. A key result from this mathematical expression is that each electron in an atom can only acquire discrete energy levels. The internal energy of an atom as a whole is determined by the state of these individual electrons.

By interactions of an atom with a photon, a valence electron in an atom may undergo a change in energy level. The electron may make this energy level transition through absorption, induced emission, or spontaneous emission of photons. These radiative transition mechanisms, are depicted schematically in Figure 2. 4. In absorption, the valence electron may rise from a lower energy state, E'', to a higher energy state, E', by absorbing a photon. In induced emission, an electron that is already in an excited state may be induced to decay to a lower level by an incoming photon. In this process the electron will emit a second photon, and two photons of equal energy will result from the interaction. Finally, in spontaneous emission, an excited electron may decay spontaneously to a lower level and emit a photon in the process.

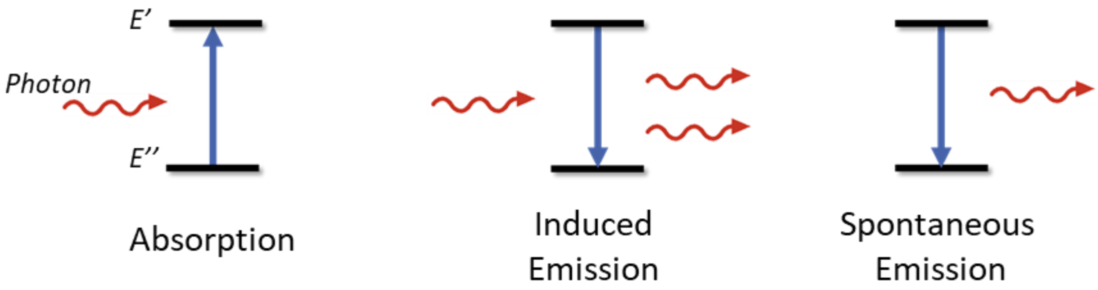

Figure 2. 4 Schematic representation of the most common radiative transition pathways of atoms observed in flames. The higher electronic level is indicated by E' and the lower one by E''.

For any of the above interactions to occur, the photon with which the atom interacts must have an energy magnitude equivalent to the energy difference between the initial and final states of the atom. Photon energy, E,is given by

$$E = E' - E'' = \frac{hc}{\lambda} \tag{2. 1}$$

where h is Planck's constant, and λ is the photon's wavelength. Thus, since the possible electron energy states are discrete and constant, the wavelength of the radiation involved is always approximately the same for a given transition of a particular element. As a result, atomic features in the electromagnetic spectrum typically appear as a line.

In the present work only the emission intensity of the atomic strontium lines observed in the visible spectrum are considered. At 460.7 nm there is a singlet line that corresponds to spontaneous emission due to the transition ${}^1P_1 \rightarrow {}^1S_0$ [36] (Banwell [37] provides a full description of term symbols). Strontium has another emission feature in the visible spectrum at around 689 nm, which corresponds to the transition ${}^3P_1 \rightarrow {}^1S_0$, but this is about four orders of magnitude lower in intensity than the ${}^1P_1 \rightarrow {}^1S_0$ transition [36], and in all measurements performed during this work, it is obscured by strontium monohydroxide emission at around the same wavelength.

2.2.2 Molecular Spectrum

As in an atom, electrons in a molecule are also constrained to discrete energy levels, and they may also transition among these levels through the radiative mechanisms mentioned above. The electronic state in the strontium monohydroxide molecule is mainly determined by a non-bonding electron localized in the strontium atom [30]. It is this electron that transitions between the ground state ($X^2\Sigma^+$) and the lower excited states ($A^2\Pi$ and $B^2\Sigma^+$) where the Π state is doubly degenerate, and the Σ states have no degeneracy [38]. In addition, internal energy is also stored in the motions of a molecule’s atoms relative to each other. These movements are categorized as molecular rotations and vibrations and also have quantum states over which the molecule can transition. Thus, since a molecule can transition between closely spaced rotational and vibrational states in addition to electronic states simultaneously, numerous lines located near to each other in the electromagnetic spectrum result. At low spectral resolution these line clusters form seemingly continuous bands such as the ones observed in Figure 2. 1. Figure 2. 5 and Figure 2. 6 show the molecular emission features with higher resolution and at lower temperatures and pressures. In order to explain the structure of the individual transitions within each of those bands, vibrational and rotational states must be understood in detail.

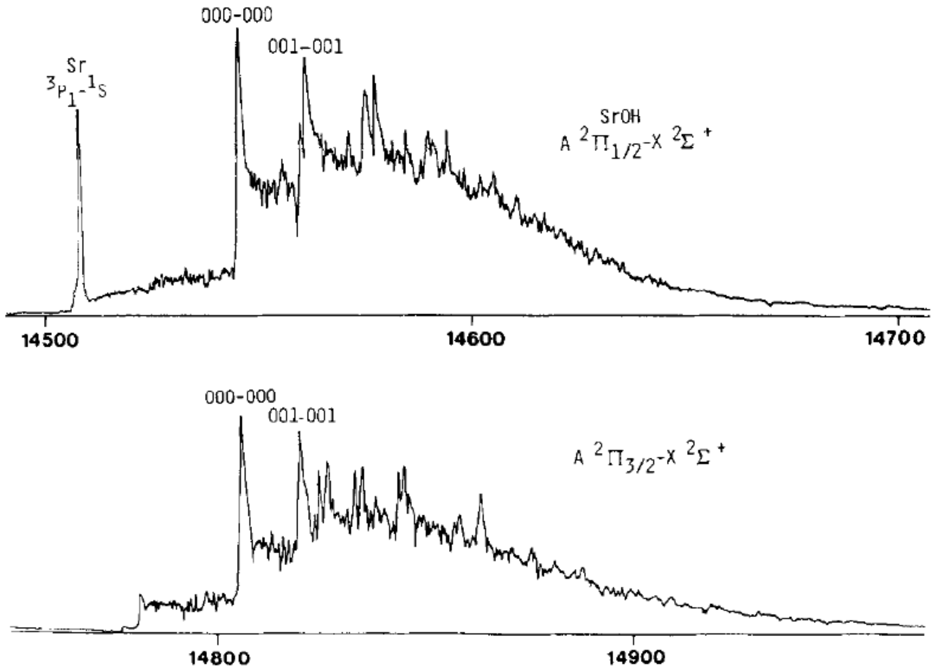

Figure 2. 5 High resolution spectrum of the $A^2\Pi \rightarrow X^2\Sigma^+$ transitions of strontium monohydroxide at 9 Torr [31]. The horizontal axis is in units of cm^{-1}.

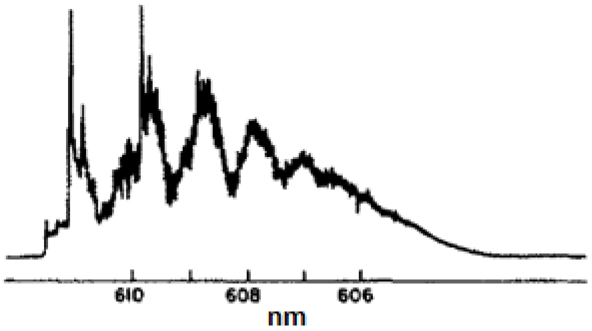

Figure 2. 6 Spectrum of emission of the strontium monohydroxide $B^2\Sigma^+ \rightarrow X^2\Sigma^+$tranisitons with a resolution of 0.14 Å at a temperature and pressure of 600 K and 3 Torr.[30].

Molecular vibrational energy results from the non-rigid nature of the bonds between atoms. In a linear triatomic molecule composed of three different elements the possible vibrations may be characterized by three normal modes, namely two stretches, which correspond to the oscillations of the bond lengths, and a bend, which describes the oscillation in the angle formed by the three atoms. This last one is doubly degenerate since it can occur in two orthogonal planes while the other ones have no degeneracy. By convention, the modes are labeled 1, 2, and 3 for Sr-O stretch, Sr-O-H bend, and O-H stretch, respectively. The energy associated with mode i can be determined by the anharmonic oscillator model, which uses an anharmonicity constant, $x_{e,i}$, and an oscillation frequency, $\overline{\omega}_{e,i}$, that characterizes the vibrational mode. The molecular vibrational energy, $G_i(v)$, for vibrational state,v_i, is given by Equation (2. 2) [37] where v_i may only have integer values.

$$G_i(v_i) = \left(v_i + \frac{1}{2}\right)\overline{\omega}_{e,i} - (v_i + \frac{1}{2})^2\overline{\omega}_{e,i}x_{e,i} \tag{2. 2}$$

To a first degree approximation every vibration mode can be assumed to be independent of the others, and consequently, the energy associated with each mode can be evaluated with Equation (2. 2). If the vibrational energy was to be determined more rigorously, however, for a given vibrational mode higher order terms that are associated with the vibrational states of the other modes would be added to this expression. In the case of strontium monohydroxide, however, the needed anharmonic constants required to perform such a detailed spectroscopic analysis have not been reported in literature.

In a radiative molecular electronic transition, vibrational state changes have different probabilities of occurring. The Franck-Condon principle states which vibrational transitions are more likely to take place. It says that the time scale of the electronic transition is much smaller than the time scale of the nuclear motion, and therefore the nuclei remain in the same positions before and after the transition. Consequently, the overlap of potential energy curves of the electronic states determines the likelihood of each vibrational transition. Figure 2. 7 illustrates this notion. In the case shown, the relative position of the atoms in the initial vibrational level of the ground electronic state is most likely to occur at a higher vibrational level of the excited electronic state, and therefore, the vibrational transition $\Delta\nu = 2$ is most likely to occur with the electronic transition. In the case of strontium monohydroxide, since the electron that transitions between the ground and the lowest excited levels is a non-bonding electron localized in the strontium atom, the bonds are not significantly affected by the electronic state, and the potential energy curves are very similar in shape and horizontal position [30]. Therefore, the transitions $\Delta\nu = 0$ are the most likely to occur. This has been confirmed experimentally for the mentioned electronic transitions [30, 31]. Since the vibrational frequencies change only slightly with electronic state, the vibrational structure is thus determined mostly by the very small changes in $\overline{\omega}_e$ that result.

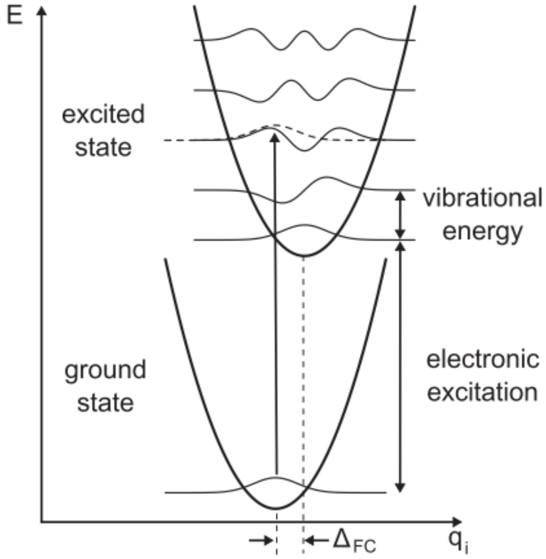

Figure 2. 7 Franck-Condon principle in absorption [39]. The horizontal axis represents the relative spatial coordinates of the atoms in the molecule, and the vertical axis represents potential energy

Each of these rovibronic transitions also has rotational structure associated with it. A molecule's rotational energy is proportional to its moment of inertia, which in a first order approximation can be calculated by considering the nuclei in the molecule to be point masses and ignoring any effect the electrons may have. Thus as a linear molecule [30, 40], strontium monohydroxide can store energy by rotating around two different axes, as a macroscopic object might, but the magnitude and direction of the rotations are quantized. The magnitude of the rotational energy in terms of wavenumber, $F(J)$, is given by Equation (2. 3) [37]. Here J is the rotational quantum number. B_v is the rotational constant, and it depends on the molecule's moment of inertia. In the second term D_v is the centrifugal distortion constant and it accounts for the change in moment of inertia that the molecule may undergo due to the atoms' separation caused by centrifugal forces. The subscript v is appended to both of these variables to indicate that the quantity that they represent can be dependent on vibrational (and electronic) state, since average bond distances change as the oscillations grow in amplitude with vibrational state thus affecting the moment of inertia of the molecule.

$$F(J) = B_v J(J+1) - D_v J^2 (J+1)^2 \tag{2. 3}$$

The degeneracy, g_J, of each rotational state results from the direction of rotation being quantized, and it is given by:

$$g_J = 2J + 1 \tag{2. 4}$$

Although this rotational model provides useful results for some purposes, in order to more accurately locate each of the transition lines in the molecular bands of strontium monohydroxide, the electrons' orbital and spin angular momentum must be considered as well. This requires the vectorial addition of orbital, spin, and rotation angular momenta. Two different coupling cases must be used to characterize the rotational structure of transitions between the two lowest excited states and the ground state of strontium monohydroxide. The discussion that follows on this topic is based on the one given by Herzberg [41].

The ground state, $X^2\Sigma^+$, and the second lowest excited state, $B^2\Sigma^+$, are described by Hund's coupling case (b). Here, the spin angular momentum is weakly coupled to the internuclear axis, and therefore, it cannot be directly added to the orbital angular momentum. Instead, the orbital and nuclear rotation angular momenta are added first, which results in a vector characterized by the quantum number K, and that vectorial result is then added to the spin orbital momentum to produce the total angular momentum vector. The rotational energy expressions incorporate a splitting constant, γ, and are given by:

$$F_1(K) = B_v K(K+1) + 0.5\gamma K \tag{2. 5}$$

$$F_2(K) = B_v K(K+1) - 0.5\gamma (K+1) \tag{2. 6}$$

Hund's case (a) describes the $A^2\Pi$ state [31]. Here the nuclear rotation of the molecule and the electronic motions do not interact strongly with each other. As a result, the components of the spin and the orbital angular momenta along the axis that crosses the three atoms in the molecule can be added directly, which results in a vector characterized by the quantum number Ω. Both components may have equal or opposing directions, which creates two different energy levels, and correspondingly, two values for Ω. The resulting total angular momentum is also characterized by J, as before, and the rotational energy for each of the levels is given by Equations (2. 7) and (2. 8), where ${B_{\mathrm{eff}}}^{(1)}$and ${B_{\mathrm{eff}}}^{(2)}$ are different effective rotational constants that factor in different effects.

$$F_1(J) = {B_{\mathrm{eff}}}^{(1)} J(J+1) \tag{2. 7}$$

$$F_2(J) = {B_{\mathrm{eff}}}^{(2)} J(J+1) \tag{2. 8}$$

By calculating the vibrational and rotational energies of a molecular state, as described above, and with knowledge of its electronic energy, the total internal energy difference between the initial and final states in a molecular transition can be found. The Born-Oppenheimer approximation provides an adequate point of departure for this calculation. In it the appropriate rotational and vibrational energy expressions can be linearly combined along with the electronic energy to find the total internal energy of a given molecular state. Differences between the two states of a transition can then be found along with selection rules, which determine the allowed radiative transitions, to predict the locations of transition lines in the electromagnetic spectrum using Equation (2. 1).

In the case of the $B^2\Sigma^+$ - $X^2\Sigma^+$ transition, Equations (2. 5) and (2. 6) need to be used. The selection rules allow for $\Delta K = \pm 1$ transitions only, and thus the most important transitions are composed of two main doublet branches, R and P, which are given by:

$$R_1(K) = \nu_0 + {F_1}'(K+1) - {F_1}''(K) \tag{2. 9}$$

$$R_2(K) = \nu_0 + {F_2}'(K+1) - {F_2}''(K) \tag{2. 10}$$

$$P_1(K) = \nu_0 + {F_1}'(K-1) - {F_1}''(K) \tag{2. 11}$$

$$P_2(K) = \nu_0 + {F_2}'(K-1) - {F_2}''(K) \tag{2. 12}$$

ν_0 is the origin of the band and is determined by the addition of the electronic and vibrational energy differences. Following the standard nomenclature used previously, $'$ and $''$ indicate the energy term belonging to the higher state and lower states, respectively.

The selection rules in the $A^2\Pi$ - $X^2\Sigma^+$ transition are $\Delta J = 0, \pm 1$, and the twelve branches determined by Equations (2. 13) to (2. 14) are produced as a result. In these expressions ${\nu_0}^{(1)}$ and ${\nu_0}^{(2)}$ indicate the band origin of the two bands produced by the two different values of Ω.

$$P_1(J) = {\nu_0}^{(1)} + {F_1}'(J-1) - {F_1}''(J) \tag{2. 13}$$

$$Q_1(J) = {\nu_0}^{(1)} + {F_1}'(J) - {F_1}''(J) \tag{2. 14}$$

$$R_1(J) = {\nu_0}^{(1)} + {F_1}'(J+1) - {F_1}''(J) \tag{2. 15}$$

$$P_{12}(J) = {\nu_0}^{(1)} + {F_1}'(J-1) - {F_2}''(J) \tag{2. 16}$$

$$Q_{12}(J) = {\nu_0}^{(1)} + {F_1}'(J) - {F_2}''(J) \tag{2. 17}$$

$$R_{12}(J) = {\nu_0}^{(1)} + {F_1}'(J+1) - {F_2}''(J) \tag{2. 18}$$

$$P_2(J) = {\nu_0}^{(2)} + {F_2}'(J-1) - {F_2}''(J) \tag{2. 19}$$

$$Q_2(J) = {\nu_0}^{(2)} + {F_2}'(J) - {F_2}''(J) \tag{2. 20}$$

$$R_2(J) = {\nu_0}^{(2)} + {F_2}'(J+1) - {F_2}''(J) \tag{2. 21}$$

$$P_{21}(J) = {\nu_0}^{(2)} + {F_2}'(J-1) - {F_1}''(J) \tag{2. 22}$$

$$Q_{21}(J) = {\nu_0}^{(2)} + {F_2}'(J) - {F_1}''(J) \tag{2. 23}$$

$$R_{21}(J) = {\nu_0}^{(2)} + {F_2}'(J+1) - {F_1}''(J) \tag{2. 24}$$

A coarse model based on these principles was developed in order to synthesize the available spectral information of strontium monohydroxide. The first term of Equation (2. 2) was used in order to find vibrational energy terms of each state, and the second and higher order terms were ignored because the required constants have not been reported in literature. Only $\Delta\nu = 0$ transitions were considered for the Sr-O stretch and the Sr-O-H bend, since these are heavily favored by the Franck-Condon principle [30, 31]. The O-H stretch was neglected because its excitation energy is an order of magnitude higher than the other two modes, and its vibrational constant is unlikely to change with electronic state, which renders its contribution to the total vibrational term trivial. Equations (2. 5)-(2. 24) were applied to the $A^2\Pi$ - $X^2\Sigma^+$ and $B^2\Sigma^+$ - $X^2\Sigma^+$ transitions, as appropriate, with the pertinent selection rules. The constants used are summarized in Table 2. 1. The relevant results from this model are discussed in Chapter 4.

Table 2. 1 Spectroscopic constants used for finding the approximate spectral location of some of the strontium monohydroxide rovibronic transitions [30, 31, 42]. All units in cm^{-1}.

	$X^2\Sigma^+$	$A^2\Pi_{1/2}$	$A^2\Pi_{3/2}$	$B^2\Sigma^+$
T_0	0	14542.25	14805.84	16377.51
$\bar{\omega}_{\mathrm{Sr-O}}$	522	544	544	582
$\bar{\omega}_{\mathrm{Sr-O-H}}$	360	375*	375*	397
B_v	0.2492	-	-	0.2522
γ	2.427E-3	-	-	-0.1447
B_{eff}	-	0.2538	0.2538	-

* Values not reported in literature. An estimate was made.

Although this model provides an understanding of the structure of the molecular spectrum measured in this study, the description given is not sufficient to predict all the molecular transitions between the ground and the two lowest excited electronic states of strontium monohydroxide with complete accuracy. There is a number of additional angular momentum couplings and perturbation effects that produce additional transitions and splitting of the energy levels. Further, the molecular constants needed to calculate the different energy levels have only been characterized for the lower vibrational and rotational excited levels. This is because of the high density of transitions within each band caused in great part by the small differences in vibrational energies between the different states, as mentioned earlier. This creates an inherent difficulty when studying the molecular structure at higher rotational and vibrational temperatures; when exciting higher states, more overlapping transitions are observed as well. It is likely for this reason that literature on the subject is scarce.

2.2.3 Line Broadening

As discussed, the position of an emission or absorption line in the electromagnetic spectrum is determined by the energy difference between the initial and final states of the related transition. The width of such a line in the spectrum is finite and is determined by three independent broadening processes. Namely, these processes are natural, collision, and Doppler broadenings.

Natural line broadening results from quantum mechanical considerations. Heisenberg's uncertainty principle dictates that some measurable quantities can only be determined with a limited degree of certainty. This is an intrinsic feature of any quantum state [43], and applies beyond experimental limitations. More specifically, the precision to which a variable can be known is inversely proportional to that of its complementary variable, if it has one. Position and momentum are perhaps the best known example of a complementary variable pair. Time and energy are, in fact, also complementary variables, and thus in the current context, the uncertainty of the energy of an atomic or molecular state is limited by its lifetime. The uncertainty in wavelength that results from the energy uncertainty is manifested by the broadening of the emission or absorption line. The magnitude of natural broadening, however, is typically very small when compared to the other two broadening mechanisms.

The frequent collisions that atoms and molecules undergo cause broadening of emission and absorption lines as well. During impact with each other, the particles' electronic and molecular configurations are affected slightly due to the interactions of their electron clouds, which alters the energy of their internal states. If a particle undergoes a radiative transition while such an interaction is taking place, the wavelength of the photon involved in the process will be affected accordingly. Photons for a given transition will have slightly different wavelengths, and in aggregate, when measuring that transition in a medium, a wavelength distribution that is dependent on the gas conditions results. It is also possible for the peak of this distribution to shift away from the wavelength associated with the undisturbed particle, but this shift is typically smaller than the broadening itself.

The Doppler effect also creates a wavelength distribution for any particular transition. The wavelength of an emitted photon is different in the reference frame of the emitter than it is to a stationary observer. If the emitter is moving towards the observer, the wavelength of the emitted particle will appear shorter to the observer, and if the emitter is moving away from the observer, it will appear longer. The same principle can be applied to explain absorption line broadening. The Boltzmann-Maxwell equation predicts the distribution of the velocities of particles in a gas at a given temperature, and from it the Doppler broadening can be determined.

While line broadening is often an important aspect to consider in spectroscopic studies, the measurements performed in this work do not have the resolution required to perform detailed quantitative assessments based on its theoretical principles.

2.2.4 The Radiation Spectral Intensity of an Emitting Gas

While the wavelength of the photons with which a particular atom or molecule interacts depends primarily on the species' internal electronic and molecular structure, the number of photons involved in the transition per unit time, which directly determines the intensity of the radiation emitted or absorbed, depends on two factors: the probability that the particular radiative transitions will occur, and the concentration of molecules or atoms at the initial state of the transition. By determining these two quantities, the intensity of the radiation at any point in space may be determined.

The first one of these, the probability of transition, is inherent to the particular combination of species, energy state, and type of transition being considered. It is useful to characterize this probability with an Einstein coefficient, a quantity that defines the rate of transition of molecules or atoms. The spontaneous emission Einstein coefficient, A_{21}, indicates the proportion of atoms or molecules that will decay from a high energy level to a lower one per unit time. The absorption Einstein coefficient, B_{12}, quantifies the proportion of particles that will be excited per unit time and per unit of radiative energy density of the needed wavelength in the medium. Equivalently, the induced emission Einstein coefficient, B_{21}, describes the proportion of particles that will decay normalized by the same quantities as B_{12} is. These three coefficients are determined by quantum mechanical aspects and are independent of classically described events on which quantities such as temperature and pressure are defined.

The intensity of radiation emitted or absorbed is also determined by the concentration of excited molecules or atoms that are at the initial level of the transition with which the radiation is associated. The proportion of particles of a given species at any given internal energy state in a gas can be found with the Boltzmann distribution:

$$\frac{N_i}{N} = \frac{g_i}{Q_e(T)} e^{\left(-E_i/_{kT_{\text{ex}}}\right)} \tag{2. 25}$$

Here, N is the total number density of particles of the species of interest, N_i is the number density of particles of the same species at energy level i, g_i is the degeneracy of the same electronic energy level, E_i is the magnitude of that level above the ground state, k is the

Boltzmann constant, and T_{ex} is the excitation temperature of the gas. Q is a quantity called the electronic partition function, and it represents the addition of all the possible internal energy states of that particle $\left(Q = \sum_i g_i e^{\left(-E_i/_{kT_{\mathrm{ex}}}\right)}\right)$. For atoms, the electronic partition is generally well characterized and can be found with temperature dependent expressions available in literature (e.g. [44]).

In order to find the proportion of molecules of a given species at a particular energy level, the three different internal energies must be taken into account. With the Born-Oppenheimer approximation, three factors of the same form as the right side of Equation (2. 25) (one for each of the internal energy modes of a molecule) are multiplied together.

It is worth noting at this point that excitation temperature, T_{ex}, is conceptually different from kinetic temperature. While the former is a measure of the internal energy states of particles in a medium and is the one that the diagnostic presented in this work measures, the latter quantifies the average kinetic energy of those particles and is the more useful of the two in the study of IC engines[2]. Both quantities must have the same value in order for the studied diagnostic to serve its purpose, and this only occurs if the medium in question is in thermal equilibrium.

In the most rigorous sense, thermal equilibrium is generally not attained in a flame with fluorescent thermally-excited particles in the absence of an irradiation source, but a state sufficiently close to it for practical purposes is often reached. While collisional excitation and de-excitation rapidly reach the same rates, radiative processes are not equilibrated because the radiative de-excitation is not balanced by radiative excitation. This imbalance leads to the underpopulation of excited states and, consequently, lower excitation temperature than kinetic temperature. However, if inelastic collisions occur at a much faster rate than the radiative processes, as is often the case in combustion, collisional processes dominate the distribution of energy states, and the effect of the unbalanced radiative de-excitation on equilibrium becomes less important. In that case, both excitation and kinetic temperature acquire adequately similar values.

The fluorescence efficiency is a useful quantity in determining whether a gas can be reasonably approximated to be in thermal equilibrium. As defined in Equation (2. 26), where Q_{21}

---

[2] Kinetic temperature is the one referred to in Chapter 1.

is the collisional de-excitation rate, fluorescence efficiency, Y, is the ratio of the radiative de-excitation rate to the total de-excitation rate.

$$Y = \frac{A_{21}}{A_{21} + Q_{21}} \tag{2. 26}$$

This expression is valid in optically thin media in the absence of external radiation sources. As a reference, a sodium atom in a flame at ambient pressure and a kinetic temperature of 2200 K has a fluorescence efficiency value of 0.04 for the transition from its first excited state to its ground state. This efficiency translates into a kinetic and excitation temperature difference of 8 K, and the difference becomes even smaller at the higher pressures in an IC engine [27]. With such a small difference between them, kinetic and excitation temperatures can be considered to be equal for all practical purposes. Given that the A_{21} values of the relevant transitions of strontium and strontium monohydroxide are similar in magnitude to those of the mentioned atomic sodium transition [45-48], if the fluorescence efficiencies of the strontium species in a flame are similarly small, these species can also be safely approximated to be in thermal equilibrium, and the spectral intensity of their radiative emission can be directly related to their medium's kinetic temperature.

This is likely to be the case for both strontium and strontium monohydroxide in the burnt gases of an engine although not to the same extent as for atomic sodium. The fluorescence efficiency of atomic strontium has been reported to be about 0.1 at ambient pressure in $H_2/O_2/N_2$, $H_2/O_2/Ar$, and $CO/N_2O/N_2$ flames [49, 50]. All the species that are expected to be strontium's main collision partners in an engine cylinder were considered in these studies. Strontium monohydroxide fluorescence efficiency, on the other hand, has not been investigated directly, to the author's knowledge, but from studies of calcium monohydroxide a reasonable approximation may be inferred due to the similarities of both molecules in electronic structure. Calcium monohydroxide's fluorescence intensity was also found to be around 0.1 in $H_2/O_2/Ar$ stoichiometric flames and was lower in rich flames of the same composition [51]. These results do not take into consideration the quenching effect of carbon dioxide and molecular nitrogen, which, as suggested by Laser-Induced Saturation Fluorescence studies of strontium monohydroxide in C_2H_4/Air diffusion flames [52], are likely to decrease the fluorescence efficiency of this molecule even further. *For these reasons, excitation and kinetic temperatures will be assumed to be undifferentiated for the purposes of this work and will be referred to without specificity from this point forward in the present document.*

The Einstein coefficients and, in thermal equilibrium, the Boltzmann distribution constitute the building blocks of the expression with which the energy density of radiation of a particular wavelength can be calculated. The following treatment to arrive at the calculation of spectral intensity largely follows the ones by Linne [53] and Rybicki et al. [54]. Simplifications and assumptions are made as applicable to the conditions and characteristics of the development and intended application of the diagnostic studied.

The steady-state spatial conservation of energy of wavelength λ in radiatively participating media with negligible scattering can be given by the following equation:

$$\vec{\nabla} \cdot \rho_\lambda \vec{c} = \frac{hc}{\lambda}\left(N_2 A_{21} + \rho_\lambda (N_2 B_{21} - N_1 B_{12})\right) \tag{2. 27}$$

Here, $\vec{c}$ is the velocity of light, and ρ_λ is the energy density of radiation at the wavelength at which the particle emits and absorbs. This expression neglects line broadening due to Doppler, natural, or collisional effects. Equation (2. 27) can be used to determine the total intensity of any particular atomic or molecular line in the spectrum as long as the Einstein coefficients and the excitation energies of every state involved are known. Simplifying for radiation traveling along the line-of-sight of an optical detector, and assuming that the medium emits and absorbs energy isotropically, Equation (2. 27) becomes

$$\frac{dJ_\lambda}{dz} = \frac{hc}{4\pi\lambda} N_2 A_{21} + \frac{h}{\lambda} N_2 B_{21} J_\lambda - \frac{h}{\lambda} N_1 B_{12} J_\lambda \tag{2. 28}$$

Thus, radiance, J_λ, changes spatially along distance, z. This change is determined by the linear combination of spontaneous emission, induced emission, and absorption. Note that when applying this equation rigorously, the concentrations of species at the higher and lower levels, N_2 and N_1, are dependent on location, z, if the medium is heterogeneous. However, assuming these quantitates to be spatially uniform when applying the expression to a heterogeneous medium is equivalent to applying their line-of-sight average.

Further, it is convenient to simplify Equation (2. 28) by defining an emission coefficient, ε_λ, an absorption coefficient, κ_λ, and a source function S_λ:

$$\varepsilon_\lambda = \frac{hc}{4\pi\lambda} N_2 A_{21} \tag{2. 29}$$

$$\kappa_\lambda = \frac{h}{\lambda}(N_1 B_{12} - N_2 B_{21}) \tag{2. 30}$$

$$S_\lambda = \frac{\varepsilon_\lambda}{\kappa_\lambda} \tag{2. 31}$$

In addition, the line-of-sight average of the optical depth, τ_λ, is given by the product of the absorption coefficient and the path length, l:

$$\tau_\lambda = \kappa_\lambda l \tag{2. 32}$$

With these definitions, Equation (2. 28) becomes:

$$\frac{dJ_\lambda}{d\tau_\lambda} + J_\lambda = S_\lambda \tag{2. 33}$$

Finally, solving this differential equation while applying the boundary condition $J_\lambda(0) = 0$, which applies when there is no external source of radiation, results in Equation (2. 34)

$$J_\lambda = S_\lambda(1 - e^{-\tau_\lambda}) \tag{2. 34}$$

The optical depth in the above expression implicitly contains the total path length and the total number density of active species (by substituting Equations (2. 32), (2. 30), and (2. 25)), which are parameters that depend on the experimental conditions. Figure 2. 8 illustrates the role that the product of these two quantities plays in the intensity of emission, in this case, for the transition $^1P_1 \rightarrow {}^1S_0$ of atomic strontium at 2000 K. Although the scales change for other species, transitions, and to a smaller extent, gas conditions, the general trend is the same. The most notable aspect is that for lower values of lN its relationship with J_λ is initially linear, but as the magnitude of this product increases, radiance eventually becomes constant. When a medium is in the regime characterized by the linear relationship, it is said to be optically thin, and when radiance is constant, the medium is optically thick.

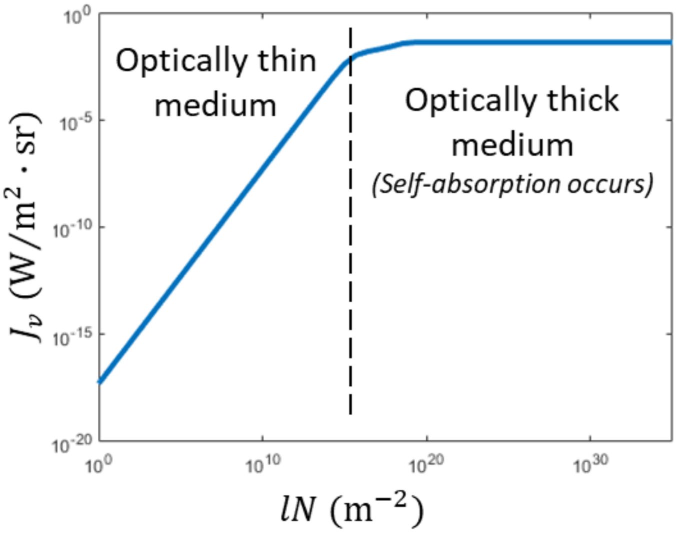

Figure 2. 8 Intensity of the $^1P_1 \rightarrow {}^1S_0$ strontium transition as a function of the product of path length and number density at 2000K.

The optical thickness of the medium is of high significance for the application of spectroscopy in combustion diagnostics. In the optically thin regime, a spontaneously emitted photon is unlikely to collide with a particle of the emitting species before leaving the medium. Conversely, when the medium is optically thick self-absorption occurs; photons are trapped in the medium, and only the ones close to the boundaries of the volumetric domain can be detected. If information for the entirety of this domain is to be obtained, the medium in question must be optically thin.

A simplified relationship for the optically thin regime can be expressed mathematically by linearizing Equation (2. 34) for small values of τ_λ:

$$J_\lambda \approx S_\lambda\big(1 - (1 - \tau_\lambda)\big) = S_\lambda \tau_\lambda = \varepsilon_\lambda l \qquad (2.\ 35)$$

Note that this result is equivalent to integrating Equation (2. 28) while neglecting absorption and induced emission. In both cases, substituting N_2 using Equation (2. 25) the expression for radiance becomes:

$$J_\lambda = \frac{hc}{4\pi\lambda} A_{21,\lambda} l N \frac{g_\lambda}{Q(T)} e^{\left(-E_\lambda/_{kT}\right)} \tag{2. 36}$$

Here the subscript λ has been added to the Einstein emission coefficient and has replaced i in Equation (2. 25) to denote that the quantities to which it is appended are associated to a specific finite wavelength. An assessment of the medium in the presented diagnostic shows that, in general, it can be assumed to be optically thin. The details of the justifying calculations are presented along with the experimental descriptions at the end of Subsection 3.1.2.

2.3 Measuring Scalar Quantities

Equation (2. 36) shows that, if a medium is optically thin, radiance is dependent on emitting species number density and gas temperature. This is, in fact, the basis for using measurements of the intensity of spontaneously emitted radiation as a tool to measure scalar quantities in a gas. However, as will be discussed next, a diagnostic method greatly benefits in simplicity and robustness when measurements at two different wavelengths are performed simultaneously.

2.3.1 Temperature

The ratio of the radiance of emission by the same species at two different wavelengths is given by Equation (2. 37). Here, the subscripts λ_i and λ_j serve to associate each of the variables with one of two distinct spectral features. For the purposes of the current study, these features can be any two of the three strontium monohydroxide bands previously described.

$$\frac{J_{\lambda_i}}{J_{\lambda_j}} = \frac{g_{\lambda_i} A_{21,\lambda_i} \lambda_j}{g_{\lambda_j} A_{21,\lambda_j} \lambda_i} e^{\left(E_{\lambda_j} - E_{\lambda_i}/_{kT}\right)} \tag{2. 37}$$

Thus, a quantity dependent on temperature simpler than Equation (2. 36) results. Most notably, the partition function and number density of the emitting species, both of which can be difficult to determine, are no longer required. Further, the resulting pre-exponential factor is inherent to the transitions involved and independent from experimental conditions.

In practice, however, measuring the intensity of single molecular emission lines to obtain the intensity ratio exactly as expressed in Equation (2. 37) is not a realistic objective for the current study. As discussed previously, the rovibronic spectrum of strontium monohydroxide is extremely congested, and as a consequence, the bandwidth of any band pass filter used to measure a portion of the visible emission spectrum of this molecule will measure the integrated intensity of several lines. In addition, in order to eventually obtain high intensity images of the quantities of interest, a wide detection wavelength window might be desirable. These issue are further compounded by line broadening since, depending on gas conditions at the time of emission, different lines close to the edges of the wavelength detection window would be detected to different degrees within a given wavelength detection window.

Despite these difficulties, some assumptions are made in the present work in order to obtain a useful temperature-dependent result. The excitation energy of the rovibronic spectrum of strontium monohydroxide is dominated by the electronic excitation energy [42], as is generally the case with most molecules. Therefore, lines in a given electronic band can be considered to correspond to transitions originating from upper states with equal excitation energies. Yet, when calculating the ratio of intensities of two bands, it is necessary to use a nominal energy difference, $\Delta E_{ji,w}$, that is adequately descriptive of the specific transitions included in the calculation. The subscript ji has been appended to this variable, and later to others, to indicate that the quantity that each represents is particular to the two spectral features used in Equation (2. 37), and w indicates that it is dependent on the detection window width. Note that the operator of $\Delta E_{ji,w}$ is not linear, and therefore in strict terms, an arithmetic mean of the excitation energies would not yield correct results. However, it is assumed that these excitation energies are close enough to each other for any errors caused by this coarse treatment to be negligible.

It is also important to use a suitable feature-specific and detection-bandwidth-specific pre-exponential factor, $K_{\lambda_i,w}$. This factor is the summation of the pre-exponential factors of all the transitions captured in a given detection band, w, and is defined in Equation (2. 38).

$$K_{\lambda_i,w} = \sum_k f_{i,k} g_{\lambda_{i,k}} A_{21,\lambda_{i,k}} \lambda_{i,k} \qquad (2.\ 38)$$

The dimensionless factor, $f_{i,k}$, is included in order to account for the relative efficiency with which emission from an individual line is collected. Both, the band shape of a hypothetical band pass filter used to capture the band intensity and the extent to which lines at the edges of the wavelength detection window are measured can be taken into consideration in this way. $K_{\lambda_j,w}$ is defined equivalently by replacing the corresponding subscript in this expression.

With these representative quantities, the intensity ratio between two bands can be approximated as:

$$\frac{J_{\lambda_{i,w}}}{J_{\lambda_{j,w}}} \approx \frac{K_{\lambda_i,w}}{K_{\lambda_j,w}} e^{\left(\Delta E_{ji,w}/_{kT}\right)} \qquad (2.\ 39)$$

Taking the natural logarithm of this Equation, the following expression is obtained

$$\ln\left(\frac{J_{\lambda_{i,w}}}{J_{\lambda_{j,w}}}\right) = b_{ji,w} + \frac{m_{ji,w}}{T} \qquad (2.\ 40)$$

where,

$$m_{ji,w} = \frac{\Delta E_{ji,w}}{k} \qquad (2.\ 41)$$

$$b_{ji,w} = \ln\left(\frac{K_{\lambda_i,w}}{K_{\lambda_j,w}}\right) \qquad (2.\ 42)$$

Finally, solving for temperature,

$$T = \frac{m_{ji,w}}{\ln\left(J_{\lambda_{i,w}}/J_{\lambda_{j,w}}\right) - b_{ji,w}} \qquad (2.\ 43)$$

In order to find the quantities $m_{ji,w}$ and $b_{ji,w}$ so that temperature can be determined, a calibration process is required. This is done in this study by performing spectral measurements of a strontium monohydroxide-containing gas at predicted conditions. Then, as expressed in Equation (2. 40), a linear regression of the natural logarithm of the intensity ratio and the inverse of temperature yields the required constants, which may be used in Equation (2. 43).

It is also useful to consider the sensitivity of the temperature measurement technique from the calibration constants in order to obtain a way to assess the performance of the method. This can be obtained by calculating the derivative of the intensity ratio with respect to temperature, as expressed in the following Equation:

$$\frac{\mathrm{d}\left({J_{\lambda_{i,w}}}/{J_{\lambda_{j,w}}}\right)}{\mathrm{d}T} \approx -\frac{e^{b_{ji,w}} m_{ji,w}}{T^2} e^{\left({m_{ji,w}}/{T}\right)} \tag{2. 44}$$

It can be seen that sensitivity depends in great part on $m_{ji,w}$ due to its presence in the exponential and in the pre-exponential factor of this expression. This quantity is determined entirely by the difference in excitation energies, $\Delta E_{ji,w}$.

2.3.2 Equivalence Ratio

Determination of equivalence ratio is rather more involved. Once again departing from Equation (2. 36), it can be seen that the intensity ratio of lines emitted by two different species in the optically thin regime is given by Equation (2. 45). In this case, subscripts a and b are added to the different variables in order to indicate that the quantities belong to two different species or the associated wavelengths of their transitions. In this work, a may indicate relation with atomic strontium or its emission feature at 460.7 nm, and b may refer to strontium monohydroxide or any three of its three spectral bands.

$$\frac{J_{\lambda_a}}{J_{\lambda_b}} = \frac{g_{\lambda_a} A_{21,\lambda_a} \lambda_b}{g_{\lambda_b} A_{21,\lambda_b} \lambda_a} \frac{Q_b(T)}{Q_a(T)} \frac{N_a}{N_b} e^{\left({E_{\lambda_b} - E_{\lambda_a}}/{kT}\right)} \tag{2. 45}$$

A form of this equation that is useful for calibration purposes may be obtained by applying the same treatment as the one discussed in the previous subsection. Grouping all constants into the factors $K_{\lambda_a,w}$ and $K_{\lambda_b,w}$, which are defined by appropriately substituting the subscripts in Equation (2. 38), the expression thus may become:

$$\frac{J_{\lambda_a}}{J_{\lambda_b}} = \frac{K_{\lambda_a,w}}{K_{\lambda_b,w}} \frac{Q_b(T)}{Q_a(T)} \frac{N_a}{N_b} e^{\left(E_{\lambda_b} - E_{\lambda_a} /_{kT} \right)} \tag{2. 46}$$

Taking the natural logarithm then results in:

$$\ln\left(\frac{J_{\lambda_{a,w}}}{J_{\lambda_{b,w}}}\right) - \ln\left(\frac{N_a}{N_b}\right) - \ln\left(\frac{Q_b(T)}{Q_a(T)}\right) = b_{ba,w} + \frac{m_{ba,w}}{T} \tag{2. 47}$$

Similarly, the constants $b_{ba,w}$ and $m_{ba,w}$, which are defined by correspondingly changing the subscripts in Equations (2. 41), (2. 42), (2. 38), and (2. 39) must be established experimentally. This time, however, in addition to the measured intensity ratio, $\frac{J_{\lambda_{a,w}}}{J_{\lambda_{b,w}}}$, the concentration ratio, $\frac{N_a}{N_b}$, and the partition function ratio, $\frac{Q_b(T)}{Q_a(T)}$, must be determined as well. The concentration ratio may be found with equilibrium calculations such as the ones described in Section 2.1. In order to do this, the temperature, pressure, and equivalence ratio in the chamber at the time that the spectral measurements are performed must be known. The ratio of partition functions must be determined by calculating the partition function of each species separately. Thus, having determined the gas conditions and all quantities on the left side of the equation, a regression may once again be performed in order to find the needed parameters.

Finally, to determine equivalence ratio by means of the presented diagnostic, $\frac{N_a}{N_b}$ would have to be solved for in Equation (2. 47) and calculated from optical measurements along with the gas temperature determined from Equation (2. 43) or otherwise. Then, equilibrium calculations would yield the answer sought.

2.4 Summary of Assumptions

Although the spectral measurement of molecular emission as an optical diagnostics technique offers important advantages for the determination of scalar quantities in IC engines, several challenges arise from using unresolved spectral bands emitted by a largely uncharacterized species such as strontium monohydroxide that has been thermally excited. Spectroscopic constants, collisional cross sections in combustion environments, and Einstein coefficients, among other quantities, have generally remained unreported for this molecule, and as a result, the relative importance of some of the relevant physical processes that take place while the events to be diagnosed are occurring is still unclear to some extent. An effort has been made to create a complete model of the pertinent processes, as described in the earlier Sections of this Chapter, but the necessary supporting evidence to justify some of its features is less than conclusive. A portion of the current work is, therefore, dedicated to the evaluation of the validity of some of the assumptions made, all of which are summarized in this Section.

Some of these assumptions are readily apparent in the key mathematical expression that relate some of the most important quantities. The application of Equations (2. 40) and (2. 47) to calculate gas temperature and equivalence ratio presumes the existence of the quantities $\Delta E_{ji,w}$ and $\Delta E_{ba,w}$. This implies that the excitation energy of all the transitions that fall within the detection window in a given band is very similar. This is very likely to be the case since electronic excitation energy, which is the same for all transitions in a band, contributes significantly more to the total excitation energy than vibrational and rotational energies. Nevertheless, an effort to estimate these individual excitation energies based on the concepts described in Subsection 2.2.2 is discussed in Chapter 4.

A more inconspicuous issue associated with the same quantity is that the line broadening mechanisms described in Subsection 2.2.3 make $\Delta E_{ji,w}$ and $\Delta E_{ba,w}$, in fact, pressure dependent. This is because the broadening processes themselves are affected by this parameter, and therefore, for different pressures the spectral distribution of each transition changes. Although the width of any one transition is always negligible compared to the spectral resolution of the equipment used in this study and the wavelength detection width of a potential imaging system, the effect that broadening has on all the transitions in aggregate plays a role by influencing which transitions enter the detection band used to determine band intensity and to what extent. Given that the spectrum of strontium monohydroxide is not sufficiently characterized, the effect is difficult to predict theoretically. Additionally, since temperature and pressure cannot be varied independently in an optical engine, it is not possible to fully determine this dependency experimentally within the scope of this study. Therefore, pressure dependency of the band excitation energy difference is neglected as a starting point, and the effect of the assumption is evaluated in Chapter 4.

In addition to presumptions on individual parameters, the derivation of Equations (2. 40) and (2. 47) as a whole also assumes thermal equilibrium of the emitting species. Justification for the use of the Boltzmann distribution is provided in the discussion presented in Subsection 2.2.4. Given the uncertainties associated with the temperature measurements performed in this study (~100K), the population of excited states of molecules initially at the ground electronic state is determined in this way. However, this calculation does not take into account the possibility that strontium monohydroxide is produced, at least to some extent, in an excited state, which would result in chemiluminescence. The intensity of this radiative emission would not be taken into account in the analysis of Section 2.3, but to the author's knowledge, there are no reports of observations of strontium monohydroxide radiative emission known to be originated from chemiluminescence with certainty.

Finally, the medium is assumed to always be optically thin in the wavelengths of strontium and strontium monohydroxide emission. An analysis is presented in Chapter 3 that confirms that this is, indeed, very likely to be the case.

Chapter 3
Experimental Measurements

The diagnostic technique studied in this work offers a simplified means to obtain measurements of temperature and equivalence ratio in an IC engine. It is based on the measurement of the radiative emission from strontium combustion products to determine those quantities. Engine experiments were performed in order to assess the quantitative relationship between the spectral emission and the scalar quantities of interest. An optical engine fueled with strontium-doped ethanol was operated at different conditions and the relative spectral emission from the combustion chamber was measured. In parallel, the temperature in the chamber was calculated using a 1-D thermodynamic model. In addition, flat flame burner experiments were performed in pursuit of spectral measurements at steady-state conditions through which a fundamental picture of the key processes to consider was sought.

3.1 Engine Setup and Operation

3.1.1 Engine System Description

A single-cylinder optical engine, schematically depicted in Figure 3. 1, was used in the present study. It uses spark ignition and direct fuel injection, and it has four valves, a pent-roof chamber, and a bowl piston. One of the intake ports has a butterfly valve that permits the regulation of swirl flow. Additionally, quartz cylinder and piston windows provide ample optical access. Other mechanical details of the engine are provided in Table 3. 1.

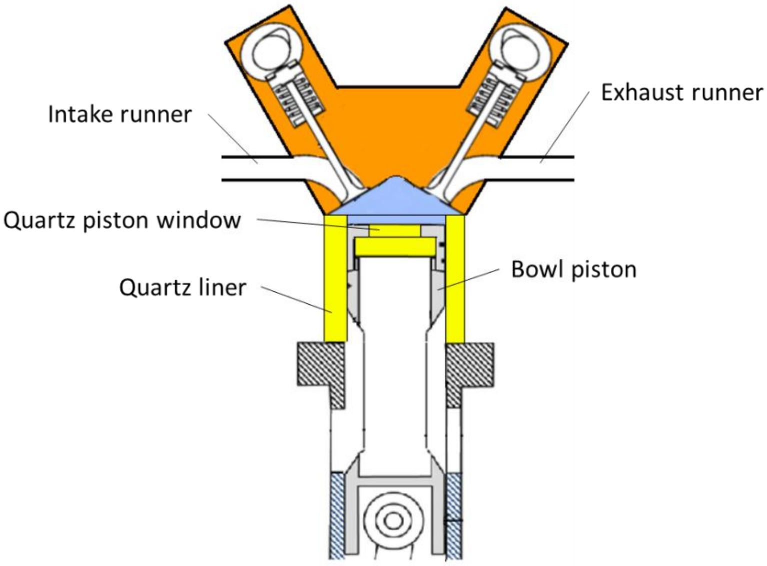

Figure 3. 1 Schematic cross section of the optical engine used in the experiments described in this work (not to scale). Adapted from [55].

Table 3. 1 Engine hardware specifications

Bore	86 mm
Stroke	86 mm
Compression ratio	8.9
Displacement	500 cm^3
Connecting rod length	159 mm
Intake Valves Opening	-357 CAD aTDC
Intake Valves Closing	-140, -129 CAD aTDC
Exhaust Valves Opening	137 CAD aTDC
Exhaust Valves Closing	-348 CAD aTDC

Consistent air flow that met the needs for reliable engine operation was ensured through specially designed intake and exhaust systems. Intake airflow was regulated with a needle valve to achieve the desired intake manifold pressure, and it was supplied to the system through an ultrasonic orifice, which ensured that the flow was constant despite pressure oscillations. The air was heated as it flowed into a plenum and maintained at temperature with electrical heaters that covered the surfaces of the pipes upstream of the combustion chamber of the engine. A small amount of air that contained suspended droplets of silicon oil was added just upstream of the plenum to provide lubrication for the piston. On the exhaust side another plenum received the gases discharged from the engine, and at its exit a ball valve was used to regulate exhaust pressure.

Thermal management of the engine was performed using systems commonly used in IC engines as well as some that are specialized for optical engines. Constant oil flow was provided to the engine head and crank case in order to lubricate the cam shaft, valve, and crank shaft mechanisms, and the head temperature was controlled with internal coolant flow. Additionally, in order to prevent damaging thermal stresses in the quartz cylinder, jets of air were directed around it externally.

Several high-speed sensors measured pressure with half-crank-angle-degree resolution throughout the entire system. A piezoelectric transducer (Kistler 6125) connected to a charge amplifier (Kistler 5010A) measured the pressure in the cylinder. Water cooled piezoresistive sensors (Kistler 4049A) measured the pressure at the exhaust port and at the exit of the exhaust plenum, and other pressure sensors (Kistler 4007B) provided the measurements at the inlet of the intake plenum, the intake runner, and the two intake ports. Many of these sensors provided redundant measurements that were useful when setting up and testing the engine system for reliable operation, but only the measurements taken at the intake ports, the cylinder, and the exhaust port were used for data analysis, as will be discussed in Section 3.2. Similarly, many other low-resolution transducers and thermocouples installed throughout the system were useful in ensuring safe engine operation and in troubleshooting technical difficulties.

3.1.2 Fuel Selection

The fuel blend to be used in the experiments was determined based on its ability to contain a sufficient amount of a strontium compound in order to produce atomic strontium and strontium monohydroxide in enough quantities during combustion for high signal-to-noise emission measurements. The solubility of strontium compounds and similar substances in hydrocarbon fuels was assessed experimentally to find an adequate mixture.

Isooctane was first considered since it is a standard laboratory-grade surrogate for gasoline, but mixing strontium compounds in this fuel proved to be extremely challenging. This is because isooctane, as a non-polar hydrocarbon, cannot dissolve strontium compounds, which are in most cases polar due to the highly ionic bonds that strontium tends to make with other elements. Two main strategies were attempted to bridge the gap in chemical polarity between these two substances in order for them to mix homogeneously.

The first one of these was the use of polyether rings known as crown ethers. These molecules tend to complexate with alkali metal and alkali earth metal atoms from ionic compounds in solution [56-58], and as a result, the metal atom is trapped in the center of a non-polar ring, which could then, in theory, dissolve in a hydrocarbon solvent. As a proof of concept, approximately equimolar amounts of 18-crown-6 and sodium chloride, and separately, the same crown ether with potassium chloride, were saturated in methanol. Alkali metals were used because the method to be used to assess the final concentration of metals in the fuel was not able to detect strontium, but if the mixing process was quantitatively demonstrated to dissolve significant amounts of a metal that has similar stability constants with the crown ether used [59], then strontium could be reasonably assumed to be dissolved in similar quantities in isooctane with the same process. In addition, methanol was chosen as a solvent because it has been demonstrated to be an adequate medium for the complexation to occur [60]. Once the crown ether and metal solutions in methanol were mixed, they were diluted in isooctane to form a 1:30 mixture of methanol:isooctane. By Inductively Coupled Plasma Atomic Emission Spectrometry tests (ASTM D5185) performed at an independent laboratory (ALS Global), however, these blends were determined to not have any significant amount of metal dissolved in them. One possible explanation for no potassium or sodium to be detected in these samples is that the methanol and the isooctane separated before the concentration tests were carried out, and the metals remained in the methanol. Then, when a sample was drawn from each of the containers, only isooctane was taken and tested. In any case, crown ethers were determined to not be a satisfactory solution to the problem of dissolving strontium in isooctane.

The second strategy attempted to accomplish this was to dissolve a metal compound in a different solvent which could then be blended with the gasoline surrogate. For this stage of the assessment, an organometallic complex, strontium acetylacetonate, was used as the strontium compound. Isooctane, methyl decanoate, methanol, ethanol, 3-pentanone, and acetone were mixed with small quantities of this strontium substance individually. Of these, the only solvent that showed readily visible signs of dissolution of the solid was ethanol. Then, a saturated solution of ethanol and strontium acetylacetonate was mixed and the ethanol was allowed to evaporate completely over three days. By comparing the initial mass of the solution to the mass of the residue left over after the ethanol had been allowed to evaporate completely, the maximum concentration of strontium acetylacetonate in ethanol was estimated to be 100 ppm by weight, which indicated a concentration of atomic strontium in the fuel of about 30 ppm by weight.

This demonstrated solubility of strontium acetylacetonate in ethanol was not sufficient for it to be blended with isooctane and obtain high intensity spectral emission of all strontium products during engine operation. The needed total concentration of strontium in the final fuel blend to be used in experiments for this to be the case had been estimated to be 400 ppm. This estimate was obtained by comparing the Einstein emission coefficients, equilibrium concentrations during combustion, and the initial concentration of metals used in previous similar experiments [27]. In lack of better results, however, it was decided to proceed with the engine experiments using the ethanol-strontium acetylacetonate mixture as fuel and assess the resulting emission intensity directly.

The preparation of the ethanol and strontium acetylacetonate blend that was ultimately used in the experiments involved a simple mixing process. An arbitrarily large amount of the organometallic complex was added to a container with ethanol. The only constrain to the proportions was that there remained a significant amount of solid strontium acetylacetonate in the liquid in order to ensure that the ethanol was saturated with the amount of the solid complex that it was capable of dissolving. After shaking the container vigorously, the liquid was filtered through a porous membrane, which eliminated most of the solid residue. Yet, care had to be taken to clean the fuel injector on a regular basis in order to avoid it being clogged by precipitates. This was done by operating it with pure ethanol for about 5 minutes at the end of a day of experiments.

An assessment of the optical thickness in the combustion chamber that results from using this fuel was necessary in order to ensure that the concentration of strontium products was not too high to perform the diagnostics presented, as discussed in Subsection 2.2.4. A simple evaluation can be performed given the physical dimensions of the combustion chamber (Table 3. 1) and estimating the total amount of strontium in the chamber, which can be calculated from the injected fuel mass and the estimated concentration of strontium in the fuel. During the richest runs, a fuel mass of 29.5 mg per cycle was injected, which with the strontium concentration mentioned above introduces 0.89 μg (1.0E-8 mol) of strontium. Dividing this quantity by the volume of the chamber at TDC and multiplying by the bore, the maximum total optical depth of any strontium product during the combustion process is calculated to be 1.4E-5 m^{-2}. This value is lower than the lower limit of the scale in Figure 2. 8, which shows that the medium is well in the optically thin regime for strontium atomic emission. Given that strontium monohydroxide has similar Einstein coefficients as those of atomic strontium [46, 47], this compound can also be assumed to emit under the same optical conditions.

3.1.3 Engine Operation

Several criteria were considered in selecting other engine operation parameters for the experiments. It was necessary for the burnt gas distribution to be as consistently homogeneous as possible because, as will be described in Subsection 3.1.4, radiative emission was collected from a small portion of the chamber volume, and it was therefore necessary for that sampled volume to be representative of conditions in other areas of the chamber where burnt gas was also present. Charge homogeneity also allowed for the 1-D thermodynamic model of the engine to give adequate temperature calculations of the burnt gas region since it uses a two-zone combustion submodel. A description of the thermodynamic model is provided in Section 3.2. Additionally, it was desirable to run the engine in a way that allows for its operation to be modeled with a limited number of parameters that need tuning. This simplifies the calculations and minimizes the uncertainty in the results. For the same reasons, repeatability of results and minimization of cycle-to-cycle variation was sought. Lastly but most importantly, safe and reliable functioning of the engine was required.

Considering these constraints, the operation conditions were selected. The parameters that were constant for all tests are summarized in Table 3. 2. Homogeneous operation was achieved by injecting fuel early during the intake stroke (310 bTDC), which typically provides enough time for the fuel to evaporate and mix well with air before ignition. Opening the swirl control valve made it relatively straightforward to determine the time-resolved mass flow of air into the chamber. This quantity would have been more difficult to characterize otherwise since accurately modeling the constriction of a partially or fully closed valve can be very challenging (in the latter case leaks may be significant). All other parameters in Table 3. 2 were selected from previous baseline runs, which permitted adequate comparisons when troubleshooting was necessary.

Table 3. 2 Constant engine operation parameters for all tests

Engine speed	1300 rpm
Swirl control valve position	Fully open
Injector type	8-hole, 90˚
Fuel injection pressure	12 MPa
Fuel injection timing	310 CAD bTDC
Intake air temperature	45°C
Intake air plenum pressure	40 kPa
Exhaust plenum pressure	101.5 kPa
Oil temperature	45°C
Coolant temperature	45°C

Other parameters were varied in order to form a range of conditions over which radiative emission of strontium products could be characterized. Experiments with different mass of injected fuel per cycle, and therefore different equivalence ratios, ϕ, were performed. This required spark sweep tests in order to find suitable ignition timings for every one of the conditions due to the slowing flame velocity as the equivalence ratio of the charge increases or decreases from stoichiometric operation. It was determined that a spark timing of 28 CAD bTDC for $0.86 \leq \phi \leq 1.42$ and one of 38 CAD bTDC for all other equivalence ratios was adequate, so these timings were used in the experiments accordingly. In addition, runs fueled with pure ethanol were also carried out in order to assess background spectral radiation emitted from the chamber and to assess the effect of strontium products on the combustion process. A summary of the equivalence ratios tested with each fuel and the timing of the optical system, which will be described in detail in the next Subsection, is shown in Table 3. 3.

Table 3. 3 Equivalence ratios and spectral measurement timings tested with the two fuels used.

Ethanol + Strontium Acetylacetonate		Pure Ethanol	
ϕ	Spectral measurement timings (CAD aTDCc)	ϕ	Spectral measurement timings (CAD aTDCc)
1.72	0, 20, 40, 60	1.29	0, 20, 40
1.57	0, 20, 40, 60	1.14	0, 20, 40
1.42	0, 20, 40, 60	1.00	0, 20, 40
1.29	0, 20, 40	0.86	0, 20, 40
1.14	0, 20, 40		
1.00	-10, 0, 15, 20, 40		
0.86	-10, 0, 15, 20, 40		

3.1.4 Imaging System Setup

The setup used to measure the spectral intensity distribution of the visible light emitted from the engine chamber during its operation is depicted in Figure 3. 2. It used an optical collector (Thorlabs, 635 nm SMA Collimation Package), which had a wavelength dependent divergence depicted in Figure 3. 3 and a focal length of 35.41 mm. The collector was placed close to the top of the engine chamber and directed towards the transparent cylinder, as shown in Figure, and was coupled to an optical fiber that directed the radiation to the entrance of a grating spectrometer (Oriel MS127i, Model 77480). The spectrometer used has a Czerny-Turner optical layout with a ruled grating with 400 lines per mm and a blaze wavelength of 350 nm. The light exiting from the spectrometer was focused directly onto the sensor of an intensified camera (LaVision Imager Intense & FlowMaster 3). The intensifier gate width was set at 1 ms (~8 CAD at 1300 rpm engine speed) for all images.

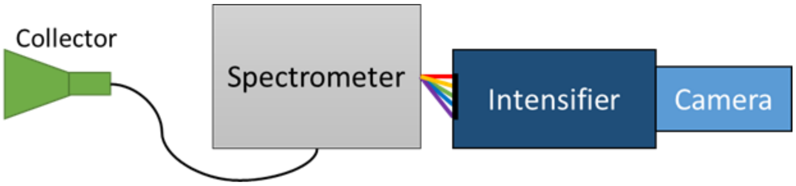

Figure 3. 2 Schematic of optical instrumentation used for in-cylinder spectral measurements.

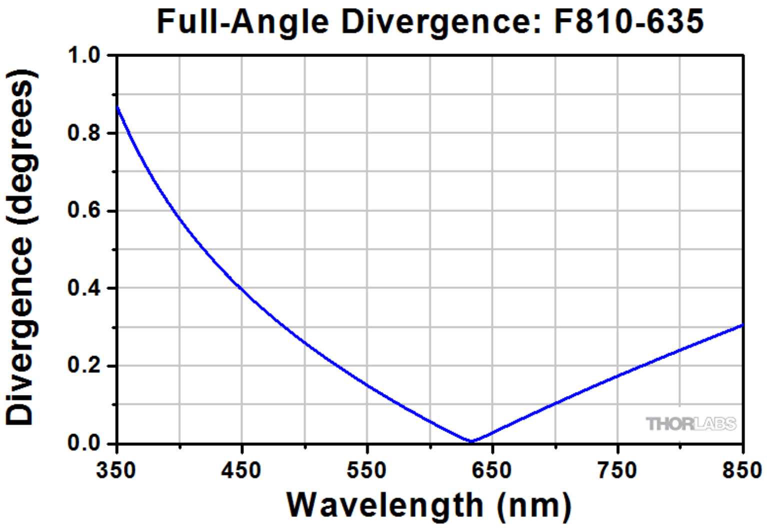

Figure 3. 3 Collimator wavelength dependent divergence as provided by the manufacturer [61].

Figure 3. 4 Combustion chamber of the optical engine. Optical collector was directed towards the area marked with the red circle.

In order for all the spectral features of interest to be measured, it was necessary to position the grating such that the observed wavelengths would range from before the strontium line at 460 nm to after the strontium monohydroxide band centered at 683 nm. In order to do this, the collector was temporarily directed towards a butane flame to which small quantities of strontium nitride were introduced using a stainless steel spatula. As the spectrum of the resulting emission was continuously imaged, the grating was adjusted until the visible features, which were expected to represent those depicted in Figure 2. 1, were within the field of view of the image.

Then, wavelength and relative intensity calibration spectrum images were taken in order to make the necessary post-processing corrections to the in-engine strontium product emission measurements. A mercury lamp (Pen-Ray 90-0012-01), which emits spectral features at well-known wavelengths, was placed in front of the collector, and the spectrum was captured. The location of the mercury features was checked sporadically between some of the engine runs to ensure that no spatial shifting had occurred in the setup. Also, an incandescent tungsten calibration lamp (Ocean Optics DH-2000) was warmed up for 30 minutes, as recommended by the manufacturer for the light bulb to reach steady-state temperature, and the emitted light was coupled through mated fibers directly to the entrance of the spectrometer. Spectral measurements from each of these arrangements were recorded.

After obtaining calibration spectrum images, the engine was operated at the conditions described previously, and the spectral light emission from the engine was measured. The system was synchronized with the engine encoders, and for every one of the engine runs, the camera was triggered once per cycle at predetermined CADs. Table 3. 3 summarizes the different camera timings used for each of the engine conditions.

3.2 In-Cylinder Temperature Calculations

In order to complement the understanding of the spectral emission of strontium monohydroxide in the optical engine, temperature in the cylinder was estimated using a one-dimensional thermodynamic model of the engine setup using the specialized software GT-Power. In essence, the program simulated the operation of the engine and performed a time-resolved first-law analysis of the cylinder. The domain of the simulation is shown in Figure 3. 5. Although the model was meticulously developed to closely simulate the experimental conditions, a tuning process was necessary to obtain the most accurate results possible and estimate the uncertainty of the temperature calculations.

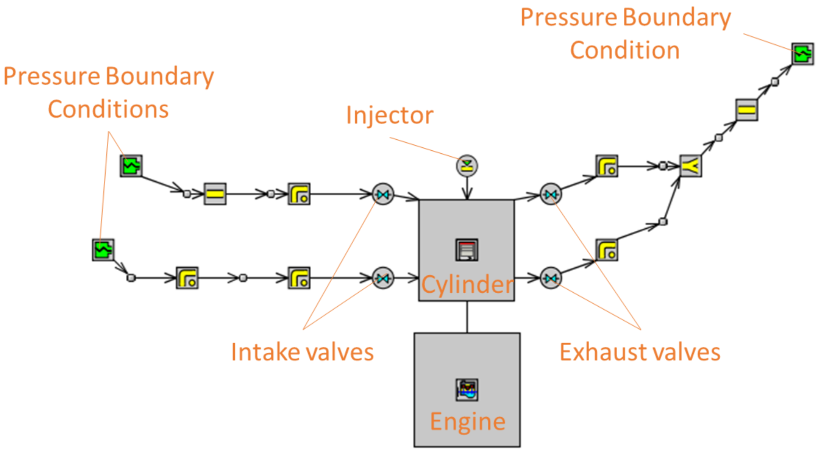

Figure 3. 5 Domain of one-dimensional thermodynamic simulation of the engine.

Experimental pressure measurements were used as inputs in the model to minimize errors in the calculations. The pressure boundary conditions were defined to be the ensemble averages of time-resolved pressure measurements at the intake and exhaust ports. This ensured that the predicted instantaneous gas flow rates through the system was accurate for any given simulated run. Additionally, combustion phasing and heat release rate were determined for each run from the ensemble average of the measured in-cylinder pressure trace.

Despite these efforts, uncertainties in experimental conditions inherently limited the confidence with which temperature could be determined. This is because the instantaneous heat transfer, one of the most influential factors in the calculation of burnt gas temperature, is perhaps also the most difficult aspect to predict accurately. A number of different well-known heat transfer models, which have been empirically developed for particular engine geometries and operating conditions, were available in the software for use in the simulation. The Woschni model without swirl, which was described in Subsection 1.1.3, was selected as the best option for the application, but it was still not expected to be perfectly suitable to the geometry and conditions used in the present study. Additionally, important quantities such as wall temperatures and heat transfer coefficients of oil and coolant during the experiments were not determined and only estimates were used in the model. For these reasons, a strategy to manage uncertainties was needed.

The approach towards this end was to scale the magnitude of the estimated heat transfer using a convective heat transfer coefficient multiplier which was tuned to match experimental results. The multiplier was adjusted so that the calculated pressure trace would qualitatively match the measured ensemble-average cylinder pressure trace of a stoichiometric run. Thus, the error caused by the uncertainties in all the quantities that determine heat transfer were assumed to be corrected by the adjustment of this variable. A comparison of the resulting pressure traces from different values of the multiplier are shown in Figure 3. 6.

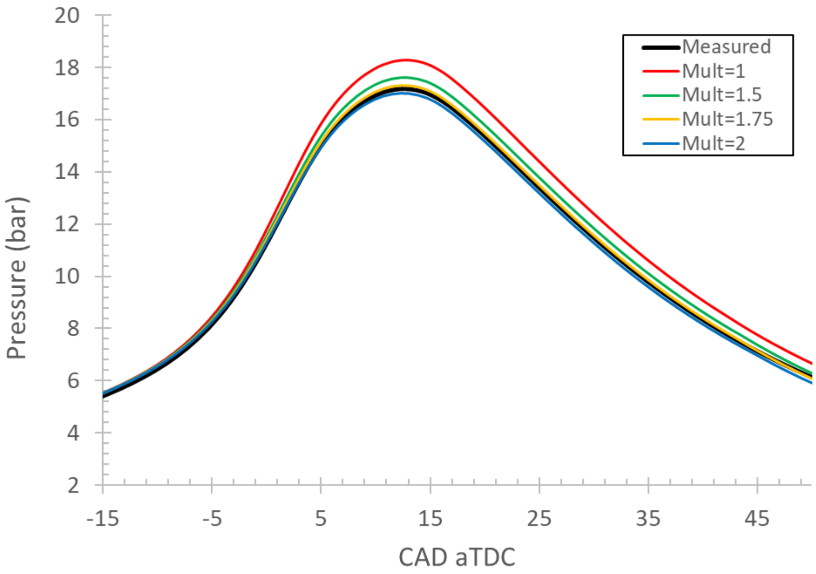

Figure 3. 6 Comparison of calculated pressure traces for different convective heat transfer coefficient multiplier values.

An estimate of the uncertainty of the calculated burnt gas temperature was also necessary in order to understand some of the limitations of the calibration method used. This was obtained by assessing how the variation of uncertain values that are used as inputs in the calculations affects the results. In the case of the convective heat transfer multiplier for the values considered in the figure above, the results vary by about 100 K around top dead center, and the difference decreases later in the cycle, as shown in Figure 3. 7. As a conservative precaution, the uncertainty in the calculated burnt gas temperature was thus determined to be 100 K for all calculations.

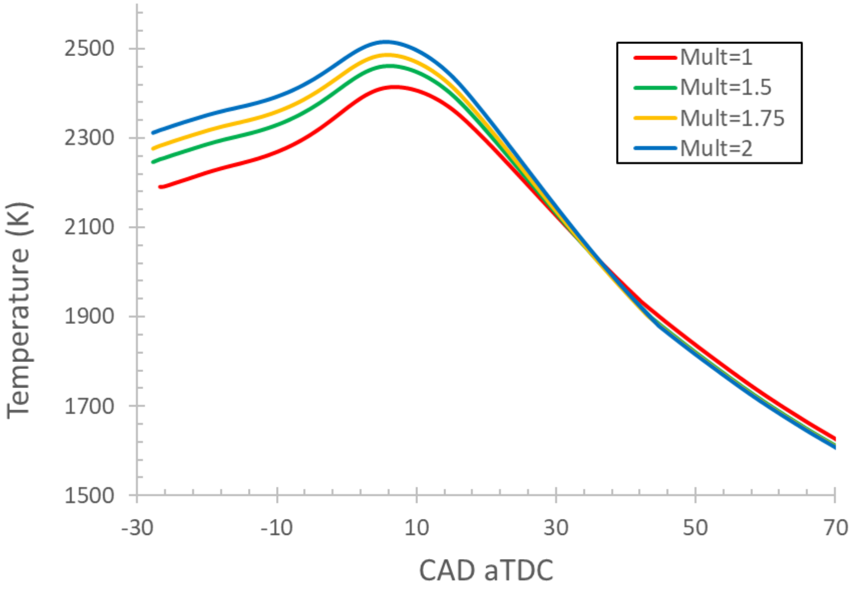

Figure 3. 7 Burnt gas temperature calculated for every value of convective heat transfer multiplier considered.

Once the model was setup and tuned, the experimental engine runs were simulated. The fuel was approximated to be pure ethanol, which neglected the effects of introducing a strontium complex in the fuel. A discussion on the possible resulting errors from this assumption is included in Section 3. For each of the equivalence ratios tested a representative run was selected and simulated by incorporating its ports and cylinder ensemble average pressure traces as previously described. The mass of fuel introduced was adjusted as needed as well as the timing of injection and ignition. The results for some of the burnt gas temperature calculations are shown in Figure 3. 8. As expected, the stoichiometric run results in the hottest burnt gas, and rich and lean charges produce cooler product gases, as excess mass that does not participate in the reaction absorbs some of the energy as sensible heat.

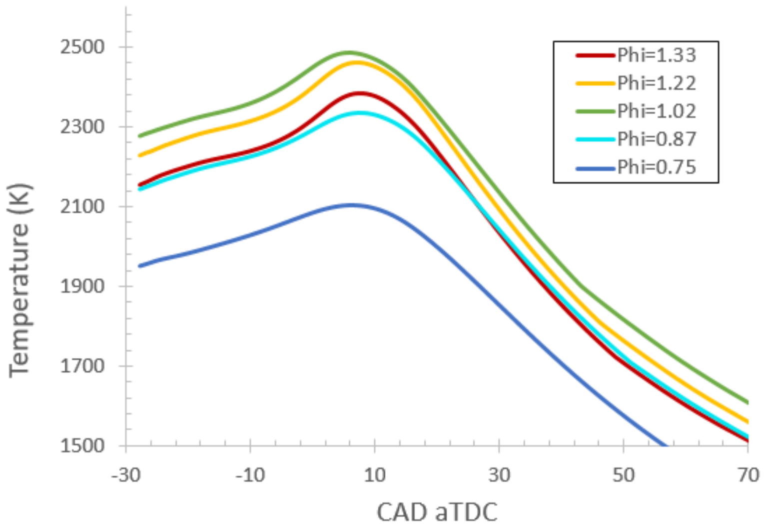

Figure 3. 8 Predicted burnt gas temperature for each of the experimental conditions tested.

The results obtained were then qualitatively examined for accuracy by comparing calculated quantities to measured ones and others reported in literature. Figure 3. 9 shows a comparison of the measured and calculated pressure-volume diagrams in logarithmic scale for some of the conditions tested and simulated. Agreement for all stoichiometric conditions is adequate, and it increases during the compression and power strokes as the charge becomes leaner. For further confirmation of the validity of the results of the simulation, some of the calculated instantaneous heat fluxes, which are shown in Figure 3. 10, were inspected in order to ensure that they were in the same order of magnitude as previously reported for similar conditions. Similar trends have indeed been measured with peak values from about 1000 kW/m^2 to 3000 kW/m^2 depending on the surface of the cylinder with which heat exchange is being considered [62], which is in clear agreement with the obtained results. In the case of the results shown in Figure 3. 10, the heat flux corresponds to a weighted average of all the surfaces involved.

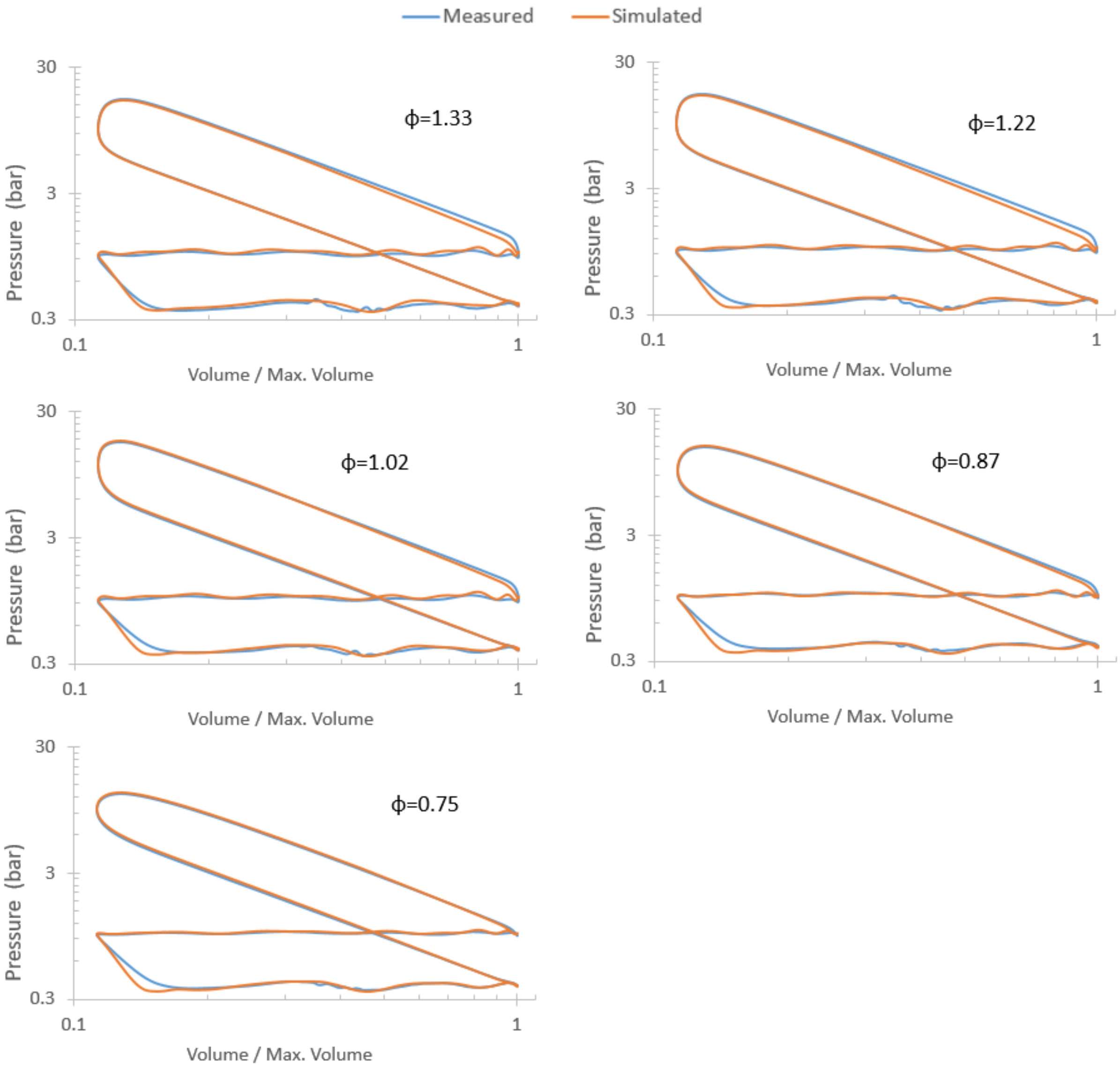

Figure 3. 9 Comparison of experimental and simulated Log P – Log V plots

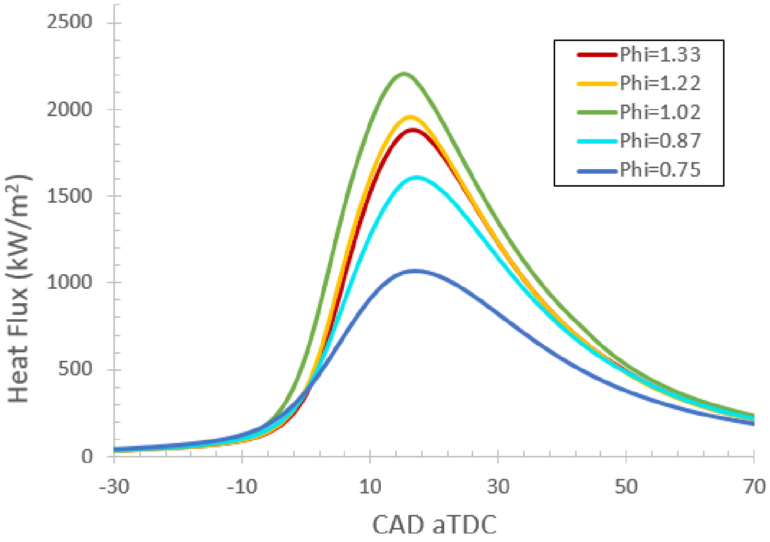

Figure 3. 10 Calculated heat flux for some of the conditions tested.

Once the model was satisfactorily validated, the effect of cyclic variation on the temperature predictions was assessed in order to determine whether assigning the same burnt gas temperature with respect to CAD to all cycles in the run was reasonable. Due to practical limitations in the software, it was not possible to input cycle specific pressure traces to obtain cycle-solved predictions for a given run. However, the calculated burnt gas temperature from pressure data of cycles with the highest and the lowest peak pressures was compared for a few runs. It was found that, at least for cycles whose IMEP (Integrated Mean Effective Pressure) and peak in-cylinder pressure are within 5% of those of the ensemble average, the calculated temperature differences are negligible.

With these analyses it was determined that while inherent significant uncertainties are common in the calculation of in-cylinder temperatures even in the best instrumented research engines, the thermodynamic model used produced useful results for the purpose of investigating the measurement of temperature using the spectral emission of strontium monohydroxide.

3.3 Benchtop Flat Flame Experiments

In addition to the engine experiments, a Hencken burner was used in order to obtain in-flame spectral measurements of strontium and strontium monohydroxide radiative emission at steady-state atmospheric conditions and compare the results with those obtained from engine measurements. These experiments also served to provide preliminary validation results of temperature determination. However, the usefulness of the results was limited by the fact that it was not possible to obtain a significant variation of conditions in the fluorescent region of the flame and that the temperature in it remained unknown due to the complex thermos-fluidic structure in the burnt gases of the flame.

3.3.1 Burner Description

The surface of the burner used in these experiments (Technologies for Research RD1.5X1.5,1.5”) is depicted in Figure 3. 11. It consists of a honeycomb array (35.7 mm × 35.7 mm) of oxidizer tubes (0.95 mm in hydraulic diameter). At the center of each of the array cells, there is a fuel tube with round cross section (0.54 mm ID). This arrangement produces a set of small diffusion flames which, at ambient pressure, are located at about 1 mm from the burner surface [63], and for the purposes of studying combustion products between 2 and 5 cm from the surface, can be regarded as a single premixed flat flame [64]. The flat flame is insulated and shielded from external air by a 7.8 mm thick co-flow of nitrogen that surrounds the area where combustion occurs. The particular model of the burner used in these studies is also equipped with a tube at the center of the surface that ejects a sample fluid, which in this case, was a solution of a strontium compound.

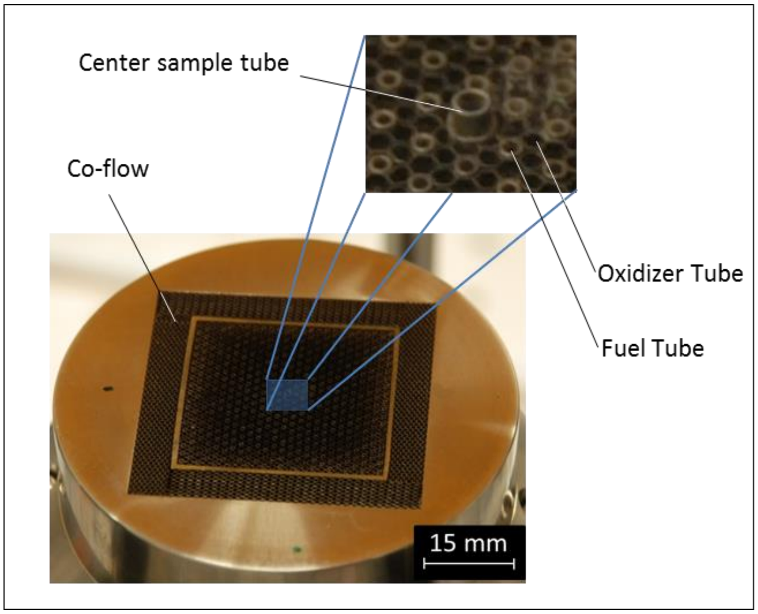

Figure 3. 11 Surface of Hencken burner used in these experiments.

Although the Hencken burner flame has been characterized in numerous studies ([63-66], for example), the flow structure of the burner described here is significantly different from that previously reported in the literature. This is because the fluid ejected from the center tube creates a complex thermo-fluidic structure above the surface. Figure 3. 12 shows a schematic of the burner along with a real-color photograph of the gases above the burner during operation. Due to the cooler flow along a vertical line from the center tube, the conditions in the area where emission from the introduced sample is observed are significantly different from those readily predicted right above a flat flame with no center jet flow. Although this creates significant uncertainty in the conditions at the signal collection area, the temperature of the center jet was still expected to be proportional to the temperature of the product gases outside of the jet, which can be controlled by varying the composition of the flame.

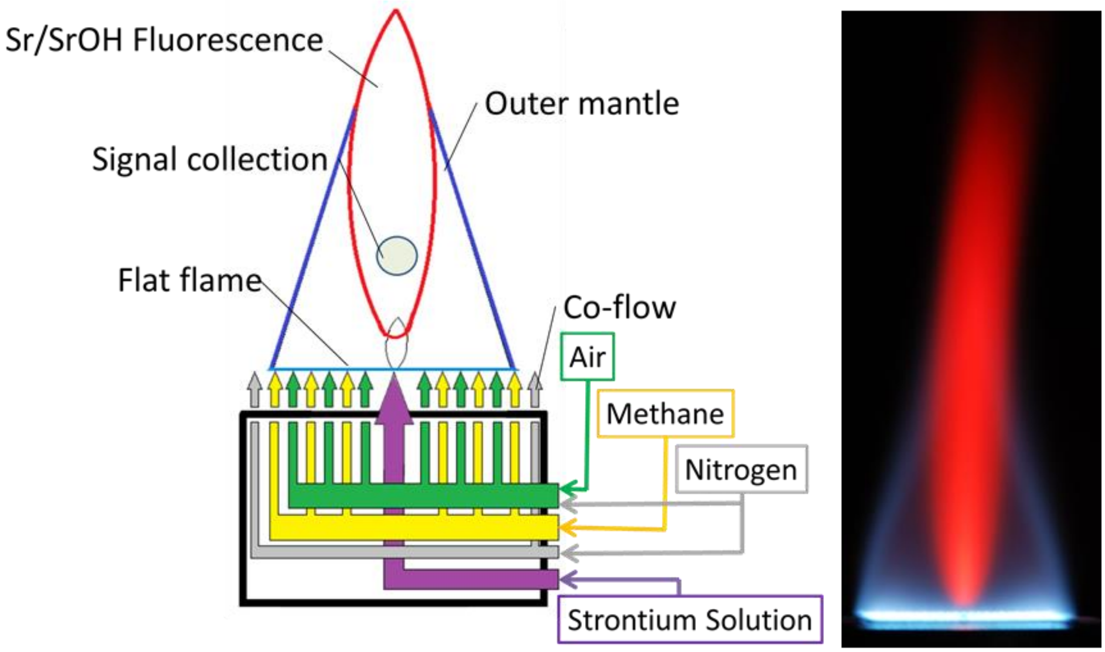

Figure 3. 12 Schematic representation of the Hencken burner and its flow structure (left) and photograph of the flame and product gases (right).

3.3.2 Setup Operation

In an attempt to observe the temperature dependence of strontium monohydroxide emission, the spectral luminosity from the flame was measured while the Hencken burner was operated varying the relative flow of the gases. Air and methane were introduced in the oxidizer and fuel tubes, respectively, and their flow rates were individually controlled with mass flow controllers (Alicat MC-Series).

The conditions in the flame were varied in two ways. First, the total flow rate of the flame gases was fixed at 15.0 SLPM and the equivalence ratio at 1.05 while a suspension of strontium acetylacetonate in water was introduced through the sample tube at 0.5 ml/min. Measurements of the spectrum of the strontium monohydroxide emission at different levels of nitrogen dilution under these conditions were performed with a digital fiber optic spectrometer (Ocean Optics USB2000+) with sub nanometer resolution. About ten measurements were performed at each set of conditions. Note that the resolution of the engine spectral measurements was about 3 nm. In order to compare the results between both types of experiments, the resolution of the burner measurements was artificially decreased by applying a 3 nm moving average filter.

Images of the flame were also captured with the setup shown in Figure 3. 13 while varying equivalence ratio. The total flow rate of the flame gases was maintained at 20.6 SLPM, and the suspension of strontium acetylacetonate in water was introduced through the sample tube at 0.3 ml/min. A beam splitter with uniform 50% transmission and 50% reflection in the visible spectrum was placed close to the flame, and two intensified cameras (LaVision Imager Intense & FlowMaster3) were positioned with respect to the beam splitter in a way such that both of them would image the flame with the same field of view. Each one of the cameras was equipped with a band pass filter (Andover Corp. 610FS10-50 and 680FS10-50) so that each one would capture the radiation from each of the features of strontium monohydroxide. Thus, both of the cameras imaged the combustion gases from the same perspective, but one of them imaged radiation at 605 nm and the other one at 685 nm.

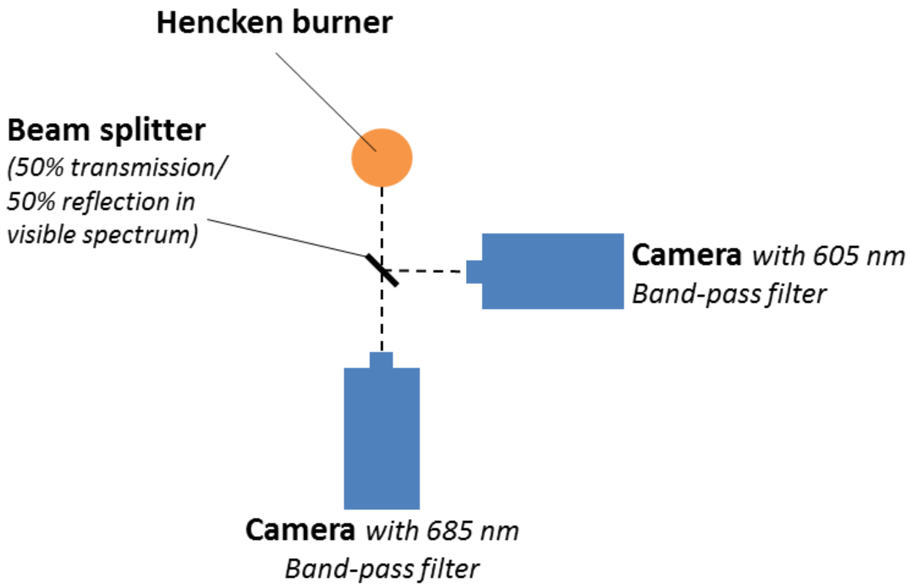

Figure 3. 13 Schematic of the setup of Hencken burner and two cameras.

3.3.3 Results

Figure 3. 14 shows the measured intensity ratios with the adiabatic flame temperature computed from equilibrium calculations overlaid. It can be seen that the intensity ratios calculated from spectral measurements correlates with the adiabatic flame temperature slightly. However, the variation in intensity ratio is small compared to the uncertainty of each of the measurements. Therefore, the possible overall temperature variation in the fluorescent region of the flame is too small to perform assessments of temperature dependent quantities.

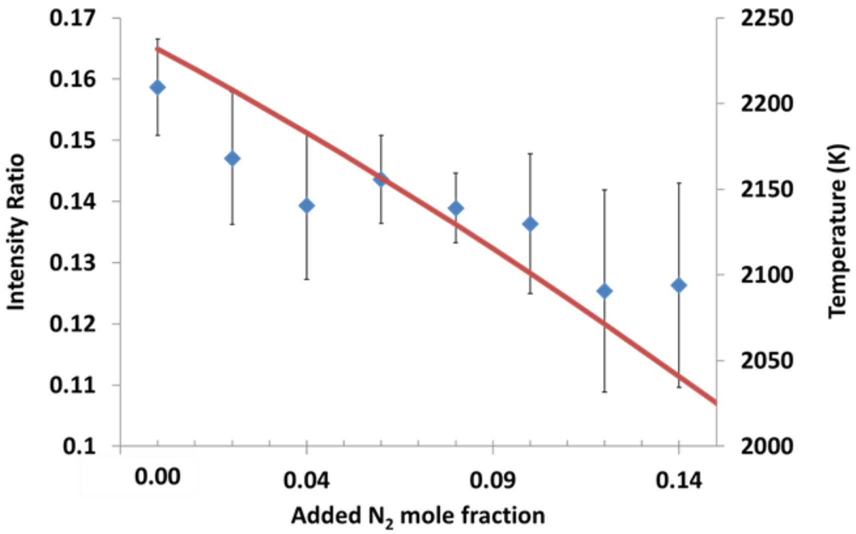

Figure 3. 14 Ratio of the peak intensity of the features at 605 nm and 685 nm with respect to nitrogen dilution in the flame. Error bars are based on the standard deviation of the measurements for a particular set of conditions. The adiabatic flame temperature is overlaid.

Similarly, simultaneous imaging of the flame at two different wavelengths while varying equivalence ratio provided qualitative corroboration of the capability of the diagnostics technique to provide temperature measurements, but a quantitative relationship between temperature and spectral emission was obscured by the fact that the conditions in the flame remained unknown. Figure 3. 15 shows images of the ratios for different equivalence ratios. Differences between images at the different conditions are evident, and spatial differences can be recognized in each of the images, which are perhaps due to inhomogeneities on the burner surface due to contamination.

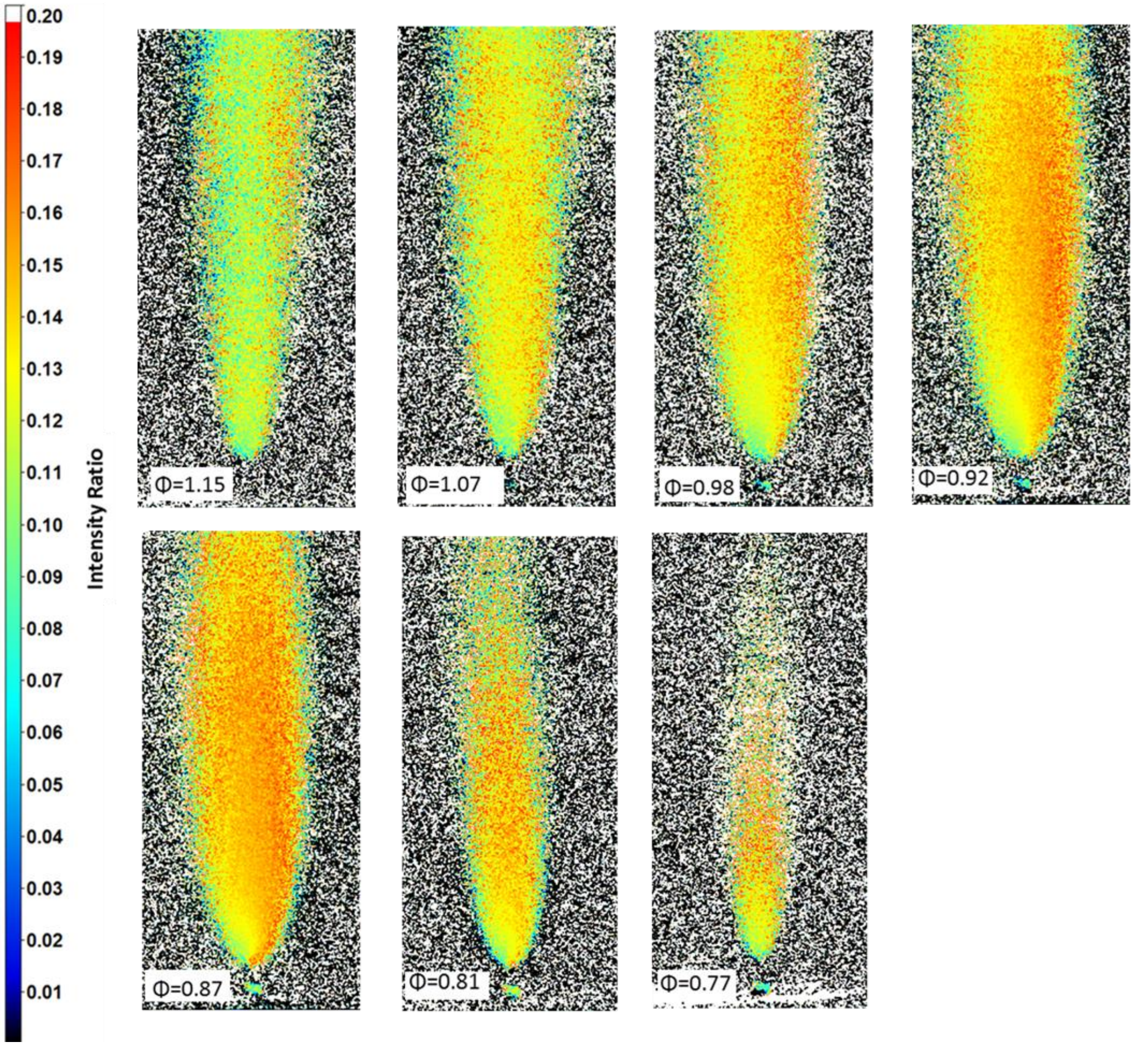

Figure 3. 15 Images of the intensity ratio of the features of strontium monohydroxide used for temperature measurements ($J_{\lambda=605}/J_{\lambda=683}$). A higher intensity ratio correlates with higher temperature.

Chapter 4

Processing and Analysis

Having operated the optical engine with pure ethanol and with a mixture of ethanol and strontium acetylacetonate, combustion performance during runs with both fuels was compared in order to determine whether strontium presence in the chamber affects the processes that the diagnostics technique intends to study. Then, the collected spectral measurements were processed and analyzed in order to establish the relationship between the ratio of intensities of the different spectral features with temperature and equivalence ratio in the gas that produced the emission. The calculation of intensity ratios from spectral measurements required several processing steps such as relative intensity and background subtraction corrections. Subsequently, the relationships were quantified with a linear regression routine. The results showed that the mathematical descriptions discussed in Chapter 2 were adequate, thus confirming the validity of some of the theoretical assumptions made. In addition, insights for the practical application of the diagnostic were obtained. However, due to inherent constraints in the range of conditions investigated and low signal-to-noise ratio in some of the measurements, generally applicable calibration constants were difficult to obtain.

4.1 Assessment of Effects of Strontium Presence in Flame Chemistry

One of the ways in which strontium may affect the processes that the presented diagnostics technique intends to measure is through flame quenching. This is an undesirable effect that could result from the presence of alkaline earth metals in a combustible mixture. It may occur because, if present at high concentrations, the metals can accelerate the rate of recombination of hydrogen atoms [67], thus prematurely depleting the necessary free radicals for flame propagation. In turn, incomplete fuel burn is a consequence of flame quenching, and it can be readily detected because it produces a lower total heat released in each cycle than normal. By comparing the heat released in runs fueled by pure ethanol to that released in runs fueled by the ethanol-strontium acetylacetonate mixture, it can be determined whether the metal has a significant chemical effect on flame chemistry.

This analysis was performed between comparable engine runs in which both fuels were used by following the approach described in Subsection 1.1.2 on every cycle. A least-squares regression of the $\log P - \log V$ plot during the times in which the valves are closed and combustion is not taking place (-125 to -28 CAD aTDCc for compression and 28 to 111 CAD aTDCc for expansion) was done in order to find the ratio of specific heats. Then, Equation (1. 5) was computationally integrated in time with intervals of θ that were the same as the CAD resolution of the pressure transducer used during experiments (0.5 CAD). The values for compression and expansion specific heat ratios were used before and after TDCc respectively, and the integral was performed from -30 to 129 CAD aTDCc. Thus, a total heat released was obtained for every engine cycle.

The results, which are depicted in Figure 4. 1, show no obvious reduction in the total heat released per cycle as a consequence of adding strontium acetylacetonate to ethanol. In fact, the total heat released seems to be slightly higher for runs fuel with the ethanol and strontium acetylacetonate mixture. The difference, however, is not significant given the standard deviation of the runs.

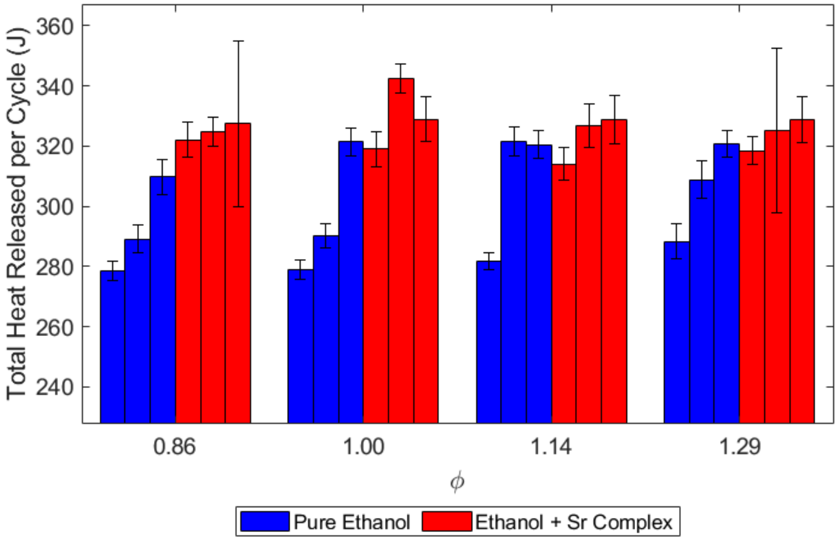

Figure 4. 1 Average total heat released per cycle for a number of runs operated under different equivalence ratios and fuel mixtures. No systematic decrease of heat released is associated with strontium presence.

Besides flame quenching, it is possible to investigate other potential effects of strontium presence on normal flame development, although to the author's knowledge none have been reported. For the purpose of investigating additional effects, the CAD of 5% and 95% Mass Burned Fraction (MFB) were compared for runs that were fueled with and without strontium, as shown in Figure 4. 2 and Figure 4. 3. It is clear that there is no difference in combustion development for the different fuels given the cycle-to-cycle and run-to-run variability of the quantities considered. Consideration of the heat release rate further confirms this observation. Figure 4. 4 shows this quantity as a function of CAD for the stoichiometric runs. It can be seen that the differences between the curves corresponding to different fuel mixtures are no larger than the run-to-run variations for a given fuel. Therefore, it was determined that within the precision limits of the operation and performance assessment of the engine, the effect of strontium on the combustion process is negligible under the conditions considered.

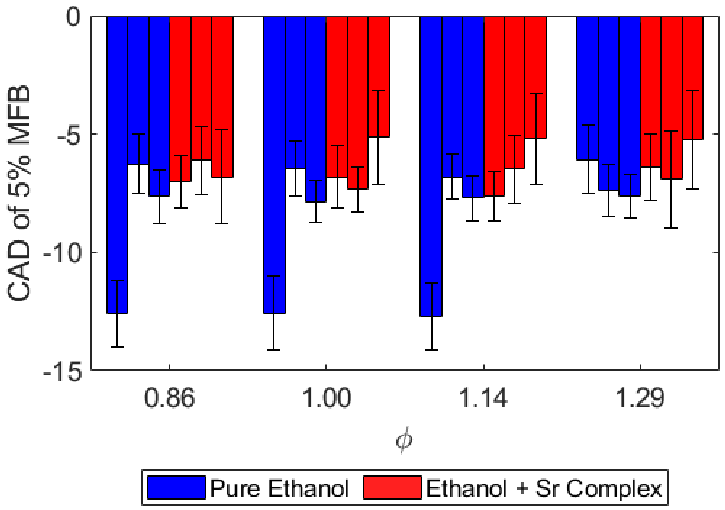

Figure 4. 2 Comparison of 5% MFB for engine runs fueled with pure ethanol and ethanol + strontium acetylacetonate mixture under different equivalence ratios.

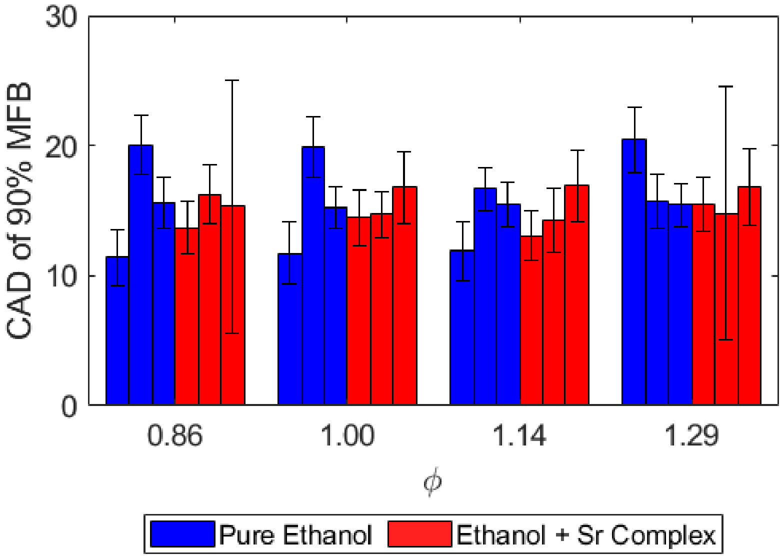

Figure 4. 3 Comparison of 95% MFB for engine runs fueled with pure ethanol and ethanol + strontium acetylacetonate mixture under different equivalence ratios.

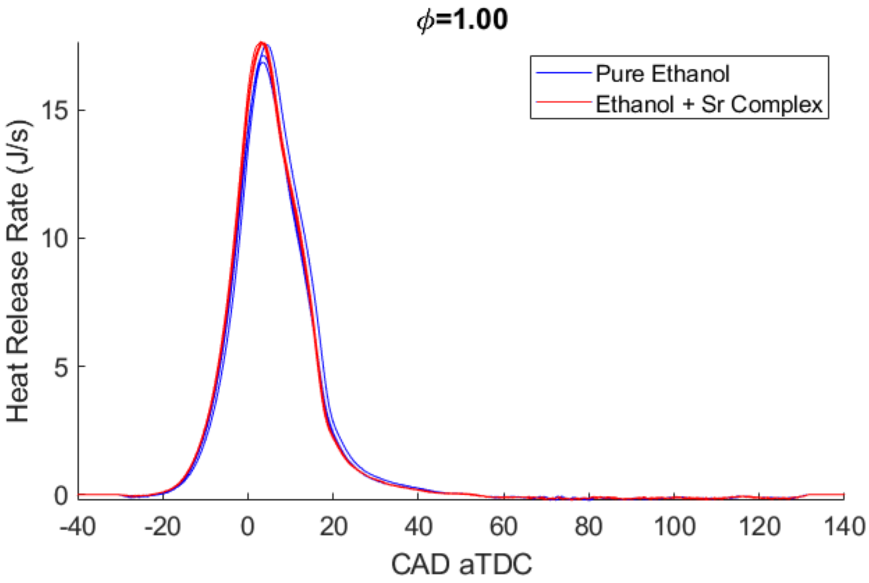

Figure 4. 4 Ensemble average of heat release rate for runs fueled with ethanol with and without strontium acetylacetonate under stoichiometric conditions.

4.2 Calculation of Intensity Ratios from Engine Spectral Measurements

Images of the exit of the spectrometer collected during calibration measurements and engine experiments were inspected and processed for quantitative analysis. Images that had more than 10 pixels with a saturated number of counts were discarded from further processing. The intensity along every column of pixels in the remaining images was then added to obtain a plot of intensity vs. wavelength. An example of this procedure is shown in Figure 4. 5.

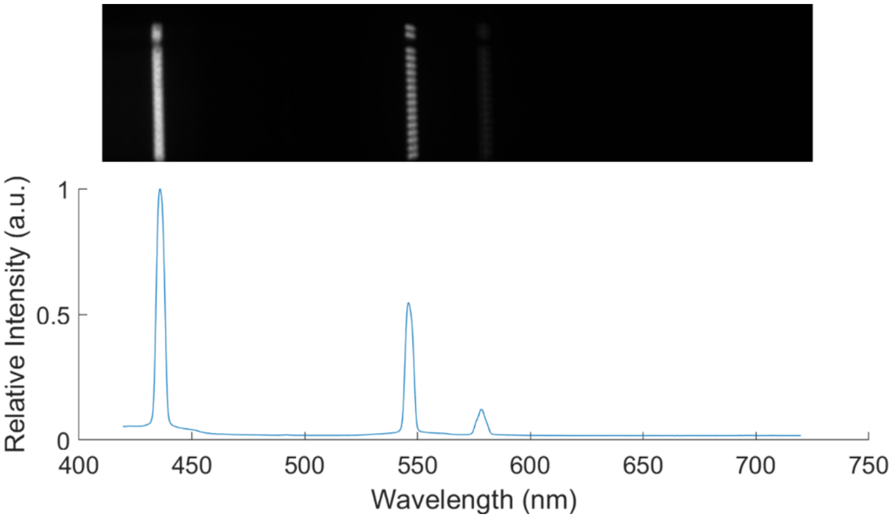

Figure 4. 5 Mercury lamp spectrum. Example of a spectrum image and its resulting plot.

Then, wavelength calibration was applied to the relative intensity calibration and engine measurement plots. Estimating the wavelength range that was encompassed by the field of view of the camera after coarsely positioning the grating and noting the known locations of mercury features, the lines observed in the calibration spectrum images were determined to be located at 435.8 nm, 546.1 nm, and 579.0 nm. The pixel locations of the peaks of the lines at 435.8 nm and 579 nm were used to linearly relate each pixel's horizontal location to a wavelength. The position of the remaining line was then corroborated to be at 546.1 nm in the resulting scale. The three peaks are readily observable in the plot of the bottom half of Figure 4. 5 corresponding to the two clearly visible lines in the image. The line corresponding to the third peak is barely noticeable in the image. It is worth noting that from this plot the spectral resolution of the system may be determined. This was established by the Full Width at Half Maximum (FWHM) of the mercury emission lines as they appear in the plot, which was approximately 3 nm.

Relative spectral intensity calibrations were also necessary in order to account for the spectral sensitivity of the setup. The intensity plots from the relative intensity calibration images were compared to the spectral distribution of the calibration lamp, which according to the manufacturer, was approximately that of a black body at 2960 K. From this comparison, wavelength-dependent intensity correction factors were calculated and applied to all engine spectral measurements. This permitted the determination of their true relative spectral intensity.

After calibrating the engine spectral measurements for wavelength and relative intensity, the background radiation intensity was determined and subtracted. The background radiation is emitted from substances in the burnt gases other than strontium and strontium monohydroxide, and it often overlaps in wavelength with the features studied. An examination of interfering radiative emission was performed by comparing the spectral measurements of pure ethanol runs with the ones from runs fueled with the strontium acetylacetonate-ethanol blend. The spectral emission measured during pure ethanol tests was expected to be representative of that obtained from other sources besides strontium products during experiments in which strontium was added to the fuel.

All spectral measurements obtained from pure ethanol-fueled tests showed sodium emission at 589 nm and broadband emission similar to that of a black body. An example is shown in Figure 4. 6.

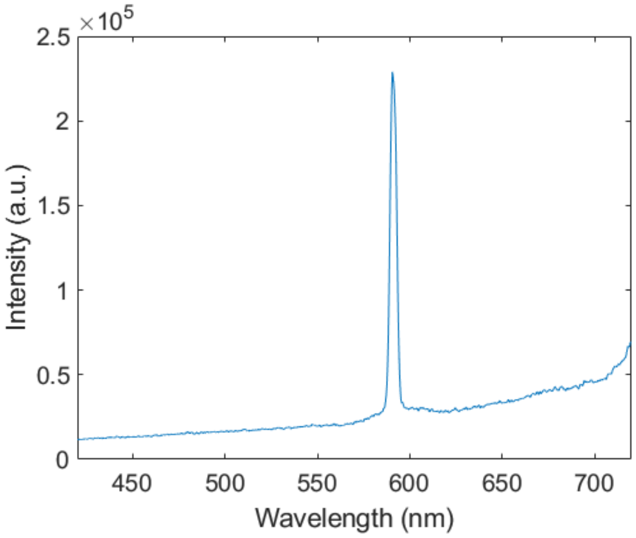

Figure 4. 6 Example of radiation spectrum collected from optical engine combustion chamber during tests fueled by pure ethanol.

The sodium feature is explained by the fact that this element is generally present in relatively large quantities in laboratory-grade ethanol such as the kind used to fuel the engine in these experiments and perhaps also in the seed oil used for lubrication of the piston. However, this is largely of no concern for the measurements pertinent to this work since sodium emission in the visible spectrum is spectrally well separated from any of the strontium product features under study, and therefore, no correction for it was necessary.

The wide-ranging broadband emission, on the other hand, does overlap in wavelength with strontium and strontium monohydroxide radiative emission. It likely originates from solid particles of silicon dioxide formed as a combustion product of seed oil. Attempts were made to minimize the formation of this substance by decreasing the amount of seed oil supplied to the chamber, but since the seed oil is introduced upstream from the intake plenum, significant amounts of oil had likely been accumulating on the inside walls of the intake system over the long term operation of the engine. For this reason, even if little or no seed oil was added in the experiments ran for this study, some oil was still advected into the engine from the walls of the intake system, which resulted in broadband emission of unpredictable intensity detected in the measurements described in this work. This would also explain the fact that no correlation was found between any common engine performance metrics and the spectral intensity of background emission.

In light of these observations, a strategy was devised to quantify the emission from silicon dioxide that interferes with that from strontium and strontium monohydroxide. The method is based on predicting the background radiation intensity in interfering ranges from the intensities in non-interfering ranges for each collected measurement. The approaches used in the in the atomic strontium range (455 nm – 465 nm) and the strontium monohydroxide ranges (600 nm – 610 nm and 635 nm – 705 nm) were slightly different.

In the case of the atomic strontium range, the background was approximated by fitting an exponential function to the measured spectral intensity at wavelengths in the vicinity of 460 nm. Figure 4. 7 shows measured spectral distributions of emission collected during tests with and without strontium acetylacetonate. The data points in the wavelength ranges 430 nm – 455 nm and 465 nm – 490 nm were fitted to a function of the form ae^{bx}. It can be observed in the image on the left that the resulting function matches the measured background radiation intensity in the range 455 nm – 465 nm reasonably well. Thus in this case, the spectral data collected from pure ethanol tests was used only to corroborate qualitatively that the resulting fitted function describes the background radiation in the 455 nm – 465 nm range accurately.

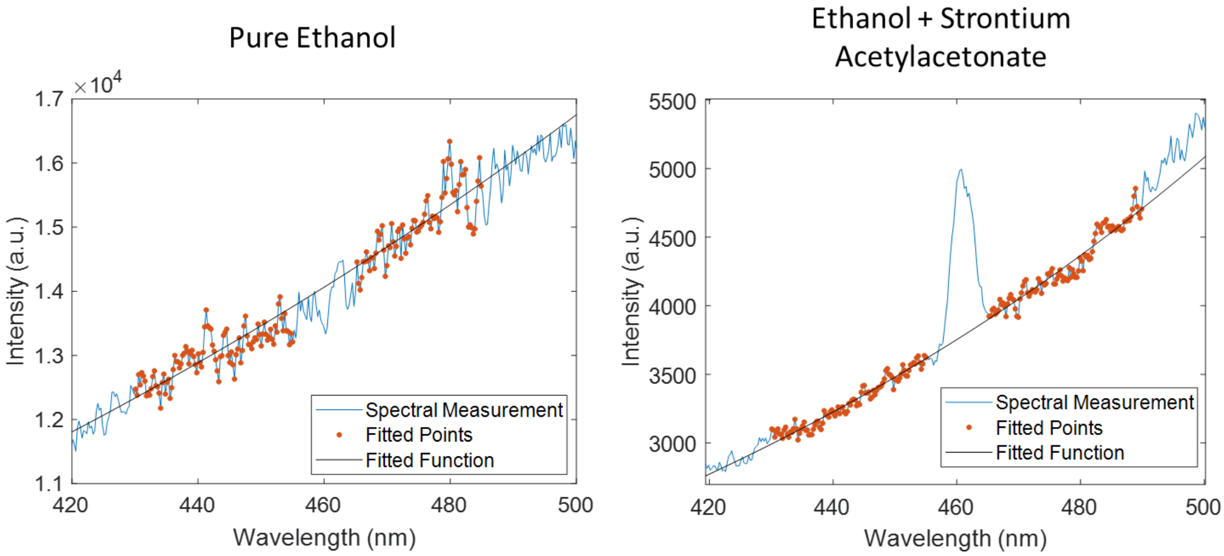

Figure 4. 7 Measured spectral distribution and the fitted points and function used to approximate the spectral intensity of background radiation in the atomic strontium emission range. Measurements for an engine cycle of a test fueled with pure ethanol (left) and the strontium acetylacetonate-ethanol mixture (right) are shown. The intensities are different in both plots due to cyclic variabilities.

On the other hand, for the strontium monohydroxide emission range, the data from pure ethanol tests was used to create interpolation tables to predict the background spectral intensity. This is because strontium monohydroxide emission ranges are larger, and the background intensity at a sufficient amount of neighbouring points for an adequate direct function fitting was either obscured by the sodium feature or was not measured due to insufficient range of the instrumentation used. The independent variable in the interpolation tables was the intensity at 625 nm, a point at which no emission besides background is expected in neither pure ethanol nor ethanol-strontium acetylacetonate tests. The dependent variables were the intensities at 8 equally spaced locations in the range 635 nm – 705 nm. The intensity at 625 nm was determined for each of the measurements performed in ethanol + strontium acetylacetonate tests and the background intensities at the locations in the range 635 nm – 705 nm in the same tests was estimated from the pure ethanol interpolation tables. Then, a function of the form $ae^{bx} + ce^{dx}$ was fitted on those points and on the measured intensity at 540 nm, 625 nm, and 715 nm. Figure 4. 8 shows examples of measured spectral distribution of radiation emitted from the engine combustion chamber and the results of the function fitting process. A visual comparison between measured and projected background spectral intensity was performed on several of the measurements on pure ethanol tests, and adequate results were confirmed in all of them.

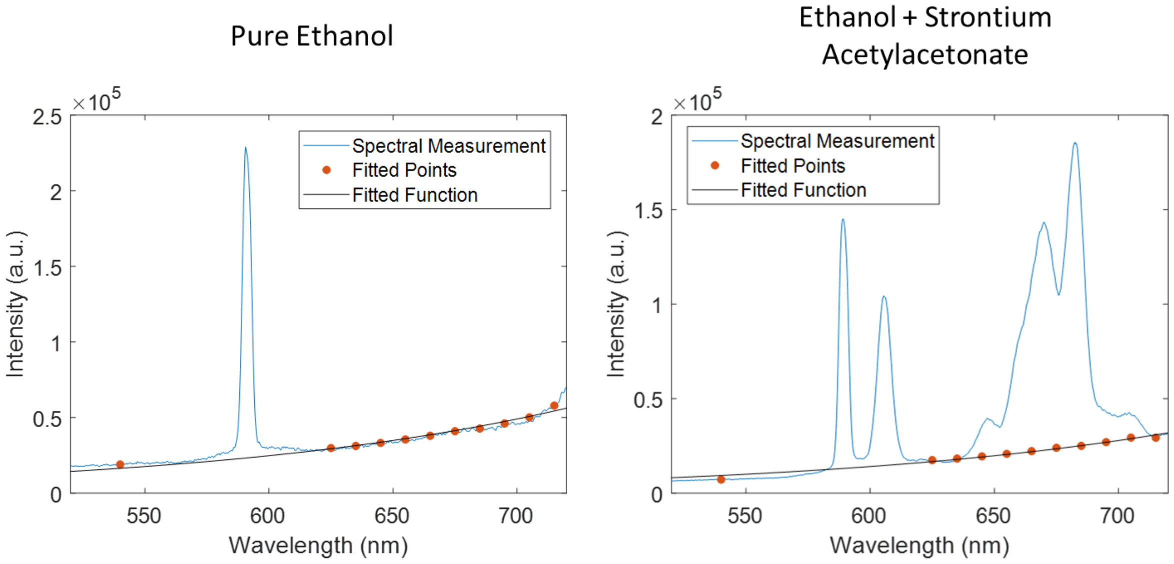

Figure 4. 8 Example of measured spectral distribution and the fitted points and function used to approximate the spectral intensity of background radiation in tests fueled with pure ethanol (left) and the strontium acetylacetonate-ethanol mixture (right).

Although this background subtraction methods were expected to be generally effective at separating the useful signals from the interfering ones, the uncertainty of the corrected spectral intensity was expected to increase with increasing background emission intensity relative to strontium and strontium monohydroxide emission. This is because of the inherent associated decrease in signal-to-noise ratio of the data. In addition, it is likely that other strontium products besides atomic strontium and strontium monohydroxide, such as strontium oxide, also emit background radiation to an extent that is not possible to determine with available methods. In order to obtain a metric of the uncertainty of the true spectral intensity associated with this effect, background indexes, B_{SrOH} and B_{Sr}, were calculated for each spectral measurement. These were defined to be the integrated spectral background in the wavelength range of the signal with which it interferes, $J_{\text{bkg,SrOH}}$ or $J_{\text{bkg,Sr}}$, divided by the square of the intensity of the integrated corrected signal, J_{Sr} or J_{SrOH}, as expressed in Equations (4. 1) and (4. 2). Figure 4. 9 shows an example of the areas used for this calculation for strontium monohydroxide.

$$B_{\text{SrOH}} = \frac{J_{\text{bkg,SrOH}}}{{J_{\text{SrOH}}}^2} \tag{4. 1}$$

$$B_{\text{Sr}} = \frac{J_{\text{bkg,Sr}}}{{J_{\text{Sr}}}^2} \tag{4. 2}$$

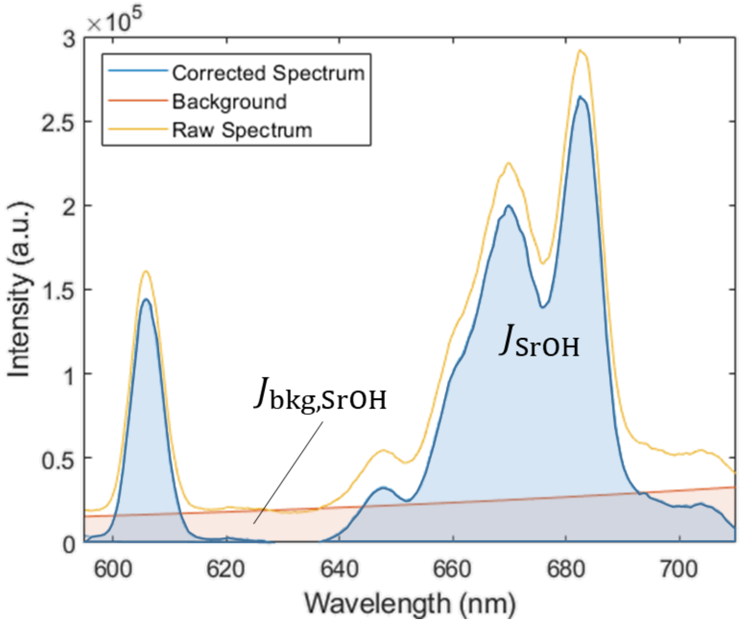

Figure 4. 9 Representative schematic of the areas used to calculate the background index of strontium monohydroxide for each spectral measurement. The area of the region shaded in orange was divided by the square of the area of the region shaded in blue.

After subtracting the background from each of the spectral measurements and characterizing their signal-to-noise ratio, spectral intensity ratio calculations among the bands of strontium monohydroxide were performed. Different intensities for each band were first determined by their peak intensity[3], and by integrating the total intensity of a portion of it defined by four hypothetical ideal step detection bands and a Gaussian filter. The step bands had widths of 1.1 nm, 3 nm, 6 nm, and 10 nm, and the Gaussian filter had a FWHM of 10 nm. Note, however, that the resolution of the spectrogram was determined to be 3 nm, as mentioned in Chapter 3. In this way, each spectral band in a given measurement was assigned a total of 6 intensities associated with it. The detection bands were centered at the same locations as the peaks for each of the bands; 606 nm for the $B^2\Sigma^+ \rightarrow X^2\Sigma^+$ transition, and 670 nm and 683 nm for the $A^2\Pi \rightarrow X^2\Sigma^+$ transitions. An example of the calculation of the integrated band intensities is shown schematically in Figure 4. 10. Then, intensity ratios $J_{\lambda=605\text{ nm}}/J_{\lambda=683\text{ nm}}$, $J_{\lambda=605\text{ nm}}/J_{\lambda=670\text{ nm}}$, and $J_{\lambda=670\text{ nm}}/J_{\lambda=683\text{ nm}}$ were calculated for each detection bandwidth. Thus, 18 different intensity ratios among strontium monohydroxide bands were calculated for each spectral measurement.

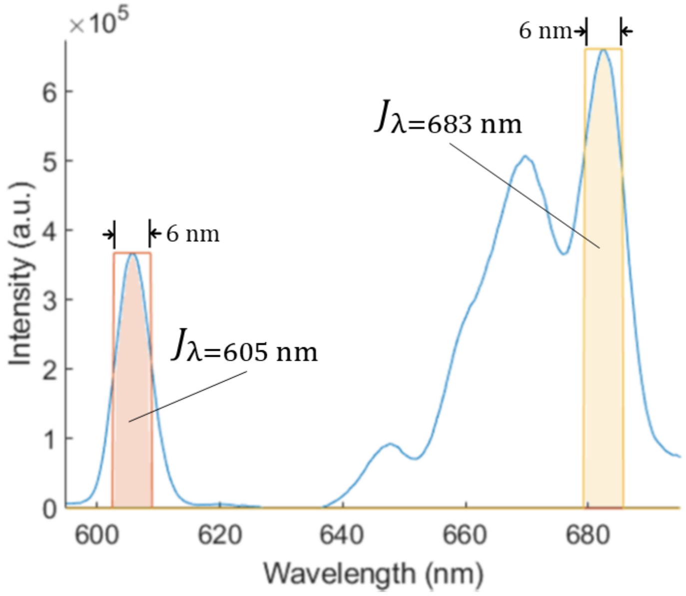

Figure 4. 10 Schematic of the calculation of the integrated intensities of the bands at 605 nm and 683 nm using ideal step band-pass filters of 6 nm width. The intensity assigned to each of the bands is defined by the area of the shaded regions.

---

[3] Quantities related to the intensity ratios determined in this way are associated with the label *"0nm"* in the present document.

The location of the detection bands was determined to be optimal for high intensity measurements under all conditions tested in the experiments. Although molecular spectral features generally change shape, and consequently their peak intensity often shifts with changing gas conditions, the strontium monohydroxide bands were found to preserve their overall shape and location under all temperatures and pressures applied in the study. Figure 4. 11, which depicts a comparison of the average relative spectral emission intensity for three different engine runs, shows that this was the case. Relatively constant shape and location of the strontium monohydroxide bands at flame conditions was also confirmed previously by other authors [51, 68]. This observation constitutes an attractive feature of the presented diagnostic since it indicates that a constant detection band provides the highest possible signal independent of conditions, which is of great benefit to obtain the largest amount of signal possible in imaging studies.

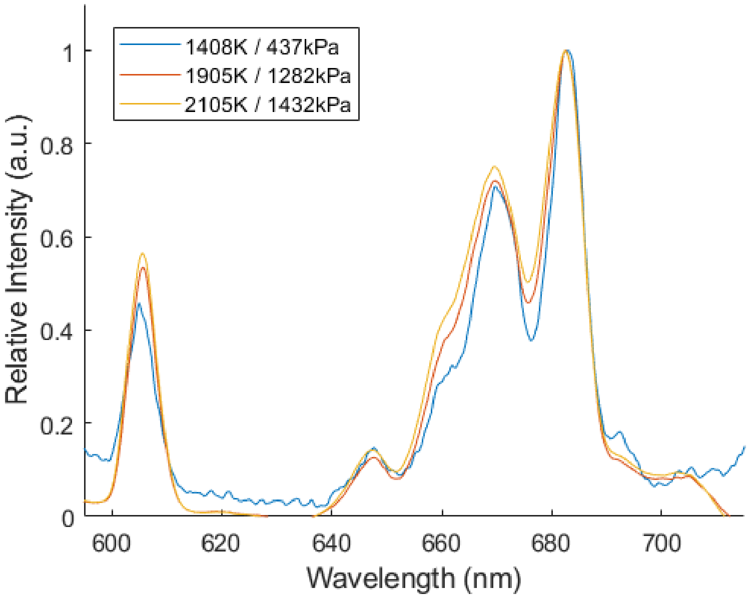

Figure 4. 11 Average relative intensity of strontium monohydroxide features for three different runs. Predicted temperature and average pressure during the spectral measurements are indicated.

Intensity ratios between the strontium atomic line and the strontium monohydroxide band were calculated in a similar way. The same detection locations and bandwidths were used to calculate the intensity of the strontium monohydroxide features, but the intensity of the strontium feature was always established by an ideal step band-pass filter 10 nm wide centered at 460 nm.

This was done because the intensity of the strontium line was generally too low to obtain meaningful quantities with thinner detection windows.

Finally, once intensity ratios had been calculated, measurements from engine cycles that exhibited significant differences in engine performance metrics with respect to the average of the run were eliminated from further analysis. This was necessary to ensure that spectral measurements from cycles that might not be properly represented by the ensemble average pressure traces, which were the ones used to make the temperature predictions, would be considered. Otherwise, measurements from cycles in which the combustion process occurred in a particularly distinct way would distort the results. This was a particularly substantial problem in excessively lean or excessively rich runs. The issue was mitigated by eliminating runs that had a peak pressure 5% or more different from the average or an IMEP 2% or more different than the average.

4.3 Error and Uncertainty Considerations

Before interpreting the experimental results, careful consideration of the limitations of the methods used is needed. These arose mainly from constraints imposed by the engine system and the limited dynamic range of the optical equipment utilized.

Since in the current approach the probed gas volume was the cylinder of an IC engine, the range of conditions in it could not be directly and independently controlled, but instead they were created by varying a set of inputs into the operation of the optical engine. The inputs influenced the chemical and thermodynamic conditions in the cylinder (independent variables) which ultimately dictated the measured emitted spectral intensity (dependent variables). Limitations stemmed in great part from the inherent uncertainty in the resulting conditions in the engine cylinder. As shown in Figure 4. 12, in the idealized conceptualization of the relationship between conditions and measurements, a particular set of inputs deterministically dictate the conditions in the cylinder, which can be established through the computational thermodynamic calculations performed on GT-Power. In reality, however, the results of these calculations are only statistical representations of the actual conditions in the cylinder, which during any one cycle and spectral measurement are highly chaotic and uncertain.

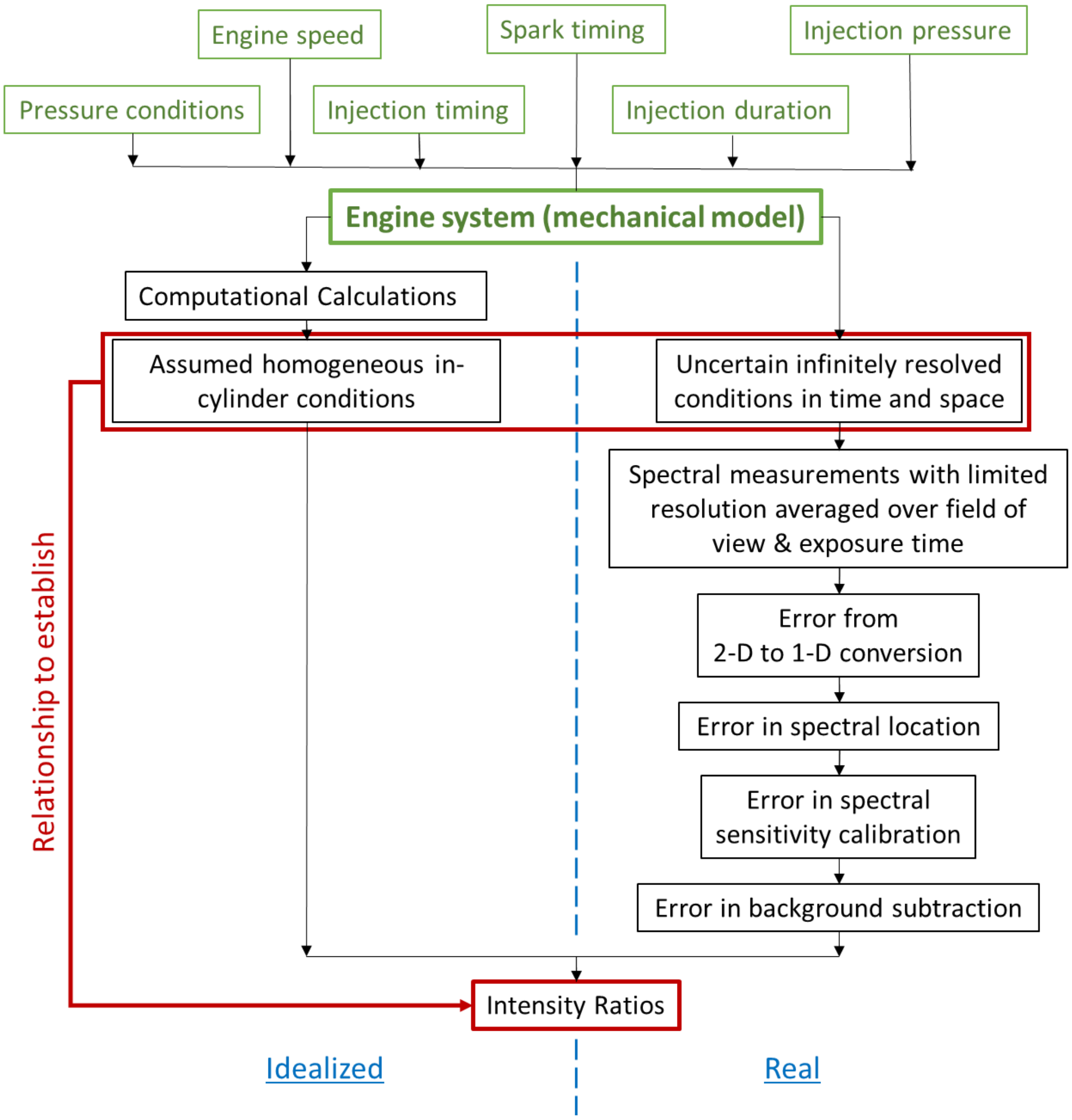

Figure 4. 12 Flow diagram of the real and idealized ways in which the controllable inputs (green boxes) ultimately determine the spectral intensity ratios measured. Error propagation in the "Real" section is considered qualitatively in this work.

Besides the inherent ambiguity associated with the exact conditions in the cylinder at any point in time, the measurements themselves and the sequential processing steps introduced uncertainty in the results as well, as shown in Figure 4. 12. The measurements were limited spatially by the volume enveloped by the collector in the experimental setup. In addition, the 1 ms exposure time necessary to obtain measurements with sufficient signal-to-noise ratio averaged the spectral emission over a relatively long period of time (~8 CAD). Then, converting the images to 1-D intensity plots, locating the features in the spectrum, correcting the relative spectral intensity, and eliminating the background emission introduced additional error, some of which is very difficult to characterize. However, the uncertainty in the conditions in the cylinder likely made a significantly larger contribution to the overall uncertainty in the relationship between gas conditions and emission spectral intensity.

An inherent feature of this methodology was that many of the uncertainties were collectively exacerbated and difficult to separate with decreasing gas temperature. As seen on Equation (2. 36), the absolute spectral intensity of emission decreases exponentially with decreasing temperature. In addition, number density of emitting species, which proportionally affects emission intensity, is also generally lower at low temperatures. This is because low temperatures in an engine cylinder are inherently associated with low pressure and high volume conditions which in turn are associated with low gas density. Thus, with decreasing temperature the signal-to-noise ratio of the spectral measurements decreased on account of two different but associated factors. The increased noise in measurements at low temperatures can be appreciated in Figure 4. 11. In an attempt to mitigate this problem, very high equivalence ratio tests were performed in order to increase the number density of the emitting species. However, since temperature has a larger effect on emission intensity, the improvement was relatively small. On the other hand, operating the engine at these extreme conditions created significant combustion stability issues, which resulted in high cycle-to-cycle variation, and therefore higher uncertainty in the conditions of any one cycle with respect to the ensemble average resulted. Furthermore, since low temperatures are generally obtained later in the cycle (40-60 CAD aTDC), they are also associated with larger deviations from the computational predictions. This is because the 1-D thermodynamic model uses a two-zone combustion model in the chamber, and as time elapses from the moment of ignition, this assumption becomes increasingly dubious as the hypothetical zones interact with turbulent structures and with surfaces with which heat transfer is uncertain. For these reasons, obtaining a sufficiently large range of experimental conditions to attain a general characterization with modest errors was extremely difficult.

Figure 4. 13 illustrates the consequences of this problem. It shows histograms for measured intensity ratio of strontium monohydroxide features for different engine runs. The computational thermodynamic model predicts the temperature at the time the spectral measurements were made to be the same for all cycles in each run. However, the distribution of

measured intensity ratios, which are only dependent on temperature, shows that there is considerable variability for two of the runs. Since cycles whose in-cylinder pressure traces were significantly different from the ensemble average were already eliminated, this fluctuation can only be explained by in-cylinder processes that are not accounted for in the model.

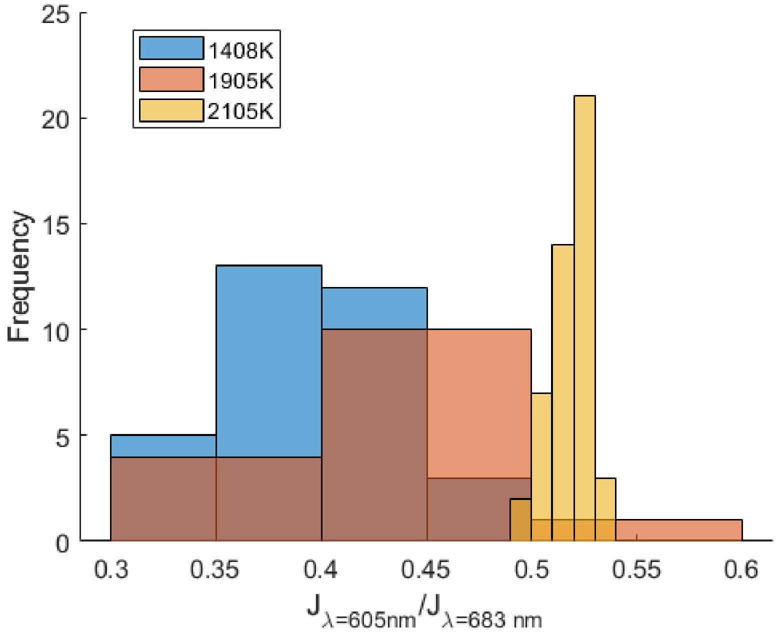

Figure 4. 13 Distribution of the ratios of the intensities of the indicated strontium monohydroxide bands determined with 6 nm detection bands for three different engine runs.

In addition, the difference in intensity between atomic strontium and strontium monohydroxide emission posed significant problems as well. As observed in Figure 2. 1, strontium emission is very low both in absolute terms and compared to that of strontium monohydroxide. This was the case in all experimental measurements obtained. Under some conditions it was possible to obtain high count measurements, but not high enough for strontium emission to have a low signal-to-noise ratio before the strontium monohydroxide features were saturated in the optical detector. Thus, assuming that the medium remains optically thin, the benefit brought about by efforts to arbitrarily increase the intensity of measured emission by any means is only as large as the dynamic range of the optical equipment used. In this study a 12-bit camera, which collects a maximum of 4095 counts per measurement, was used. Since this problem had been anticipated in an early phase of the project, the use of a 16-bit camera

(LaVision Imager sCMOS) was considered. However, this camera was found to be inadequate for the purposes of this study due it being inherently designed for use with external irradiation sources.

4.4 Temperature Relationship

4.4.1 Linear Regression Calculations

Having processed the measurements to calculate the intensity ratios of strontium and strontium monohydroxide emission spectral features and having assessed the experimental uncertainty, quantification of the relationship between intensity ratios and temperature was pursued. As stated in Subsection 2.3.1, a linear fit of data from measurements of intensity ratios at different temperatures is needed in order to accomplish this. Figure 4. 14 shows experimental results in a form in which a line that satisfies Equation (2. 40) could be fitted. The y-axis quantities were calculated from the average of the computed intensity ratios for a given run, and their error bars were determined from their standard deviation. The x-axis values were obtained from the temperatures calculated from the GT-Power model averaged over the 8 CAD interval in which the optical detector collected spectral measurements for each run, and its error was defined from the established error of the in-cylinder calculations. It can be readily seen that the errors in both axes are significant for all intensity ratios and detection bandwidths considered, which introduces difficulties in calculating the line fitting parameters. This is because a standard linear regression takes into account the uncertainty in the dependent variable, but not in the independent one [69], and therefore an alternative procedure is needed.

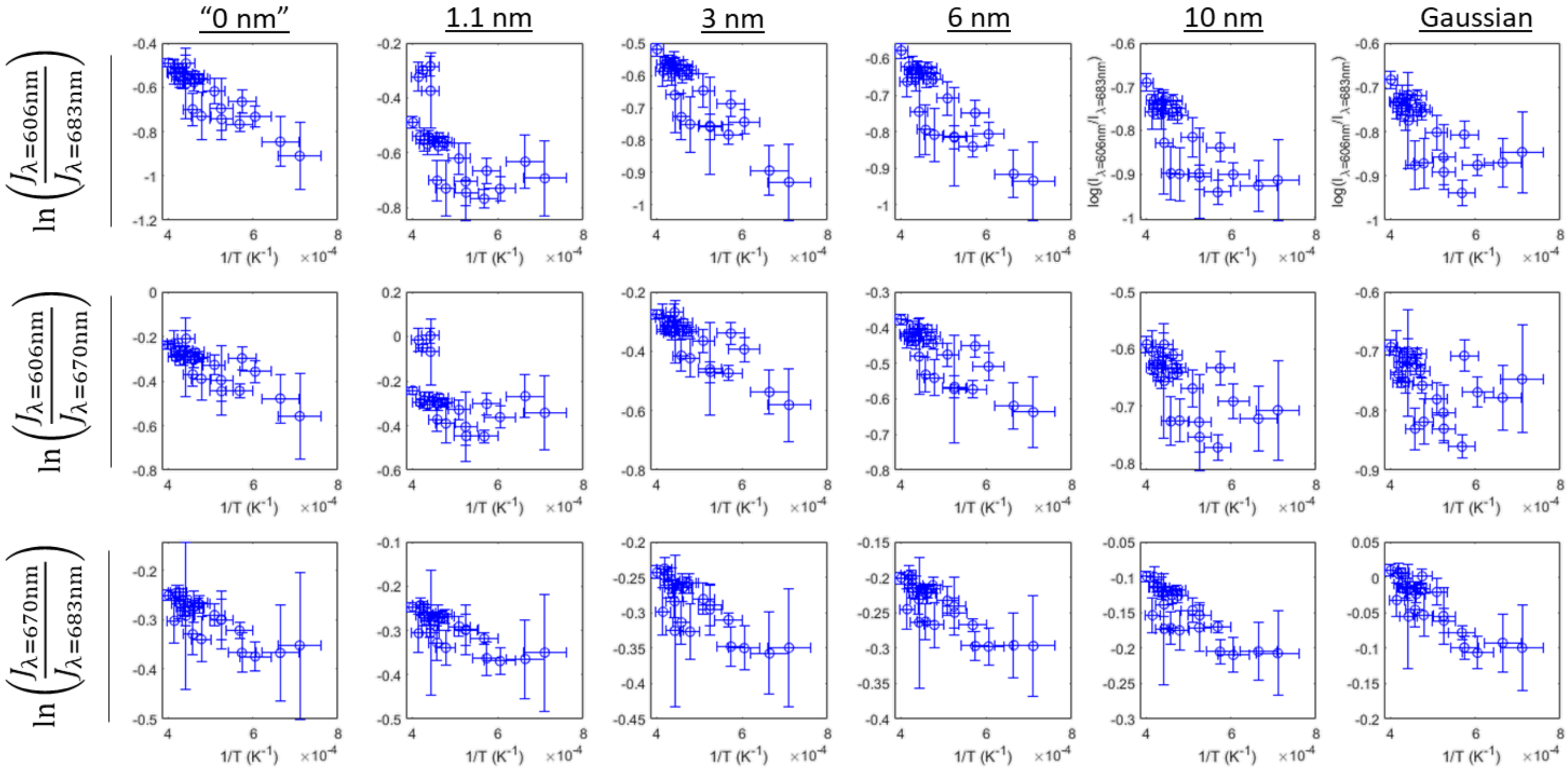

Figure 4. 14 Natural logarithm of the ratio of the measured intensity of the bands vs inverse of calculated temperature in the engine. The detection bandwidth is indicated at the top of the Figure, and it is the same for each column of plots. The y-axis label is indicated on the left side of the Figure and is equal for each row.

The first step in the approach used for line fitting while accounting for uncertainties in both variables was to iteratively simulate data with predetermined probabilistic results based on the experimental measurements and established uncertainties. This was done separately for each combination of intensity ratio and detection bandwidth considered. In each simulation one data point was selected from every test run. This data point was assigned the intensity ratio of a cycle selected at random from the ones of every cycle in the run. Each cycle in a given run had an equal probability of having its intensity ratio selected as all the others in a simulation. The temperature assignment for that point was also random, but the value was determined from a normal probability distribution centered at the temperature calculated in the engine model with a standard deviation of 100 K, since this was determined to be the error of the calculation. In this way, a point for every run was located in the $\ln\left(\frac{J_{\lambda_i,w}}{J_{\lambda_{j,w}}}\right)$ vs $1/T$ graph in each simulation.

After each simulation, a linear regression was performed. In order to account for the relative uncertainty of the different data points considered, however, a weighted linear regression was applied. Given that all uncertainties are highly correlated, as described in the previous Section, the inverse of the background index defined in Section 4.2 was used as the weighting factor, as a measure of overall uncertainty. In total, 500,000 simulations were carried out computationally for each combination of intensity ratio and detection bandwidth.

From this process, a probability distribution was obtained for the slopes and y-intercepts of Equation (2. 40). Figure 4. 15 and Figure 4. 16 are a representative example of the results. The x-axis represents the binned values of the slope and the y-axis intercept of the relationship between the $J_{\lambda=605\text{ nm}}/J_{\lambda=683\text{ nm}}$ intensity ratio and temperature with the intensity of each band having been determined by a detection bandwidth of 6 nm, as shown in Figure 4. 10. The y-axis represents the number of simulations from which a value within a given bin resulted. Given the large number of simulations performed, the shapes of the resulting curves can be assumed to be the same as those of the corresponding probability functions for each of the quantities. The distributions are close to normally distributed, and therefore the error in each of the parameters calculated was defined as the standard deviation in the resulting distribution. The results for every intensity ratio and detection bandwidth are summarized in Table 4. 1.

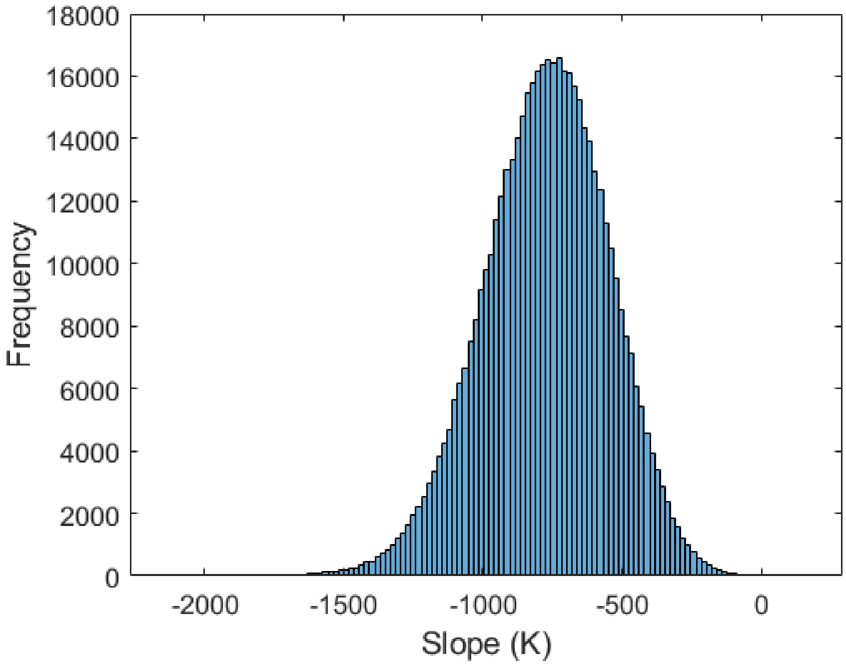

Figure 4. 15 Histogram of the results obtained for the slope of the regression line in Equation (2. 40) for the $J_{\lambda=605\ \mathrm{nm}}/J_{\lambda=683\ \mathrm{nm}}$ intensity ratio with a detection bandwidth of 6 nm.

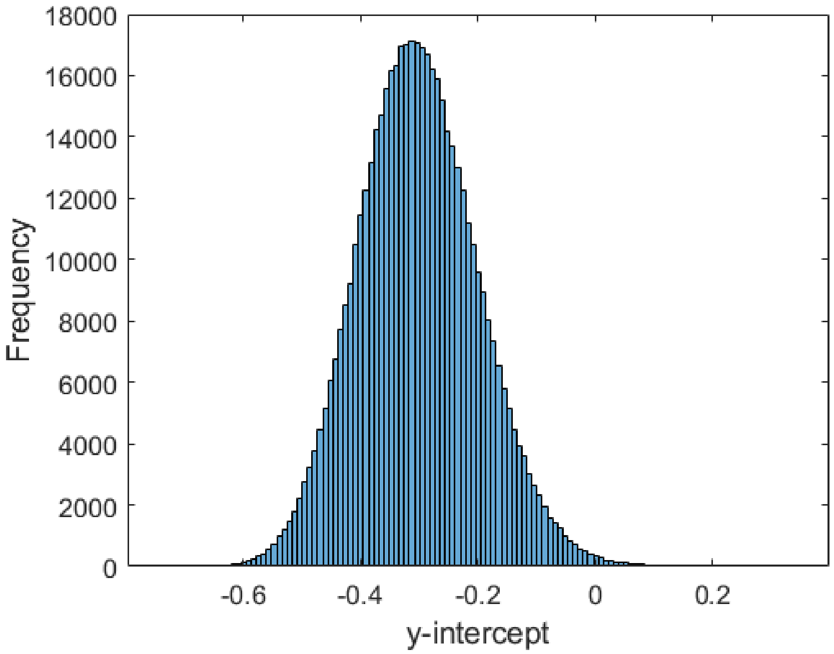

Figure 4. 16 Histogram of the results obtained for the y-intercept of the regression line in Equation (2. 40) for the $J_{\lambda=605\ \mathrm{nm}}/J_{\lambda=683\ \mathrm{nm}}$ intensity ratio with a detection bandwidth of 6 nm.

Table 4. 1 Temperature calibration constants determined from engine experiments.

λ_i/λ_j	Detection bandwidth	m_{ji} (K)	b_{ji}
606/683	'0 nm'	-780 ± 260	-0.21 ± 0.12
606/670	'0 nm'	-330 ± 190	-0.14 ± 0.09
670/683	'0 nm'	-450 ± 150	-0.06 ± 0.07
606/683	1.1 nm	-1200 ± 360	0.01 ± 0.16
606/670	1.1 nm	-750 ± 320	0.07 ± 0.15
670/683	1.1 nm	-450 ± 150	-0.06 ± 0.07
606/683	3 nm	-760 ± 230	-0.25 ± 0.11
606/670	3 nm	-360 ± 150	-0.17 ± 0.07
670/683	3 nm	-390 ± 140	-0.08 ± 0.06
606/683	6 nm	-770 ± 230	-0.30 ± 0.10
606/670	6 nm	-420 ± 140	-0.25 ± 0.07
670/683	6 nm	-340 ± 120	-0.06 ± 0.06
606/683	10 nm	-720± 210	-0.44 ± 0.10
606/670	10 nm	-320 ± 130	-0.50 ± 0.06
670/683	10 nm	-400 ± 120	0.06 ± 0.06
606/683	Gaussian	-590 ± 190	-0.49 ± 0.09
606/670	Gaussian	-280 ± 120	-0.62 ± 0.06
670/683	Gaussian	-320 ± 120	0.14 ± 0.06

4.4.2 Discussion of Results

Inspection of Table 4. 1 provides important preliminary insights. It shows that the trends of the results generally follow the one anticipated from the theory, which is expressed in Equation (2. 40). The slopes of the best-fitted lines are negative, which in accordance with Equation (2. 41) shows that the differences in excitation energy between the strontium monohydroxide bands, $(E_{\lambda=683\text{ nm}} - E_{\lambda=605\text{ nm}})$, $(E_{\lambda=670\text{ nm}} - E_{\lambda=605\text{ nm}})$, and $(E_{\lambda=683\text{ nm}} - E_{\lambda=670\text{ nm}})$ are all negative. This is the expected result since the band at 605 nm is produced by a transition to the ground state from a higher electronic state than the one produced by the bands centered at 670 nm and 683 nm, which also decay to the ground state, and the spin-orbit splitting of the first excited state results in a higher energy for the 670 nm band than for the one at 683 nm. Thus, the results show that $E_{\lambda=605\text{ nm}} > E_{\lambda=670\text{ nm}} > E_{\lambda=683\text{ nm}}$ for all detection bandwidths considered, as expected.

However, there are also some inconsistencies with some of the data. Although ideally, a best fitted line would cross every data point within uncertainty, it can be seen in most cases that at least two different lines would be needed for some of the plots in order to cross all the data points. An effort was made to empirically identify a single factor that causes this discrepancy for the intensity ratios calculated with 6 nm and 11 Å detection bandwidths, since the patterns observed in these results are representative of the ones observed in the entire set. Pressure conditions, equivalence ratio, engine metrics of performance, and image quality indexes were investigated as variables potentially correlated with vertical position on the plot. None of these were demonstrated to be an exclusive cause of the observed divergence in the 6 nm bandwidth results, but for the 1.1 nm bandwidth high spectral measurement noise was associated with the isolated group of data points in the upper left of the $\ln\left(\frac{J_{\lambda=606\text{nm}}}{J_{\lambda=683\text{nm}}}\right)$ and $\ln\left(\frac{J_{\lambda=606\text{nm}}}{J_{\lambda=670\text{nm}}}\right)$ plots. Figure 4. 17 shows a comparison of a sample of spectral measurements that resulted in the isolated group of data with one from measurements at similar temperatures in the main group lower in the plot. It is also worth mentioning that the resolution of the spectrometer used was 3 nm, and therefore any differences among the results derived from detection bands below this width are likely to be caused by noise. For all other incongruences the overall uncertainty associated with engine measurements discussed in the last section was determined to be the origin of these erratic results. All uncertainties related to these observations were ultimately accounted for with the iterative linear regression simulations.

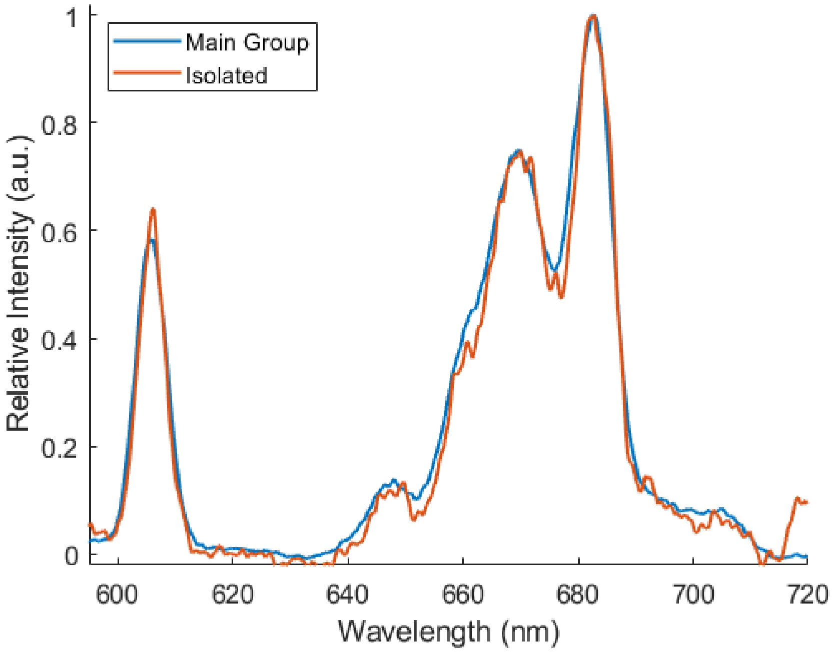

Figure 4. 17 Comparison of sample of spectral measurements that resulted in group of isolated data in the 1.1 nm results shown in Figure 4. 14 with a measurement from the main group lower in the plot. The level of noise is representative of that observed in all measurements in the run from which each was taken.

The means of the distributions of the slopes computed from these simulations, which are labeled as m_{ji} in Table 4. 1, indicate satisfactory consistency. Calculation of the differences in excitation energies from these values satisfy the constraint imposed by conservation of energy, which is that the excitation energy difference between the first and the third excited levels considered must be equal to the sum of the differences between the first and the second levels and that between the second and the third, as expressed in Equation (4. 3). This equality was satisfied with the means of the distributions of the experimentally determined energy differences to within 0.1% of relative error for all detection bandwidths examined. Although there are large errors associated with each of the energy differences, the agreement suggests congruity in the overall approach. Figure 4. 18 shows these results graphically.

$$(E_{\lambda=683\text{ nm}} - E_{\lambda=605\text{ nm}}) = (E_{\lambda=683\text{ nm}} - E_{\lambda=670\text{ nm}}) + (E_{\lambda=670\text{ nm}} - E_{\lambda=605\text{ nm}}) \qquad (4.\,3)$$

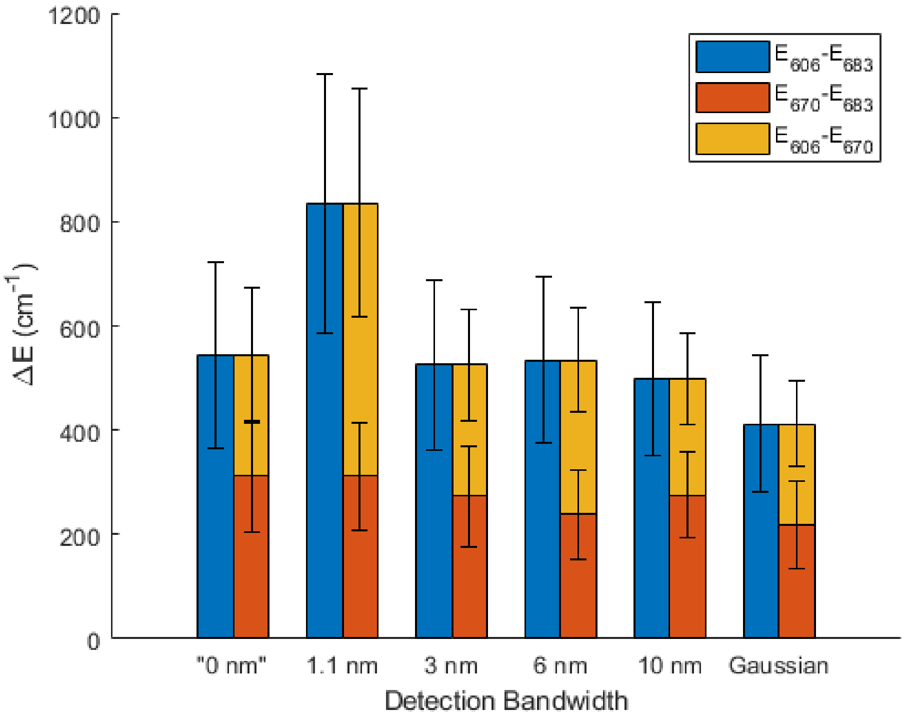

Figure 4. 18 Differences in excitation energies determined experimentally for all detection bandwidths considered. The higher difference observed for the 1.1 nm bandwidth originates from spectral measurement noise, as explained in the text. For the bars labeled “0nm” the energy differences were determined from band intensities determined by the peak intensity.

Similarly, coherence in the results was further demonstrated by the relationship among the mean of the distributions of the y-intercepts. A basis for consistency assessment using this parameter is based on the definition given in Equation (2. 42). By applying the algebraic treatment to this expression shown in Equation (4. 4), a relationship between the y-intercepts calculated for the three lines with a given detection bandwidth can be obtained.

$$e^{b_{ji,w}} = \frac{K_{\lambda_i,w}}{K_{\lambda_j,w}} = \frac{\frac{K_{\lambda_k,w}}{K_{\lambda_j,w}}}{\frac{K_{\lambda_k,w}}{K_{\lambda_i,w}}} = \frac{e^{b_{jk,w}}}{e^{b_{ik,w}}} \tag{4. 4}$$

Thus, exponentiation of e to the power of the mean of the distribution of the y-intercepts calculated from the regression routines must meet the constraint expressed above. This was, indeed, the case for all detection bandwidths within 0.02% of relative error, although once again the individual values resulted in large uncertainties. Table 4. 2 shows the results of these calculations.

Table 4. 2 Results of the consistency assessment based on the value of computed y-intercept. The values in the last two columns were expected to be the same for each row.

	$\frac{K_{\lambda=605\text{ nm}}}{K_{\lambda=683\text{ nm}}}$	$\frac{K_{\lambda=605\text{ nm}}}{K_{\lambda=670\text{ nm}}}$	$\frac{K_{\lambda=670\text{ nm}}}{K_{\lambda=683\text{ nm}}}$	$\frac{K_{\lambda=605\text{ nm}}}{K_{\lambda=683\text{ nm}}} \Big/ \frac{K_{\lambda=605\text{ nm}}}{K_{\lambda=670\text{ nm}}}$
“0 nm”	0.81 ± 0.01	0.86 ± 0.07	0.94 ± 0.07	0.94 ± 0.08
1.1 nm	1.01 ± 0.17	1.07 ± 0.16	0.94 ± 0.06	0.94 ± 0.14
3 nm	0.78 ± 0.08	0.85 ± 0.06	0.92 ± 0.06	0.92 ± 0.11
6 nm	0.74 ± 0.08	0.78 ± 0.05	0.94 ± 0.05	0.95 ± 0.12
10 nm	0.65 ± 0.06	0.61 ± 0.04	1.06 ± 0.06	1.07 ± 0.12
Gaussian	0.61 ± 0.05	0.54 ± 0.03	1.15 ± 0.06	1.13 ± 0.11

With evidence that the results satisfy essential consistency requirements, further insights were explored. Figure 4. 18 shows another important observation of relevance to the application of the diagnostic technique studied. This is that although, intuitively, the difference in excitation energy should decrease with detection bandwidth due to the bands coming nearer to each other in wavelength as the bands increase in width, the results show that for the detection band widths and profiles considered this is not the case. The effective energy difference is relatively constant for the range considered. An exception is observed with the 1.1 nm detection bandwidth, in which higher excitation energy differences $(E_{\lambda=683\text{ nm}} - E_{\lambda=605\text{ nm}})$ and $(E_{\lambda=670\text{ nm}} - E_{\lambda=605\text{ nm}})$ are observed than for the other bandwidths. This, however, is likely to be explained by the data inconsistencies observed in the 1.1 nm bandwidth plots of Figure 4. 14, which as discussed previously, are due to noise in the spectral measurements. Note that in the same Figure the $\ln\left(\frac{J_{\lambda=670\text{nm}}}{J_{\lambda=683\text{nm}}}\right)$ plot does not have an isolated group of data, and that at the same time, Figure 4. 17 shows that the $(E_{\lambda=683\text{ nm}} - E_{\lambda=670\text{ nm}})$ difference for this bandwidth is similar in magnitude to that of all other bandwidths. These results indicate that, when applying the diagnostic, there is little or no loss of sensitivity when increasing the detection bandwidth in order to increase the amount of signal detected, and that when calibrating the diagnostic, the results can be unpredictably susceptible to spectral noise.

An understanding of how this observation could be explained from theory was obtained with a coarse estimate of some of the transitions that are captured within a given band, which were computed using the spectroscopic model described in Subsection 2.2.2. Figure 4. 19, shows the distribution of excitation energies of the upper levels of the transitions captured in each band by some of the detection bandwidths used to analyze the experimental data as calculated by this spectral model. The figure shows that the distribution of calculated energies does not change significantly for any of the bands with increasing detection bandwidth, and therefore it shows that the experimental observations are indeed plausible. In addition, similar reports were previously reported, although for much smaller bandwidths and higher resolution spectral measurements [70]. Further insights from this spectroscopic model were not possible due to insufficient information available. Calculation of effective energy differences from these estimates is limited by the fact that a comprehensive report on the transition moments of the individual transitions, and therefore each of the transitions observed cannot be adequately weighted in an average.

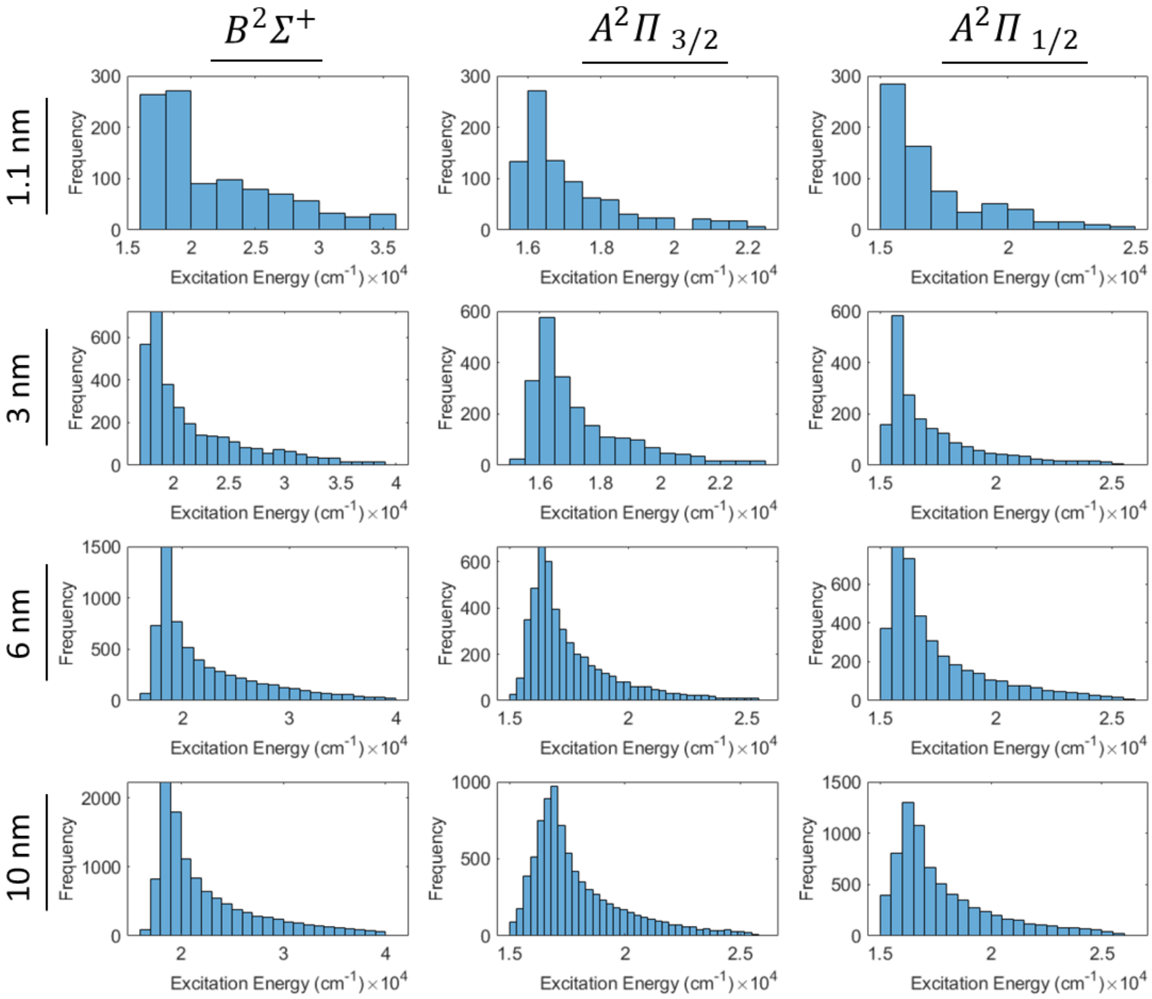

Figure 4. 19 Distributions of the computationally estimated excitation energies of the transitions detected in each band with each detection bandwidth.

Although the resulting experimental calibration coefficients show coherency with the applied theoretical treatment, the accuracy of the temperatures calculated from them and the spectral measurements is far from satisfactory. Figure 4. 20 shows how the temperature that is obtained from the computed temperature calibration constants and the spectral measurements matches the one from the GT-Power model. Only the results for the $\frac{J_{\lambda=605\text{nm}}}{J_{\lambda=683\text{nm}}}$ intensity ratio are shown since this was demonstrated to have the largest sensitivity with respect to temperature per Equation (2. 45) and given that the slope of its regression is the largest. It can be seen that the discrepancies can be as large as 1300 K, and that some of the patterns with respect to CAD computed by the spectral measurements are not as would be expected to be seen in the chamber of an engine in operation. In addition, some physically impossible results are observed (~3000 K). For these reasons, reevaluation of some of the assumptions made is required.

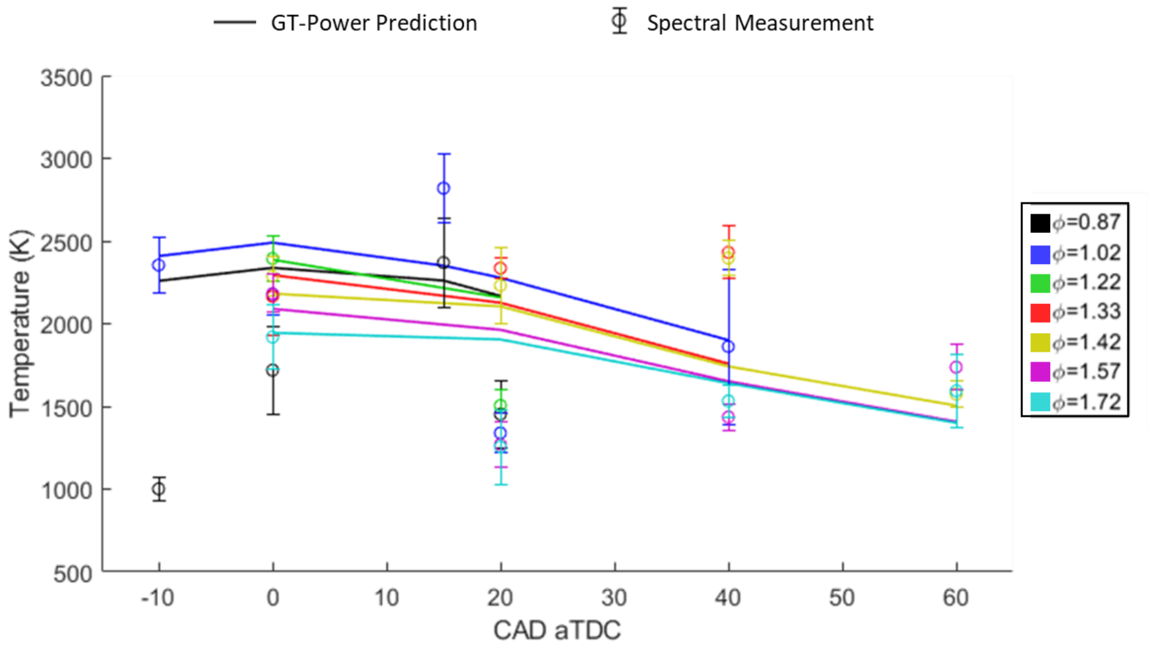

Figure 4. 20 Comparison of temperatures predicted by GT-Power and those calculated from the spectral measurements and the experimentally determined calibration coefficients for the 6 nm detection bandwidths and $\frac{J_{\lambda=605\mathrm{nm}}}{J_{\lambda=683\mathrm{nm}}}$ intensity ratio. The results from the other detection bandwidths are qualitatively similar.

One of the assumptions worth investigating in detail is that of pressure independence of the diagnostic, which was applied due to the inherent experimental limitations of the calibration method used in this work. Even though obtaining separate temperature calibrations for different pressures is not possible due to the limited range of temperatures available for a particular pressure, a useful analysis which is independent of temperature is possible. Such an assessment may be performed by equating temperature using two different intensity ratios of the same detection bandwidth with Equation (2. 43) and replacing the calculated slopes with the energy differences using Equation (2. 41), as shown below.

$$T = \frac{m_{ji,w}}{\ln\left(J_{\lambda_{i,w}} / J_{\lambda_{j,w}}\right) - b_{ji,w}} = \frac{m_{jk,w}}{\ln\left(J_{\lambda_{k,w}} / J_{\lambda_{j,w}}\right) - b_{jk,w}} \tag{4. 5}$$

$$\ln\left(\frac{J_{\lambda_k,w}}{J_{\lambda_j,w}}\right) = \frac{\Delta E_{jk,w}}{\Delta E_{ji,w}} \ln\left(\frac{J_{\lambda_i,w}}{J_{\lambda_j,w}}\right) + b_{jk,w} + \frac{\Delta E_{jk,w}}{\Delta E_{ji,w}} b_{ji,w} \tag{4. 6}$$

Thus, it is shown that by plotting experimental results of the form $\ln\left(\frac{J_{\lambda_i,w}}{J_{\lambda_j,w}}\right)$ vs. $\ln\left(\frac{J_{\lambda_k,w}}{J_{\lambda_j,w}}\right)$, a temperature-independent method for calculating energy differences relative to each other may be obtained from the slope of a line fitted through the data. This can be done for different pressure ranges to achieve a comparison.

Regressions were performed on $\ln\left(\frac{J_{\lambda_i,w}}{J_{\lambda_j,w}}\right)$ vs. $\ln\left(\frac{J_{\lambda_k,w}}{J_{\lambda_j,w}}\right)$ plots for sets of data collected at similar pressures. Figure 4. 21 shows the distribution of pressures for all spectral measurements collected in the optical engine and how their corresponding results were sectioned for this analysis. In selecting the segments, it was sought that the pressure distribution in each one of them was close to normal to avoid bias in the results towards either end of the range, and that a large number of measurements were included. Figure 4. 22 shows an example of the resulting plots and the corresponding unweighted regression lines for engine spectral measurements, and for additional comparison, burner measurements which were performed at ambient pressure. Slight discrepancies in the inclinations of the fitted lines are observed, which suggests that the relative excitation energy differences are pressure dependent.

However, an indication of the functional form of the calibration with respect to pressure was not obtained because the results were found to be significantly affected by background emission and noise in the spectral measurements.

Table 4. 3 compares the relative energy differences calculated from the slopes of lines fitted to these plots with weighted and unweighted regressions. It can be seen that only in a few cases the results agree for a given relative energy difference and pressure range within error. Since it has been shown that noise does affect the results in some cases, but it remains unclear how and when it does so, it is difficult to extract a reliable trend or to ascertain whether the observed differences are due to a systematic dependency or this noise. However, the large discrepancy between the excitation energies for ambient conditions reported previously [70], and

those shown in Figure 4. 17 provide evidence that pressure is, indeed, playing a significant role. As a side note, it is noteworthy that for a given regression method and pressure range the consistency constraint imposed by Equation (4. 3) is satisfied once again.

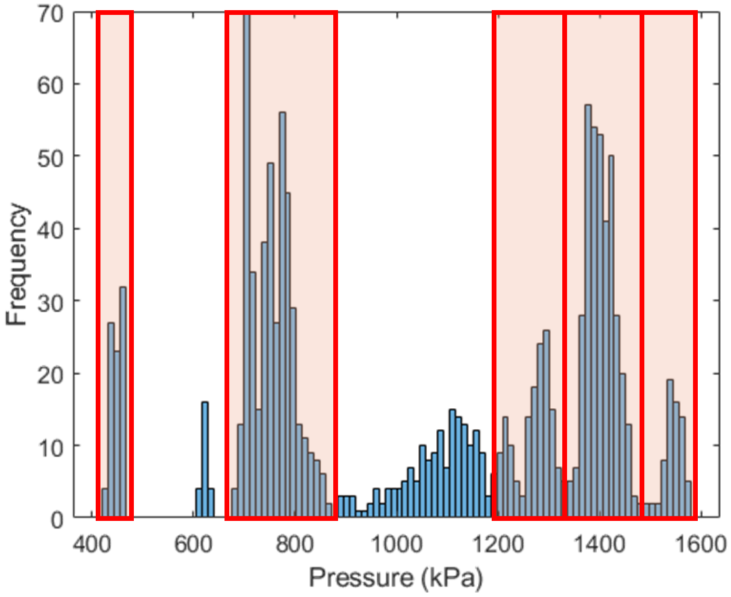

Figure 4. 21 Distribution of pressures at which spectral measurements were taken in engine experiments. The ranges used for independent analysis are indicated with the red boxes.

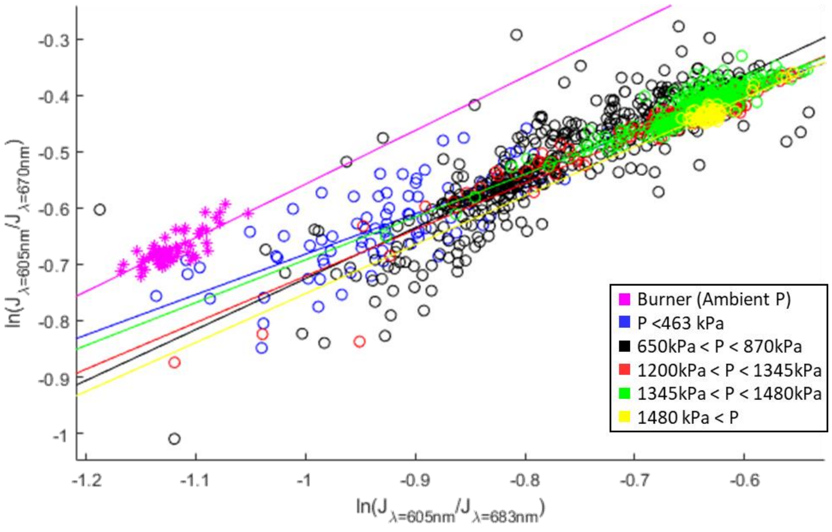

Figure 4. 22 Temperature independent analysis for engine and burner spectral measurements at different pressures. The lines were fitted through an unweighted regression. The detection bandwidth used for the intensity of each feature was 6 nm.

Table 4. 3 Relative excitation energy difference calculated from the slopes of the lines in plots such as the one exemplified in Figure 4. 22. The results correspond to the 6 nm detection bandwidth and are representative of the other detection bands used. The reported error is the one obtained from the error in the slope of the fitted line

Pressure (kPa)	$\frac{E_{\lambda=605\text{ nm}} - E_{\lambda=670\text{ nm}}}{E_{\lambda=605\text{ nm}} - E_{\lambda=683\text{ nm}}}$		$\frac{E_{\lambda=670\text{ nm}} - E_{\lambda=683\text{ nm}}}{E_{\lambda=605\text{ nm}} - E_{\lambda=683\text{ nm}}}$	
	Unweighted regression	Regression weighted by noise and background	Unweighted regression	Regression weighted by noise and background
101	0.95±0.09	0.77±0.10	0.05±0.09	0.23±0.10
425 – 463	0.72±0.07	0.79±0.07	0.28±0.07	0.21±0.07
650 - 870	0.90±0.03	0.81±0.03	0.10±0.03	0.19±0.03
1200 - 1345	0.83±0.02	0.60±0.03	0.17±0.02	0.40±0.03
1345 - 1480	0.76±0.02	0.71±0.02	0.24±0.02	0.29±0.02
1480 - 1580	0.87±0.06	0.72±0.06	0.13±0.06	0.28±0.06

Despite not being able to account for possible pressure dependencies in the calculation of calibration constants, it is possible to develop a coarse approach to account for the uncertainty introduced by neglecting a pressure dependency. This may be done by assessing the error in the temperature calculation with respect to pressure. Having found calibration constants, as described in Subsection 4.4.1, the temperatures they predict from the spectral measurements were computed and compared to the temperatures established with the engine thermodynamic model for all pressures. Then, differences between both temperature values were calculated, and the first and the third quantiles of these differences for each pressure range chosen were found. Figure 4. 23 is an example of this difference against pressure. A 50% confidence interval for temperature may be obtained by calculating the temperature calculated from spectral measurements using the calibration constants and adding to this value the quantiles mentioned of the corresponding pressure range. The width of the 50% confidence interval, is given for each pressure range in Table 4. 4. As it is shown, the intervals can be quite large, however, which shows that further improvements are necessary.

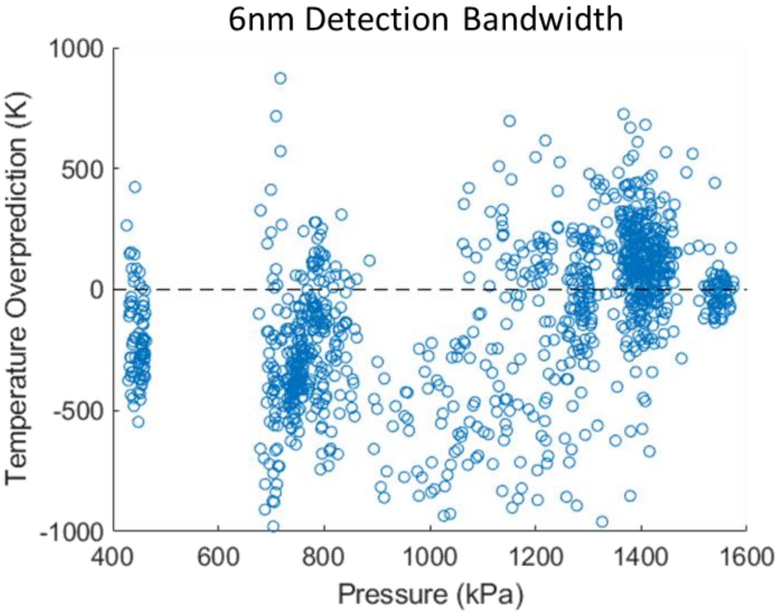

Figure 4. 23 Difference between in-cylinder temperatures calculated from 1-D thermodynamic model and computed from calibration constants and the intensity ratio $\frac{J_{\lambda=605\mathrm{nm}}}{J_{\lambda=683\mathrm{nm}}}$.

Table 4. 4 50% Confidence Interval (CI) width for each pressure range calculated for the 6 nm detection bandwidth.

Pressure Range (kPa)	50 % CI width(K)
425 – 463	224
650 - 870	306
1200 - 1345	378
1345 - 1480	223
1480 - 1580	91

4.5 Equivalence Ratio Relationship

In order to quantify the relationship between the spectral emission of strontium combustion products and equivalence ratio, a similar approach to the one used for the relationship of strontium monohydroxide emission with respect to temperature may be used. In this case, the slope and the y-intercept of the line defined by Equation (2. 47) must be found. However, a level of complexity is added to the process by the fact that two more quantities must be known besides the intensity ratio of the spectral features and the gas temperature. These additional values are the relative number density of strontium and strontium monohydroxide and the ratio of partition functions.

The first of these, the relative number density of emitting species, was found by interpolating temperature, pressure, and equivalence ratio in the results of the computational equilibrium calculations described in Section 2.1. The temperature value used here and throughout the analyses in this Section was the one predicted by the 1-D thermodynamic simulations in order to preserve consistency in error propagation with respect to the temperature calibration analyses presented in the last Section. Pressure was determined from the in-cylinder transducer measurements, and the equivalence ratio was the one for each particular engine run.

Subsequently, the ratio of partition functions was estimated by calculating the partition functions of strontium and strontium monohydroxide independently. This quantity is well characterized for atomic strontium at a wide range of temperatures, as most elements are, so a temperature dependent expression from literature [44] was used. However, an equivalent expression for strontium monohydroxide is not available, but an estimate was performed by calculating the product of the partition functions of electronic, vibrational, and rotational states, which were determined individually.

The partition function of each internal energy mode was computed from principles outlined in Chapter 2. For the electronic one, only the population of the $X^2\Sigma^+$, $A^2\Pi$, and $B^2\Sigma^+$ states were considered since any higher levels have much higher excitation energies, and their populations would be negligible at the temperatures considered. The electronic constants used were those listed in Table 2. 1. For the vibrational partition function, the populations in each mode were considered separately from their vibrational frequency, and then they were all multiplied together. Some error might have been introduced here, since this treatment does not account for the interdependence of excitation energies among the states of different modes, but in lack of a more detailed molecular spectral model at higher vibrational states, this was determined to be the best solution available. Finally, the population of the rotational states was calculated from the excitation energy using the first term of Equation (2. 3). The rotational state populations obtained in this way are very similar to those obtained with the more accurate equations that account for spin-orbit coupling (Equations (2. 5) to (2. 8)) given that the additional terms are small in magnitude. The vibrational and rotational constants used were those listed for the $X^2\Sigma^+$ state in Table 2. 1. In this way, a function of the total partition function for strontium monohydroxide with respect to temperature was found.

Since both, the relative number density of emitted species and the partition function, are dependent on temperature, it is worthwhile to assess the extent to which the large errors in the determination of in-cylinder temperature discussed in the last section propagate into the calculation of equivalence ratio. A temperature sensitivity analysis can be used to accomplish this evaluation, since for a given quantity a high temperature sensitivity results in a more significant uncertainty propagation.

As defined previously in Equation (2. 44) for intensity ratio, temperature sensitivity is the rate of change of a quantity of interest with respect to a change in temperature. The temperature sensitivity of the relative number density of strontium and strontium monohydroxide was calculated computationally for a comprehensive set of conditions representative of those obtained in the engine experiments. As shown in Figure 4. 24, pressure has a negligible effect on temperature sensitivity for this calculation at stoichiometric conditions. Similar behavior was observed at all equivalence ratios. The results as a function of temperature for different equivalence ratios are shown in Figure 4. 25. It can be readily seen that there is a rapid increase of sensitivity to temperature error with decreasing gas temperature. The effect is further exacerbated with decreasing equivalence ratios below stoichiometric conditions. This trend constitutes an added adverse effect to low temperature and low equivalence ratio to the ones discussed in Section 4.3. It exacerbates the difficulties associated with the reliability of measurements at a wide range of conditions under which a calibration process needs to be carried out. Given that the temperature uncertainty at low temperatures may be around 300 K, as shown in Table 4. 4, the number density ratio of emitting species could be inaccurate by up to 600%. This can be demonstrated by multiplying the temperature uncertainty by the sensitivity indicated in the plot.

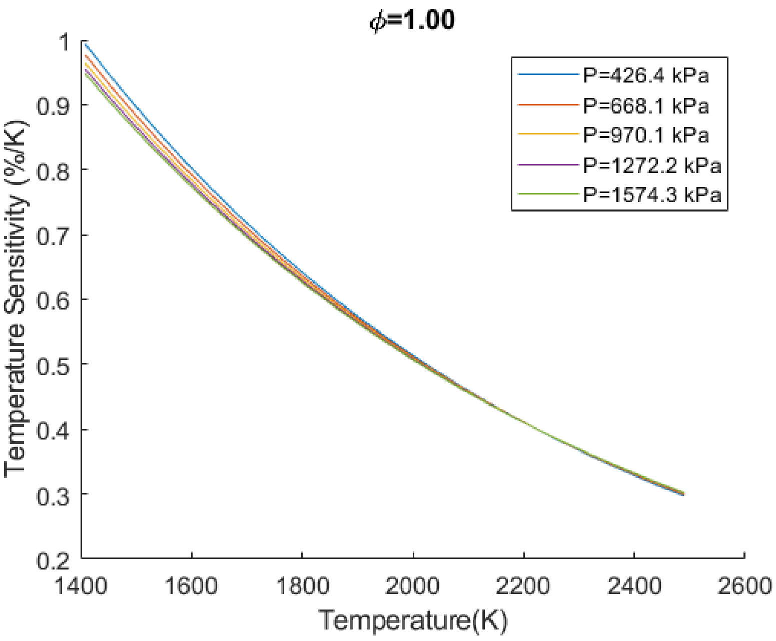

Figure 4. 24 Temperature sensitivity of the ratio of number density of strontium and strontium monohydroxide at different pressures for stoichiometric conditions.

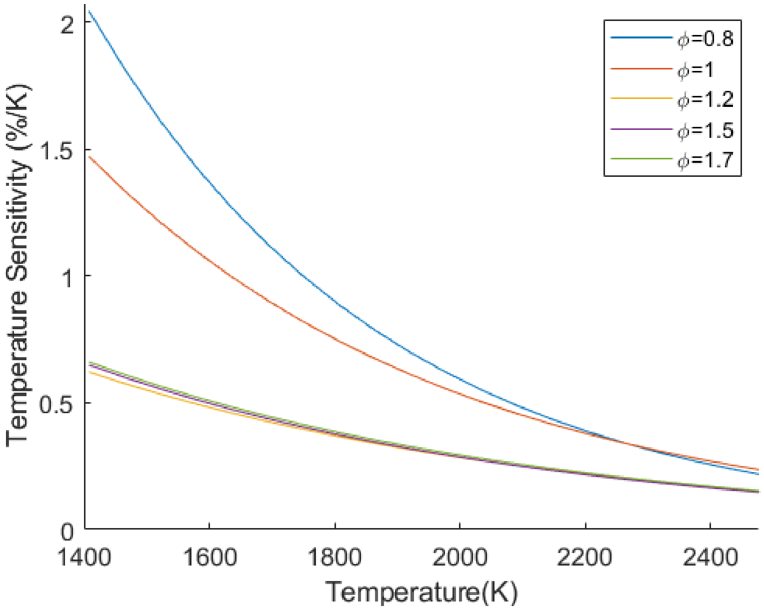

Figure 4. 25 Temperature sensitivity of the calculation of the ratio of number density of strontium and strontium monohydroxide.

By using similar computations, the temperature sensitivity of the calculation of the partition function ratio as described above was found to be comparable to that of the number density of strontium and strontium monohydroxide at stoichiometric and rich conditions. Figure 4. 26 shows the results. Similarly, the effect of temperature uncertainty is higher at low temperatures, which further compounds the issues associated with measurements at these conditions. It must be noted that this treatment, does not consider the additional error that may result from potential oversimplifications in the spectroscopic model of strontium monohydroxide, which is difficult to estimate.

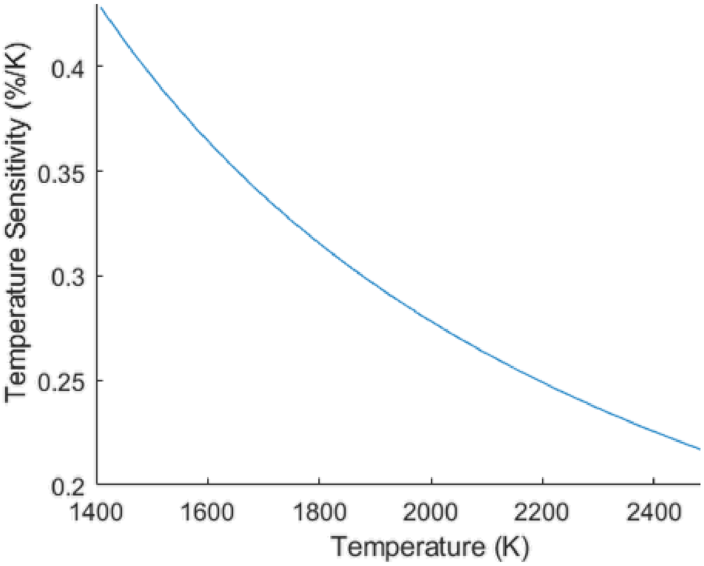

Figure 4. 26 Temperature sensitivity of the partition function ratio calculation.

Having estimated the quantities needed to obtain the calibration constants for equivalence ratio determination and assessed the impact of temperature uncertainty on them, their quantitative determination was sought with the same strategy used for temperature, which was described in detail in Subsection 4.4.1. Simulations of data with preassigned probabilistic results determined in the same way were performed, and a line was fitted to each one of them to find a probability distribution of slopes and y-intercepts. The temperatures used were once again those predicted by the GT-Power calculations. The results are shown in Table 4. 5.

Table 4. 5 Equivalence ratio calibration constants determined from engine experiments.

λ_a/λ_b	Detection Bandwidth	m_{ba} (K)	b_{ba}
461/606	'0 nm'	5900 ± 2400	-14.7 ± 1.1
461/670	'0 nm'	5600 ± 2300	-14.8 ± 1.1
461/683	'0 nm'	5400 ± 2500	-14.9 ± 1.2
461/606	1.1 nm	2900 ± 2600	-13.9 ± 1.2
461/670	1.1 nm	2700 ± 2600	-14.4 ± 1.3
461/683	1.1 nm	2300 ± 2900	-14.3 ± 1.4
461/606	3 nm	5600 ± 2300	-14.5 ± 1.4
461/670	3 nm	5200 ± 2200	-14.6 ± 1.0
461/683	3 nm	3000 ± 2700	-14.0 ± 1.2
461/606	6 nm	4300 ± 2200	-14.0 ± 1.1
461/670	6 nm	4100 ± 2300	-14.2 ± 1.1
461/683	6 nm	3700 ± 2500	-14.3 ± 1.2
461/606	10 nm	2900 ± 2500	-13.6 ± 1.2
461/670	10 nm	2500 ± 2700	-13.9 ± 1.3
461/683	10 nm	2300 ± 2800	-14.0 ± 1.3
461/606	Gaussian	2800 ± 2600	-13.9 ± 1.2
461/670	Gaussian	2500 ± 2700	-14.6 ± 1.3

Consistency inspections were performed on the results. The validity of the predicted excitation energy differences can be assessed with expressions equivalent to Equation (4. 3) that include the excitation energy of atomic strontium, which are given below.

$$(E_{\mathrm{Sr}} - E_{\mathrm{SrOH},\lambda=683\ \mathrm{nm}}) = (E_{\mathrm{Sr}} - E_{\lambda=605\ \mathrm{nm}}) + \left(E_{\mathrm{SrOH},\lambda=605\ \mathrm{nm}} - E_{\mathrm{SrOH},\lambda=683\ \mathrm{nm}}\right) \quad (4.\ 7)$$

$$(E_{\mathrm{Sr}} - E_{\mathrm{SrOH},\lambda=670\ \mathrm{nm}}) = (E_{\mathrm{Sr}} - E_{\lambda=605\ \mathrm{nm}}) + \left(E_{\mathrm{SrOH},\lambda=605\ \mathrm{nm}} - E_{\mathrm{SrOH},\lambda=670\ \mathrm{nm}}\right) \quad (4.\ 8)$$

The differences between each side of both of these equations were found to be considerable. They ranged from 5% to 120% for the different detection bandwidths considered, which makes the validity of the calculated calibration constants dubious. In all likelihood these discrepancies are due to the errors in temperature and their propagation into the calculation of quantities needed for the calibration.

Chapter 5

Conclusions and Recommended Future Work

5.1 Conclusions

The potential of an optical diagnostics technique that uses the thermal radiative emission of atomic strontium and strontium monohydroxide to calculate in-cylinder temperature and equivalence ratio in IC engines was investigated. The study was motivated by the fact that the method could potentially provide volumetric measurements of these quantities in the combustion chamber, which are generally not available with state-state-of-the-art techniques. In addition, the technique would provide these measurements in a simplified and more robust way than is currently available, and thus it would make optical diagnostics more widely available and accelerate the development of IC engines.

The technique is based on the spectroscopy of atomic strontium and strontium monohydroxide in the visible range. The latter species is a largely uncharacterized molecular radical, which introduces several difficulties in the development of a diagnostics method that stem from the fact that the relative importance of the chemical and physical processes that take place during spectral measurements are unknown. In addition, a calibration process is necessary in order to quantify the relationship between spectral emission and the gas quantities to be determined from the diagnostics method. In the study presented both of these needs were addressed experimentally.

A fuel mixture that provides a sufficient but not excessive amount of strontium into an engine cylinder was identified and characterized. In this way the need for supplementary systems and hardware was eliminated, which is in conformity with the stated goal of developing an easily implementable technique. Besides providing a recommendation for a strontium substance to use, advice based on the consideration of potentially interfering signals was given on others to avoid in the further development of fuel mixtures.

In addition, experimental calibration of the spectral emission of strontium monohydroxide with respect to temperature was pursued and key validating observations were made. An optical engine was operated under different conditions with the developed strontium-containing fuel and spectral measurements of the radiation emitted from the chamber were performed. The temperature in the cylinder was predicted by a one-dimensional thermodynamic model that used a two-zone model for flame propagation. Despite significant experimental noise and uncertainty, consistency between the spectral measurements and the mathematical formulation of their relationship with temperature was repeatedly demonstrated in several independent analyses. These showed that the theoretical approach used is adequate and that the relevant physical processes are properly accounted for.

Furthermore, key insights were obtained for the application of the diagnostic to imaging experiments. The results showed that there is little to no loss of temperature sensitivity with increasing width of detection band used to determine the intensity of a strontium monohydroxide band, which implies that there is no tradeoff in using filters of larger bandwidths in imaging studies to obtain higher intensity images.

Despite these accomplishments, a universally applicable calibration was not obtained due to experimental limitations, but essential barriers to overcome were identified. It was demonstrated that noise in the spectral measurements affects the calibration in ways that are difficult to identify in detail and correct during post-processing.

In addition, it was determined that a complete characterization of the relationship between temperature and spectral emission of strontium monohydroxide likely necessitates calibrations to be carried out as a function of pressure, which was not possible in this work due to the fact that pressure and temperature in an engine are inherently related and a large enough temperature range for spectral measurements at a given pressure cannot be achieved. Although a method to coarsely account for pressure with the methodology used was recommended, large uncertainties remained.

Finally, it was determined that a more accurate way to determine the temperature at which the spectral measurements are performed is needed. This is because the results of the measurements in a given engine run fluctuate from cycle to cycle in much greater magnitude than can be explained by standard engine variability metrics, and therefore common engine analysis tools are insufficient as a calibration standard.

Addressing these issues would permit the calculation of temperature from strontium monohydroxide spectral emission, which at the same time would enable determination of equivalence ratio from the spectral emission of atomic strontium and strontium monohydroxide.

5.2 Recommendations for Future Work

Although this work has demonstrated great potential for the presented temperature and equivalence ratio diagnostics method in IC engines, further research is necessary in order to generalize the relationship between spectral signals and the combustion parameters of interest beyond the limited range of conditions considered experimentally in this work and permit the eventual attainment of high quality images of these quantities with high temporal and spatial resolution. With these aims, future studies for the development of this technique must focus on performing spectral measurements with higher spectral intensities and dynamic range at more granular and certain sets of conditions. In addition, characterizing the strontium monohydroxide molecule in more detail would be beneficial as well.

This study demonstrated that in order to advance this method further, higher signal-to-noise ratio spectral measurements under a broader set of conditions would be needed. The higher signal would reduce noise and relative background intensity, which was determined to be detrimental in calibration measurements. These higher intensity measurements may be achieved through a more optically efficient setup. For instance, as opposed to coupling the entrance of the spectrometer and the combustion chamber with a collector and a fiber, as done in this work, these elements may be coupled directly through a large lens. In addition, improvements in the hardware used to record the measurements are needed as well. Due to the large differences in emission intensity between the strontium and the strontium monohydroxide features, a higher dynamic range detector is needed. Alternatively, independent detectors could be used to detect emission from either species.

In addition to higher intensity emission from the probed gas and adequate detection, spectral measurements over a more comprehensive set of homogeneous and well-known conditions would also enhance the capabilities of the diagnostic. Emission of atomic strontium and strontium monohydroxide could be produced in a pressurized combustion vessel or burner with a more extensive combination of temperatures and pressures. In this way, uncertainties in the measurements could be further reduced significantly by accounting for pressure dependencies in the relationships between the scalar quantities and spectral emission.

Further characterization of the strontium monohydroxide molecule is necessary as well. Although the need of an exhaustive spectroscopic model of this molecule may be avoided with more comprehensive experimental measurements, an accurate expression for its partition function with respect to temperature is still required in order to obtain low error equivalence ratio measurements. Such a relationship may be found with benchtop experiments designed for this purpose. In addition, detailed information of the Einstein emission coefficients of the individual transitions in each molecular band, would be helpful in determining an excitation energy difference theoretically.

REFERENCES

1. Agency, E.P. *Fast Facts on Transportation Greenhouse Gas Emissions*.
2. Britannica, E. *Fuel Injection | Engineering Technology | Britannica.com*. 2011 [cited 2017 2/17/2017]; Available from: https://www.britannica.com/technology/fuel-injection.
3. Heywood, J.B., *Internal combustion engine fundamentals.* 1988.
4. Woschni, G., *A universally applicable equation for the instantaneous heat transfer coefficient in the internal combustion engine*. 1967, SAE Technical paper.
5. Alkidas, A.C., *Combustion advancements in gasoline engines.* Energy Conversion and Management, 2007. **48**(11): p. 2751-2761.
6. Ceviz, M. and I. Kaymaz, *Temperature and air–fuel ratio dependent specific heat ratio functions for lean burned and unburned mixture.* Energy Conversion and Management, 2005. **46**(15-16): p. 2387-2404.
7. Akihama, K., et al., *Mechanism of the smokeless rich diesel combustion by reducing temperature*. 2001, SAE technical paper.
8. McIlroy, A., et al., *Basic research needs for clean and efficient combustion of 21st century transportation fuels*. 2006, DOESC (USDOE Office of Science (SC)).
9. Schuette, M., et al., *Spatially Resolved Air–Fuel Ratio and Residual Gas Measurements by Spontaneous Raman Scattering in a Firing Direct Injection Gasoline Engine*. 2000, SAE Technical Paper.
10. Ipp, W., et al., *2D mapping and quantification of the in-cylinder air/fuel-ratio in a GDI engine by means of LIF and comparison to simultaneous results from 1D Raman measurements*. 2001, SAE Technical Paper.
11. Fischer, J., et al., *Measurement of the equivalence ratio in the spark gap region of a gasoline direct injection engine with spark emission spectroscopy and tracer-LIF*. 2004, SAE Technical Paper.

12. Sacadura, J.C., et al., *Experimental investigation of an optical direct injection SI engine using fuel-air ratio laser induced fluorescence*. 2000, SAE Technical Paper.

13. Depussay, E., et al., *Comparative Measurements of Local Iso-Octane Concentrations by Planar Laser Induced Fluorescence and Catalytic Hot Wires Probe in SI Engines*. 1998, SAE Technical Paper.

14. Peterson, B., D.L. Reuss, and V. Sick, *On the ignition and flame development in a spray-guided direct-injection spark-ignition engine.* Combustion and Flame, 2014. **161**(1): p. 240-255.

15. Lillo, P.M., H. Zhuang, and V. Sick, *Topological development of homogeneous-charge and spray-guided stratified-charge flames in an internal combustion engine.* International Journal of Engine Research, 2017. **19**(1): p. 96-108.

16. Fansler, T., et al., *Local fuel concentration measurements in internal combustion engines using spark-emission spectroscopy.* Applied Physics B, 2002. **75**(4-5): p. 577-590.

17. Hershey, A.E. and R.F. Paton, *Flame temperatures in an internal combustion engine measured by spectral line reversal*. 1933, University of Illinois at Urbana Champaign, College of Engineering. Engineering Experiment Station.

18. Watts, S. and B. Lloyd-Evans, *The measurement of flame temperatures in a petrol engine by the spectral line-reversal method.* Proceedings of the Physical Society, 1934. **46**(3): p. 444.

19. Rassweiler, G.M. and L. Withrow, *Flame Temperatures Vary with Knock and Combustion-Chamber Position*. 1935, SAE Technical Paper.

20. Brevoort, M.J., *Combustion Engine Temperatures by the Sodium Line-Reversal Method.* Review of Scientific Instruments, 1936. **7**(9): p. 342-346.

21. Withrow, L. and G.M. Rassweiler, *Studying engine combustion by physical methods a review.* Journal of Applied Physics, 1938. **9**(6): p. 362-372.

22. Reissing, J., et al., *Optical investigations of a gasoline direct injection engine*. 1999, SAE Technical Paper.

23. Beck, K.W., et al., *Spectroscopic measurements in small two-stroke SI engines*. 2009, SAE Technical Paper.

24. Zeng, W., et al., *Conditional analysis of enhanced combustion luminosity imaging in a spray-guided gasoline engine with high residual fraction*. 2011, SAE Technical Paper.

25. Mosburger, M., V. Sick, and M. Drake, *Quantitative high-speed burned gas temperature measurements in internal combustion engines using sodium and potassium fluorescence.* Applied Physics B, 2013. **110**(3): p. 381-396.
26. Mosburger, M., V. Sick, and M.C. Drake, *Quantitative high-speed imaging of burned gas temperature and equivalence ratio in internal combustion engines using alkali metal fluorescence.* International Journal of Engine Research, 2013: p. 1468087413476291.
27. Mosburger, M.J., *Alkali metal spectroscopy for high-speed imaging of burned gas temperature, equivalence ratio and mass fraction burned in internal combustion engines*, in *Mechanical Engineering*. 2013, University of Michigan.
28. Van der Hurk, J., T. Hollander, and C.T.J. Alkemade, *Identification of the emitters of some visible alkaline-earth bands in flames.* Journal of Quantitative Spectroscopy and Radiative Transfer, 1973. **13**(3): p. 273-288.
29. Alkemade, C.T.J., et al., *Metal Vapours in Flames*. International Series in Natural Philosophy. 1982: Pergamon. 1054.
30. Nakagawa, J., R.F. Wormsbecher, and D.O. Harris, *High-resolution laser excitation spectra of linear triatomic molecules: Analysis of the B 2 Σ+-X 2 Σ+ system of SrOH and SrOD.* Journal of Molecular Spectroscopy, 1983. **97**(1): p. 37-64.
31. Brazier, C. and P. Bernath, *Laser and fourier transform spectroscopy of the Ã2II-X̃2Σ+ transition of SrOH.* Journal of Molecular Spectroscopy, 1985. **114**(1): p. 163-173.
32. Gordon, S. and B.J. McBride. *NASA Chemical Equilibrium with Applications (CEA).* 02/04/16 [cited 2016 10/11/16]; Available from: https://cearun.grc.nasa.gov/.
33. Gordon, S. and B.J. McBride, *Computer Program for Calculation of Complex Chemical Equilibrium Compositions and Applications I. Analysis*, O.o.M. National Aeronautics and Space Administration, Scientific and Technical Information Program, Editor. 1994, Citeseer.
34. McBride, B.J. and S. Gordon, *Computer Program for Calculation of Complex Chemical Equilibrium Compositions and Applications II. Users Manual and Program Description*, O.o.M. National Aeronautics and Space Administration, Scientific and Technical Information Program, Editor. 1996.
35. Meyerriecks, W. and K. Kosanke, *Color values and spectra of the principal emitters in colored flames.* J. Pyrotechnics, 2003. **18**: p. 1-22.

36. *NIST: Atomic Spectra Database*. [cited 2015 3/4/2015]; Available from: https://physics.nist.gov/PhysRefData/ASD/lines_form.html.

37. Banwell, C.N., *Fundamentals of Molecular Spectroscopy*. 1966: McGraw-Hill. 291.

38. Beardah, M.S., *Laser spectroscopy of small metal-containing free radicals*. 1999, Chemistry.

39. Pittner, S., et al., *Charge transport analysis of poly (3-hexylthiophene) by electroreflectance spectroscopy.* Physical Review B, 2013. **87**(11): p. 115211.

40. Anderson, M., W. Barclay, and L. Ziurys, *The millimeter-wave spectrum of the SrOH and SrOD radicals.* Chemical physics letters, 1992. **196**(1): p. 166-172.

41. Herzberg, G., *Molecular spectra and molecular structure. Vol. 1: Spectra of diatomic molecules.* New York: Van Nostrand Reinhold, 1950, 2nd ed., 1950. **1**.

42. Wang, J.-G., et al., *Further spectroscopic investigations of the high energy electronic states of SrOH: The B∼′ 2Σ+(000)–A∼ 2Π (000) and the D∼ 2Σ+(000)–A∼ 2Π (000) transitions.* Journal of Molecular Spectroscopy, 2007. **245**(1): p. 26-33.

43. Rozema, L.A., et al., *Violation of Heisenberg's measurement-disturbance relationship by weak measurements.* Physical review letters, 2012. **109**(10): p. 100404.

44. De Galan, L., R. Smith, and J. Winefordner, *The electronic partition functions of atoms and ions between 1500 K and 7000 K.* Spectrochimica Acta Part B: Atomic Spectroscopy, 1968. **23**(8): p. 521-525.

45. Sullivan, F., *Strontium Lines in Arc and Solar Spectra.* 1938.

46. Lebedeva, N. and V. Belyaev, *Determination of probability of A 2 Π-X 2 Σ optical transition of SrOH molecule.* 1993.

47. Belyaev, V., et al., *Determination of probability of optical transition B 2 Σ→ X 2 Σ and dissociation energy of SrOH using a method of flame spectrophotometry.* 1982.

48. Juncar, P., et al., *Absolute determination of the wavelengths of the sodium D1 and D2 lines by using a cw tunable dye laser stabilized on iodine.* Metrologia, 1981. **17**(3): p. 77.

49. Hollander, T., et al., *Quenching of excited strontium atoms measured in flames.* Journal of Quantitative Spectroscopy and Radiative Transfer, 1972. **12**(6): p. 1067-1071.

50. Jansen, B., T. Hollander, and H. Van Helvoort, *Cross sections for the quenching of the excited strontium state (51P1) measured in CO/N2O flames.* Journal of Quantitative Spectroscopy and Radiative Transfer, 1977. **17**(2): p. 193-196.

51. Human, H. and P.T. Zeegers, *Molecular fluorescence of CaOH, SrOH and BaCl in flames.* Spectrochimica Acta Part B: Atomic Spectroscopy, 1975. **30**(6): p. 203-209.

52. Bonczyk, P.A., *Laser-induced saturated fluorescence of SrOH in flames.* Applied optics, 1989. **28**(8): p. 1529-1532.

53. Linne, M.A., *Spectroscopic measurement: an introduction to the fundamentals*. 2002: Academic Press.

54. Rybicki, G.B. and A.P. Lightman, *Radiative processes in astrophysics*. 2008: John Wiley & Sons.

55. Reuss, D.L., *Cyclic variability of large-scale turbulent structures in directed and undirected IC engine flows.* SAE transactions, 2000: p. 128-145.

56. Pedersen, C.J., *Cyclic polyethers and their complexes with metal salts.* Journal of the American Chemical Society, 1967. **89**(26): p. 7017-7036.

57. Bajaj, A.V. and N.S. Poonia, *Comprehensive coordination chemistry of alkali and alkaline earth cations with macrocyclic multidentates: latest position.* Coordination chemistry reviews, 1988. **87**: p. 55-213.

58. Høiland, H., J.A. Ringseth, and T.S. Brun, *Cation-crown ether complex formation in water. II. Alkali and alkaline earth cations and 12-crown-4, 15-crown-5, and 18-crown-6.* Journal of Solution Chemistry, 1979. **8**(11): p. 779-792.

59. Pedersen, C.J. and H. Frensdorff, *Macrocyclic polyethers and their complexes.* Angewandte Chemie International Edition in English, 1972. **11**(1): p. 16-25.

60. Frensdorff, H.K., *Stability constants of cyclic polyether complexes with univalent cations.* Journal of the American Chemical Society, 1971. **93**(3): p. 600-606.

61. Thorlabs, I. *Air-Spaced Doublet Collimators*. 2019 07/26/2019]; Available from: https://www.thorlabs.com/newgrouppage9.cfm?objectgroup_id=1337&pn=F810SMA-635.

62. Greene, M., *Momentum Near-wall Region Characterization in a Reciprocating Internal-combustion Engine*, in *Mechanical Engineering*. 2017, University of Michigan: Ann Arbor, MI.

63. Ombrello, T., C. Carter, and V. Katta, *Burner platform for sub-atmospheric pressure flame studies.* Combustion and Flame, 2012. **159**(7): p. 2363-2373.

64. Hancock, R.D., K.E. Bertagnolli, and R.P. Lucht, *Nitrogen and hydrogen CARS temperature measurements in a hydrogen/air flame using a near-adiabatic flat-flame burner.* Combustion and Flame, 1997. **109**(3): p. 323-331.

65. Furlong, E., D. Baer, and R. Hanson. *Combustion control using a multiplexed diode-laser sensor system*. in *Symposium (International) on Combustion*. 1996. Elsevier.

66. Belmont, E., et al., *Experimental and numerical investigation of freely propagating flames stabilized on a Hencken Burner.* Combustion and Flame, 2015.

67. Cotton, D. and D. Jenkins, *Catalysis of radical-recombination reactions in flames by alkaline earth metals.* Transactions of the Faraday Society, 1971. **67**: p. 730-739.

68. Blackburn, M., J. Mermet, and J. Winefordner, *CW-laser excited molecular fluorescence of species in flames.* Spectrochimica Acta Part A: Molecular Spectroscopy, 1978. **34**(9): p. 847-852.

69. Krystek, M. and M. Anton, *A weighted total least-squares algorithm for fitting a straight line.* Measurement Science and Technology, 2007. **18**(11): p. 3438.

70. Van der Hurk, J., T. Hollander, and C.T.J. Alkemade, *Excitation energies of strontium mono-hydroxide bands measured in flames.* Journal of Quantitative Spectroscopy and Radiative Transfer, 1974. **14**(11): p. 1167-1178.